

**RARE EARTH ( $\Pi = \text{Ce, Er, Pr}$ ) SUBSTITUTED  $\text{Bi}_{(4-x)} \Pi_x \text{Ti}_3\text{O}_{12}$  THIN FILMS:  
SYNTHESIS, STRUCTURAL AND FERROELECTRIC PROPERTIES**

by

**SANDRA LILIANA DUSSAN DEVIA**

Thesis submitted in partial fulfillment of the requirements for the degree of

MASTER OF SCIENCE

In

Physics

UNIVERSITY OF PUERTO RICO

MAYAGÜEZ CAMPUS

2005

Approved by:

\_\_\_\_\_  
Dorial Castellanos, Ph.D  
President, Graduate Committee

\_\_\_\_\_  
Date

\_\_\_\_\_  
Oscar Perales Perez, Ph.D.  
Member, Graduate Committee

\_\_\_\_\_  
Date

\_\_\_\_\_  
Hector Jiménez. Ph.D  
Member, Graduate Committee

\_\_\_\_\_  
Date

\_\_\_\_\_  
Marcelo Suarez, Ph.D.  
Representative of Graduate Studies

\_\_\_\_\_  
Date

\_\_\_\_\_  
Félix Fernández, Ph.D.  
Chairperson of the Department

\_\_\_\_\_  
Date

## ABSTRACT

In the present research, rare earths ( $\Pi = \text{Ce, Er, Pr}$ )-substituted bismuth titanate  $\text{Bi}_{(4-x)}\Pi_x\text{Ti}_3\text{O}_{12}$  thin films were synthesized by a chemical solution deposition (Sol-Gel) technique. Films were deposited by spin coating on Pt ( $\text{Pt/TiO}_2/\text{SiO}_2/\text{Si}$ ) substrates followed by their annealing at  $750^\circ\text{C}$  in air. The XRD patterns showed polycrystalline materials with preferential (117) orientation and a grain size between 20-40 nm estimated by the Debye-Scherrer equation. The AFM images of  $1\ \mu\text{m}^2$  areas showed fairly uniform grains with smooth surface (root-mean-square roughness  $R_{\text{ms}} < 13\ \text{nm}$ ) morphology. For  $x < 0.75$ , the  $\text{Bi}_{(4-x)}\Pi_x\text{Ti}_3\text{O}_{12}$  films capacitors with a Pt top electrode exhibited good ferroelectric properties with the highest remnant polarization ( $P_{\text{R}} = P_{\text{S}}/2$ ) values of  $27.1\ \mu\text{C}/\text{cm}^2$ ,  $22.2\ \mu\text{C}/\text{cm}^2$  and  $50.3\ \mu\text{C}/\text{cm}^2$  for  $\Pi = \text{Ce, Er, Pr}$ , respectively and  $x = 0.55$ . The leakage current of  $10^{-7}\ \text{A}/\text{cm}^2$  was found to be lower than in the pure bismuth titanate ( $\text{Bi}_4\text{Ti}_3\text{O}_{12}$ ) films.

## RESUMEN

Este trabajo presenta la síntesis de películas delgadas de titanato de bismuto " $\text{Bi}_{(4-x)}\Pi_x\text{Ti}_3\text{O}_{12}$ " dopado con tierras raras " $\Pi = \text{Ce, Er, Pr}$ " usando el método de Sol-Gel, las películas fueron depositadas sobre sustratos de Pt ( $\text{Pt}/\text{TiO}_2/\text{SiO}_2/\text{Si}$ ) por "spin coating" seguido de un tratamiento térmico a una temperatura de  $750^\circ\text{C}$  durante 1 hora. Los análisis de los patrones de rayos-x mostraron películas policristalinas con una preferencial orientación por el plano (117), el tamaño del grano fue entre 20-40 nm, calculado a partir de la ecuación de Debye-Scherrer. Las imágenes obtenidas por el microscopio de fuerza atómica indicaron películas homogéneas con una rugosidad promedio menor de 13 nm. Los capacitores formados con las películas exhibieron un alto valor de polarización remanente para  $x=0.55$  con valores de  $27.1 \mu\text{C}/\text{cm}^2$ ,  $22.2 \mu\text{C}/\text{cm}^2$  y  $50.3 \mu\text{C}/\text{cm}^2$  para Ce, Er, y Pr respectivamente, la medida de pérdida de corriente fue menor que el valor obtenido del material sin dopar.

## DEDICATION

*This work is dedicated to God has given me the strength to overcome many difficult situations and obstacles and especially to my dear and beautiful mother HERLINDA DEVIA that always has been at my side, supporting and giving me all of her love.*

## **ACKNOWLEDGMENTS**

During the process of my master's degree in the University of Puerto Rico "Mayagüez Campus" there is lots of people who I have to thank for giving me their help. First of all I would like to thank my advisor, Dr. M. Tomar for giving me the opportunity of becoming part of his work group and for the support he made with his knowledge to this investigation. I would also like to thank my graduate committee: Dr. Oscar Perales for his valuable orientation and collaboration, which has been the key for the culmination of this work. He is not only professor but a model to follow because of his dedication, patience and love for work. I thank Dr. Dorial Castellanos and Dr. Hector Jiménez for his time and insightful comments on this work.

Thanks to Dr. Katiyar and his students in the University of Puerto Rico "Rio Piedras Campus" for facilitating their equipment to make the measurements for characterizations of my samples.

Finally but not less important thanks to my family in Colombia for all their support and especially to my boy friend Adrian Parra who with his continuous words of encouragement has always given me strength for not giving up when confronting difficulties.

## TABLE OF CONTENTS

LIST OF TABLES.....	viii
LIST OF FIGURES.....	ix
CHAPTER 1. INTRODUCTION.....	1
1.1. Definition and Properties of Ferroelectric Materials.....	4
1.1.1. Ferroelectric Domains .....	5
1.2. Ferroelectricity in Perovskite and Perovskite-like layered-structures.....	10
1.3. Objectives in this Research.....	12
CHAPTER 2. BACKGROUND INFORMATION.....	13
2.1. Physical Vapor Deposition (PVD).....	13
2.1.1. Pulsed Laser Deposition (PLD).....	13
2.1.2. Sputtering.....	15
2.2. Chemical Vapor Deposition (CVD).....	17
2.3. Chemical Solution Deposition (CSD).....	19
CHAPTER 3. PROCEDURE EXPERIMENTAL.....	24
3.1. Solution Preparation.....	24
3.2. Thin Film Preparation.....	25
3.3. Powder Synthesis .....	27

3.4. Safety Precautions.....	27
3.5. Characterization of the Samples.....	28
CHAPTER 4. RESULTS AND DISCUSSION.....	29
4.1. X-ray Diffraction Study.....	29
4.2. Atomic Force Microscopy (AFM) Analyses.....	35
4.3. Ferroelectric properties.....	43
4.4. Dielectric Properties.....	50
4.5. Leakage Current Analyses .....	57
CHAPTER 5. RESULTS ANALYSIS.....	61
5.1 Change in lattice parameters.....	74
5.2 Ferroelectric properties.....	76
5.3 Spontaneous polarization.....	78
5.3 Lakeage Current .....	78
CHAPTER 6. CONCLUSIONS AND FUTURE WORKS.....	80
APENDIX .....	83
REFERENCES.....	87

## LIST OF TABLES

Table 1. Curie temperature for ferroelectric material.....	5
Table 2. maximum polarization remnant “ $(P_R)_{max}$ ”, for some ferroelectric crystalline Structures.....	8
Table 3. Mean size grain of the thin films annealed at 750°C/ 1h as function of amount of composition of Ce in $Bi_{(4-x)}Ce_xTi_3O_{12}$ .....	31
Table 4. Mean size grain of the thin films annealed at 750°C/ 1h as function of amount of composition of Er in $Bi_{(4-x)}Er_xTi_3O_{12}$ .....	32
Table 5. Mean size grain of the thin films annealed at 750°C/ 1h as function of amount of composition of Pr in $Bi_{(4-x)}Pr_xTi_3O_{12}$ .....	33
Table 6. Root mean square roughness of the thin films annealed at 750°C for 1hour as function of amount of composition of Ce in $Bi_{(4-x)}Ce_xTi_3O_{12}$ .....	38
Table 7. Root mean square roughness of the thin films annealed at 750°C for 1hour as function of amount of composition of Er in $Bi_{(4-x)}Er_xTi_3O_{12}$ .....	38
Table 8. Root mean square roughness of the thin films annealed at 750°C for 1hour as function of amount of composition of Pr in $Bi_{(4-x)}Pr_xTi_3O_{12}$ .....	42
Table 9. Lattice parameter for bare and RE-doped Bismuth Titanate (BIT) .....	42
Table 10. Dipoles moments and ions displacements for REdoped-BIT “ $x=0.55$ ” .....	42

Table 11. Electric response for the bare and RE-doped BIT.....42

## LIST OF FIGURES

Figure 1. Applications of ferroelectric materials.....	3
Figure 2. The perovskite structure ( $ABO_3$ ).....	5
Figure 3. The mechanics of polarization reversal.....	7
Figure 4. Ferroelectric domains and domain-wall in a tetragonal perovskite ferroelectric.....	7
Figure 5. Ferroelectric (P-E) hysteresis loop.....	9
Figure 6. Strain- electric field hysteresis loop in ferroelectric Materials.....	9
Figure 7. The perovskite structure and reversible spontaneous Polarization.....	10
Figure 8. Pseudotetragonal unit cell of $Bi_4Ti_3O_{12}$ and Schematic of SBT.....	11
Figure 9. Schematic of PLD system.....	14
Figure 10. Schematic of deposition by sputtering technique.....	17
Figure 11. Representation of steps in CVD processes.....	18
Figure 12. Schematic representation from Sol to Gel.....	20
Figure 13. Stages of the Spin-Coating process.....	21

Figure 14. Stages of the Dip coating process.....	22
Figure 15. Flow diagram for the preparation of fine powder and thin film by Sol- Gel.....	26
Figure 16. Schematic of the Sol-Gel Process.....	27
Figure 17. X-ray diffraction (XRD) patterns of $\text{Bi}_{(4-x)}\text{Ce}_x\text{Ti}_3\text{O}_{12}$ thin films deposited on Pt/TiO <sub>2</sub> /SiO <sub>2</sub> /Si substrates for the composition (x = 0.00, 0.35, 0.45, 0.55, 0.56, 0.60) annealed at 750°C for 60 min.....	29
Figure 18. X-ray diffraction patterns of $\text{Bi}_{(4-x)}\text{Er}_x\text{Ti}_3\text{O}_{12}$ thin films on Pt/TiO <sub>2</sub> /SiO <sub>2</sub> /Si substrates for the composition (x = 0.00, 0.35, 0.45, 0.55, 0.56, 0.60) annealed at 1 hour 750°C.....	32
Figure 19. XRD diffraction patterns of $\text{Bi}_{(4-x)}\text{Pr}_x\text{Ti}_3\text{O}_{12}$ thin films on Pt/TiO <sub>2</sub> /SiO <sub>2</sub> /Si substrates for different compositions (x = 0.00, 0.35, 0.45, 0.55) annealed at 1 hour 750°C.....	33
Figure 20. Lattice parameters of $\text{Bi}_{(4-x)}\text{Pr}_x\text{Ti}_3\text{O}_{12}$ thin films as a function of composition x.....	34
Figure 21. AFM images in 2D of 1 μ m x 1 μ m areas of $\text{Bi}_{(4-x)}\text{Ce}_x\text{Ti}_3\text{O}_{12}$ thin films deposited on Pt/TiO <sub>2</sub> /SiO <sub>2</sub> /Si substrates annealed at 750°C for 1H..	36
Figure 22. Atomic force microscopy images in 3D of 1 μ m x 1 μ m areas with its respective value of roughness (RMS), of $\text{Bi}_{(4-x)}\text{Ce}_x\text{Ti}_3\text{O}_{12}$ thin films deposited on Pt/TiO <sub>2</sub> /SiO <sub>2</sub> /Si substrates annealed at 750°C for 1H..	37
Figure 23. AFM images in 2D of 1 μ m x 1 μ m areas of $\text{Bi}_{(4-x)}\text{Er}_x\text{Ti}_3\text{O}_{12}$ thin films deposited on Pt/TiO <sub>2</sub> /SiO <sub>2</sub> /Si substrates annealed at 750°C for 1H..	39
Figure 24. AFM images in 3D of 1 μ m x 1 μ m areas with its respective value of roughness (RMS), of $\text{Bi}_{(4-x)}\text{Er}_x\text{Ti}_3\text{O}_{12}$ thin films deposited on Pt/TiO <sub>2</sub> /SiO <sub>2</sub> /Si substrates annealed at 750°C for 1H.....	40
Figure 25. AFM images in 2D of 1 μ m x 1 μ m areas of $\text{Bi}_{(4-x)}\text{Pr}_x\text{Ti}_3\text{O}_{12}$ thin films deposited on Pt/TiO <sub>2</sub> /SiO <sub>2</sub> /Si substrates annealed at 750°C for 1H..	41
Figure 26. AFM images in 3D of 1 μ m x 1 μ m areas with its respective value of roughness (RMS), of $\text{Bi}_{(4-x)}\text{Pr}_x\text{Ti}_3\text{O}_{12}$ thin films deposited on Pt/TiO <sub>2</sub> /SiO <sub>2</sub> /Si substrates annealed at 750°C for 1H.....	42

Figure 27. Typical schematic diagram of a Sawyer-Tower circuit.....	43
Figure 28. Polarization- electric field hysteresis loops for the $\text{Bi}_{(4-x)}\text{Ce}_x\text{Ti}_3\text{O}_{12}$ thin films as a function of Ce contents x.....	45
Figure 29. P-E hysteresis loops BCeT thin films of average thicknesses $0.45 \mu\text{m}$ on Pt (Pt/TiO <sub>2</sub> /SiO <sub>2</sub> /Si) substrates for x= 0, 0.35, 0.45, 0.55, 0.56, 0.6.....	46
Figure 30. Ferroelectric response of the $\text{Bi}_{(4-x)}\text{Er}_x\text{Ti}_3\text{O}_{12}$ thin films on Pt(Pt/TiO <sub>2</sub> /SiO <sub>2</sub> /Si) substrates annealed at 750°C for different concentration of doped.....	47
Figure 31. P-E hysteresis curves of $\text{Bi}_{(4-x)}\text{Er}_x\text{Ti}_3\text{O}_{12}$ thin films as a functions of Er composition x.....	47
Figure 32. x dependence of P-E hysteresis loops for $\text{Bi}_{(4-x)}\text{Pr}_x\text{Ti}_3\text{O}_{12}$ thin films deposited on Pt(Pt/TiO <sub>2</sub> /SiO <sub>2</sub> /Si) substrates.....	48
Figure 33. P-E hysteresis curves of $\text{Bi}_{(4-x)}\text{Pr}_x\text{Ti}_3\text{O}_{12}$ thin films deposited on Pt(Pt/TiO <sub>2</sub> /SiO <sub>2</sub> /Si) substrates as a functions of Pr contents x.....	49
Figure 34. Remnant polarization ( $P_R$ ) as a function of contents of x in $\text{Bi}_{(4-x)}\text{Pr}_x\text{Ti}_3\text{O}_{12}$ thin films.....	50
Figure 35. Vertical schematic of capacitive structure Pt/ $\text{Bi}_{(4-x)}\text{Pr}_x\text{Ti}_3\text{O}_{12}$ /Pt/TiO <sub>2</sub> /SiO <sub>2</sub> /Si ( $\text{Pr} = \text{Ce, Er, Pr}$ ).....	52
Figure 36. Dielectric constant and dissipation factor (loss Tag) of $\text{Bi}_{(4-x)}\text{Ce}_x\text{Ti}_3\text{O}_{12}$ thin films as a function of the frequency and the Voltage.....	53
Figure 37. Variation of dielectric constants and dielectric loss as a function of the Frequency for BErT films with different contents of Er and the Voltage.....	55
Figure 38. The response dielectric dependency of applied frequency for BPrTiO thin films for different contents of Pr.....	56
Figure 39. Schematic diagram for measurement of the leakage current.....	57

Figure 40. The leakage current density as a function of applied electric field, for the $\text{Bi}_{(4-x)}\text{Ce}_x\text{Ti}_3\text{O}_{12}$ thin films deposited on Pt(Pt/TiO <sub>2</sub> /SiO <sub>2</sub> /Si) substrates.....	58
Figure 41. The leakage current Vs Applied electric field at room temperature for the $\text{Bi}_{(4-x)}\text{Er}_x\text{Ti}_3\text{O}_{12}$ thin films deposited on Pt(Pt/TiO <sub>2</sub> /SiO <sub>2</sub> /Si) substrates annealed at 750°C.....	59
Figure 42. Leakage current density for $\text{Bi}_{(4-x)}\text{Pr}_x\text{Ti}_3\text{O}_{12}$ thin films Pt(Pt/TiO <sub>2</sub> /SiO <sub>2</sub> /Si) substrates as a function of the electric field.....	60

## CHAPTER 1

### 1. INTRODUCTION

Ferroelectric materials have been commercially important to the electronic industry for many years, by providing solutions to the problems related to the size of devices and enhanced data storage capacity [34]. These materials are widely used in various types of devices, such as those that use these materials as binary data storage media in which opposite direction of polarization represent the 1 or 0 data bits. In addition, because electric polarization is coupled to the structure of the material, it can convert mechanical energy to electrical energy and vice versa. This latter property leads to the widespread use of this type of materials in transducer applications such piezoelectric [2], actuators and sonar detectors. Besides, the very large dielectric permittivity of ferroelectrics enables them to be applied as capacitors [3].

Ferroelectric materials can be used in the form of bulk, their major applications are in form of thin films, with layers of the order of micrometers. The choice of a proper substrate is very important due to the fact that the interaction between a thin film of a ferroelectric material and the substrate on where it is deposited will determine the corresponding electrical properties. When such a film is integrated into a device, there is an interface between the film and its substrate as well as between the film and one or more electrodes deposited on the ferroelectric material [4]. The basic function of the electrode is to provide electrical contact to the device, for such reason it is very important to select the optimum combination of substrate and electrode. There are a number of criteria which affect the choice of the electrodes, such as: i) the electrode must have sufficiently low resistance, ii) it must display adequate adhesion to both ferroelectric and underlying structure, iii) it must

be morphologically stable under the process conditions, iv) it may need to act as a diffusion barrier of oxygen or other species, v) it must provide suitable interfacial electronic properties, and vi) it may be necessary to utilize the electrode to control the film microstructure or orientation [4].

The most commonly used material for the substrate and base electrode is the platinum. This material is selected because it does not oxidize and has a high solubility for oxygen. However one of the major problems perceived with the performance of platinum electrodes is the fatigue (loss of the switchable remnant polarization as a function switching cycles) in these ferroelectric devices [5]. Also, the platinum exhibits a poor adhesion to SiO<sub>2</sub> substrates and frequently a Pt/Ti/SiO<sub>2</sub>/Si substrate is required to overcome this problem.

Some examples of ferroelectric materials are: perovskite-type [6] that have high dielectric permittivity and can be used in dynamic random access memories (DRAM). In this type of memory the information is stored in the form of charge in a linear capacitor. In order to maintain the stored information secure, a constant voltage is always required on the capacitor which is recharged by a refresh circuitry hundreds of times every seconds, if the power is interrupted the DRAM forgets the information stored in it volatile [7-8].

Besides, the large values of switchable remnant polarization are suitable for nonvolatile ferroelectric random access memories (NVFRAM), here the information is stored in the polarization states ( $\pm P_R$ ) of the ferroelectric material itself. The ferroelectric capacitor has a highly nonlinear dielectric with permanent charge retention capabilities after application of a voltage by an external circuit, therefore the stored information cannot evaporate even when the power is turned off [8]. Other mechanical applications can be see in figure 1.

Taking all this applications into account and the importance of the ferroelectric phenomena are the main motivations for this research. First, we have, synthesized high quality thin films of Bi<sub>(4-x)</sub>Π<sub>x</sub>Ti<sub>3</sub>O<sub>12</sub> (Π = Ce,Er,Pr), using a simple and unexpensive method based on the Sol-Gel process. Next, the necessity to continue studying the behavior of the ferroelectric material when they are doped rare earths.

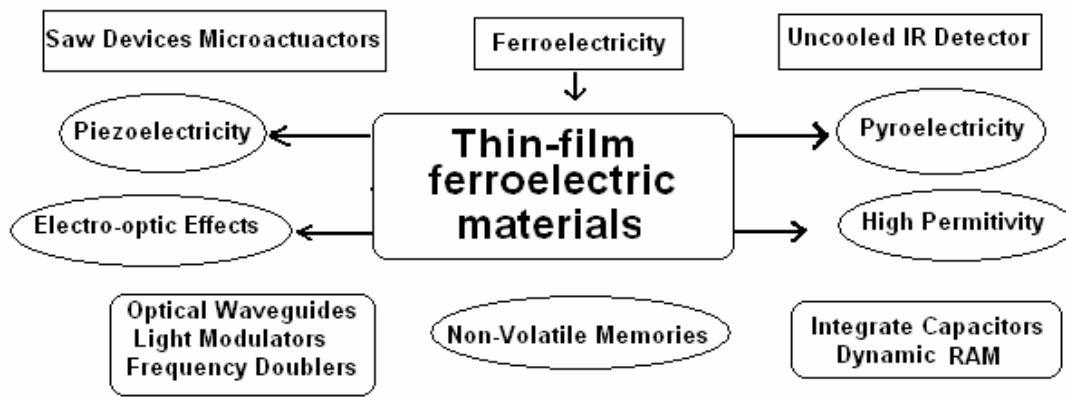


**Figure 1. Applications of ferroelectric materials.**

In this case the ferroelectric material was  $(\text{Bi}_{(4-x)}\Pi_x)^{+3}\text{Ti}^{+4}_3\text{O}^{-2}_{12}$ , doped with Cerium ( $\text{Ce}^{+3}$ ), Erbium ( $\text{Er}^{+3}$ ) and Praseodymium ( $\text{Pr}^{+3}$ ) at different levels. In previous studies of these materials, their doping with other types of rare earths such as Lanthanum (La), Samarium (Sm) and Niobidium (Nd), showed very good results [9].

In the first chapter, the applications of the ferroelectric materials and the fundamental characteristics of ferroelectricity are presented, including the motivation and the specific objectives for this research.

Chapter two is presents a short review of the different methods of synthesis of thin films of high quality. We discussed the advantages, disadvantages of these methods and other results from previous works reported in the literature, with special emphasis on the ferroelectrics of our interest.

Chapter three presents the experimental details of the synthesis of  $\text{Bi}_{(4-x)}\Pi_x\text{Ti}_3\text{O}_{12}$  ( $\Pi = \text{Ce}, \text{Er}, \text{Pr}$ ) powder and thin films, utilizing the Sol-Gel technique. Also, there is a description of the techniques for the structural and electric characterization.

In addition there is a discussion of the precautions when applying these techniques. In chapter four and five, we presented, discuss and analyze the results obtained. Finally, in the chapter six, we present the conclusions and recommendations for future works with these materials.

## 1.1 DEFINITION AND PROPERTIES OF FERROELECTRIC MATERIALS

Ferroelectric compounds are polar materials that possess two equilibrium orientations of spontaneous polarization vector in the absence of an external electric field. This spontaneous polarization vector can be switched between these orientations by application of an electric field.

The polarization associated with a spontaneously formed dipole moment is called spontaneous polarization  $P_s$ . The charge due to the spontaneous polarization is usually masked by charges from the surrounding of the material.

In turn, the change of the vector of the spontaneous polarization with the temperature is defined as the *pyroelectric effect* (it happens when the material is warmed up or cooled down provoking the displacement of the positive ions with respect to the negatives in such a way that the material is polarized electrically) [5].

If the material is polarized electrically due to the application of a unidirectional stress, the phenomenon is called *piezoelectric effect* [10]. Most ferroelectric materials undergo a structural phase transition from a high temperature (paraelectric or nonferroelectric) phase, into a low temperature (ferroelectric) phase (figure 2). The symmetry of the ferroelectric phase is always lower than the symmetry of the paraelectric phase, and the temperature of the phase transition is called the *Curie temperature*  $T_c$ . Above the Curie point the dielectric permittivity falls off with temperature according to the Curie-Weiss law [2]:

$$\varepsilon = \varepsilon_0 + \frac{C}{T - T_0} \approx \frac{C}{T - T_0} \quad (1)$$

Where  $C$  is the Curie constant and  $T_0 \leq T_c$  is the Curie-Weiss temperature [10]. When  $T > T_0$  then the thermal movement destroys the ferroelectric state and the material become paraelectric.

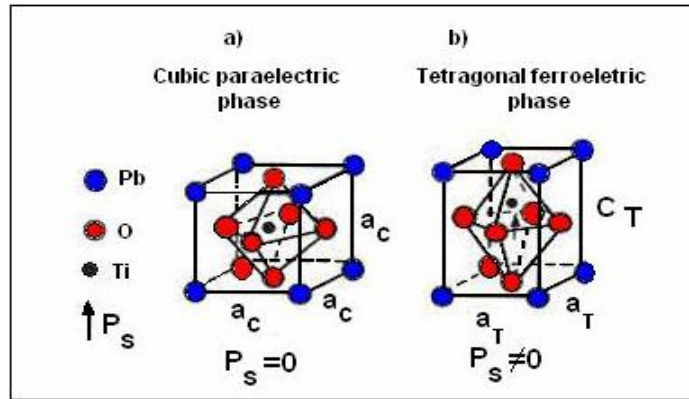


Figure 2. The perovskite structure ( $ABO_3$ ), a)  $PbTiO_3$  in the paraelectric state, b)  $PbTiO_3$  in the ferroelectric state.

The values of Curie temperature for some ferroelectric materials of the perovskite type are given in the table 1. As seen, the ferroelectric effect in the Rochelle or Seignette salt [11] exists within a very narrow region of temperatures.

Table 1. Curie temperature for ferroelectric materials. [10]

Substance	Chemical Formula	Curie Temperature $T_c$ °C
Lithium Niobate	$LiNbO_3$	1200
Lithium Tantalate	$LiTaO_3$	620
Bismuth Titanate	$Bi_4Ti_3O_{12}$	675
Lead Titanate	$PbTiO_3$	490
Potassium Niobate	$KNbO_3$	435
Barium Titanate	$BaTiO_3$	120
Seignette salt	$KN_3C_4H_4O_6 \cdot 4H_2O$	24

### 1.1.1 Ferroelectric Domains

The spontaneous polarization of a grain in a ferroelectric thin film (or ferroelectric crystal) is usually not uniformly aligned throughout the crystal along the same direction. As an example, in lead titanate ( $PbTiO_3$ ) [5-2], the spontaneous polarization lies along the  $c_T$ -axes of the tetragonal unit cell and the crystal distortion is usually described in terms of shifts of oxygen and titanium ions with respect to lead (figure 1.b). In the ferroelectric phase the crystal is spontaneously strained with  $a_T \leq a_c < c_T$  where  $a_T$ ,  $a_c$  are the a-axes of the tetragonal and cubic unit cell, respectively.

The regions of the crystal with uniformly oriented spontaneous polarizations are called ferroelectric domains [10]. In neighboring domains, the spontaneous polarization vector has different directions. These domains were first found in the Barium Titanate [12]. The interaction between neighboring dipoles produces their arrangement in the crystal, which is transmitted from one dipole to another, so that macroscopic regions are polarized in one specific direction. In turn, the onset of the spontaneous polarization at the transition temperature leads to the formation of a surface charge, this surface charge produces an electric field called depolarizing field  $E_d$  [10]; which is oriented oppositely to  $P_s$  and may be very strong (of the order of  $MV^{-1}$ ). Then, the ferroelectric domains will form to minimize the electrostatic energy of depolarizing fields and the elastic energy associated with mechanical constraints to which the ferroelectric material is subjected as it is cooled through paraelectric-ferroelectric phase transition.

The electrostatic energy associated with the depolarizing field, may be minimized if: i) the ferroelectric splits into domains of oppositely oriented polarization, or ii) the depolarizing charge is compensated by electrical conduction through the crystal or by charges from the surrounding material (for example from the atmosphere or the electric circuit to which the material is connected).

Several experimental techniques exist to observe ferroelectric domains, some of them are: the pyroelectric probe technique, electron microscopy, and optical methods. Most of the classical investigations of the domain dynamic during switching have been made on  $BaTiO_3$  [4], by optical methods. When the switching field is applied to the single domain material, new domains start to form at first, mainly at the surface, and they grow through the sample thickness.

After having grown through the sample they begin to expand sideways, the formation of new domains continues to take place as the first ones progress in their sideways expansion. Later they begin to join together on to coalesce until the entire unswitched region is completely overrun by them (Figure 3).

The region between two domains is called the domain wall, the wall which separate domains with oppositely oriented polarization are called  $180^\circ$  walls and

those which separate regions with mutually perpendicular polarization are called  $90^\circ$ walls (figure 4).

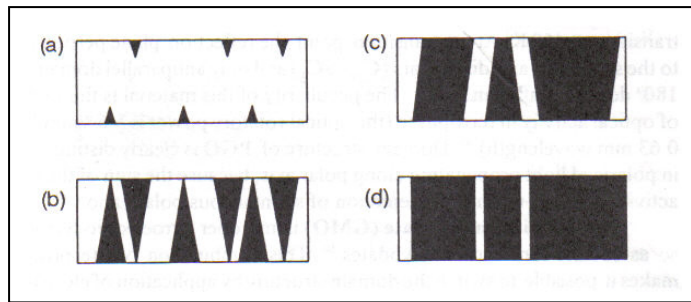


**Figure 3. The mechanics of polarization reversal. a) nucleation of new domains. b) forward growth of the domains through the thickness of the sample. c) sideways expansion of the domains. d) Coalescence of residual domains.**

Due to the complex set of elastic and electric boundary conditions at each grain of the polycrystalline films, they are always split into many domains (figure 4), and can be brought into a polar state by applying a strong electric field (10-100 KV/cm), usually at elevated temperatures. This process called *poling* [9], it cannot orient grains, but can reorient domains within individual grain in the direction of the field.

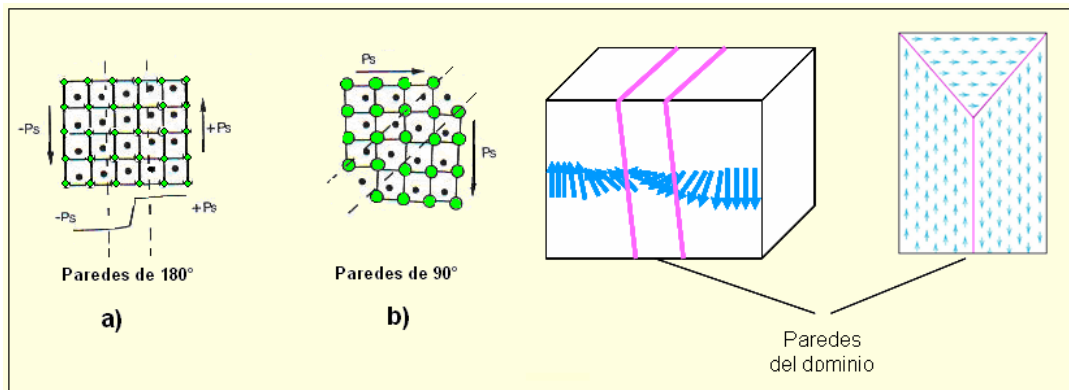


**Figure 4. Ferroelectric domains and domain-wall in a tetragonal perovskite ferroelectric. a)  $180^\circ$  and b)  $90^\circ$ .**

The polarization at zero applied field is called *remnant polarization* " $P_R$ " [2]. The maximum remnant polarization that may be achieved in polycrystalline material depends on available domains states; in a ferroelectric which exhibits only  $180^\circ$  domain walls the maximum remnant polarization is  $0.25 P_s$  (table 2). These values

are ideal assuming reorientation of all domains along available directions dictated by the poling field.

**Table 2. Maximum polarization remnant “ $(P_R)_{\max}$ ” , for some ferroelectric crystalline structures [5].**

Ferroelectric crystalline phase	# available domain states	Maximum polarization remnant $(P_R)_{\max}$
Tetragonal	6	$0.83 P_s$
Rhombohedral	8	$0.87 P_s$
Orthorhombic	12	$0.91 P_s$

The most important characteristic of ferroelectric materials is the polarization reversal or switching, by an electric field [13]. The dependence of polarization on the electric field has the shape of a hysteresis loop and is shown schematically in figure 5. This can be observed experimentally by using the Sawyer-Tower circuit [2].

The field necessary to bring the polarization to zero is called the coercive field “ $E_c$ ”. In an ideal hysteresis loop  $+E_c = -E_c$  and  $+P_R = -P_R$ . There are important differences in the hysteresis loops measured on thin films and bulk ferroelectric of similar composition, some differences are the magnitude of coercive field which may be of greater magnitude in thin films than in the bulk, the loops in films are often more tilted, and the remnant polarization generally is lower in films than in the bulk material.

In thin films the coercive field, spontaneous polarization and shape of the loop may be affected by many factors including the thickness of the film, the presence of charge defect, mechanical stress, preparation condition and thermal treatment. Also, polarization switching by an electric field leads to strain-electric fields hysteresis loop, which resembles the shape of the butterfly (figure 6), and is due to two types of effects: i) the normal converse piezoelectric effect of the lattice, ii) the switching and movement of domains walls.

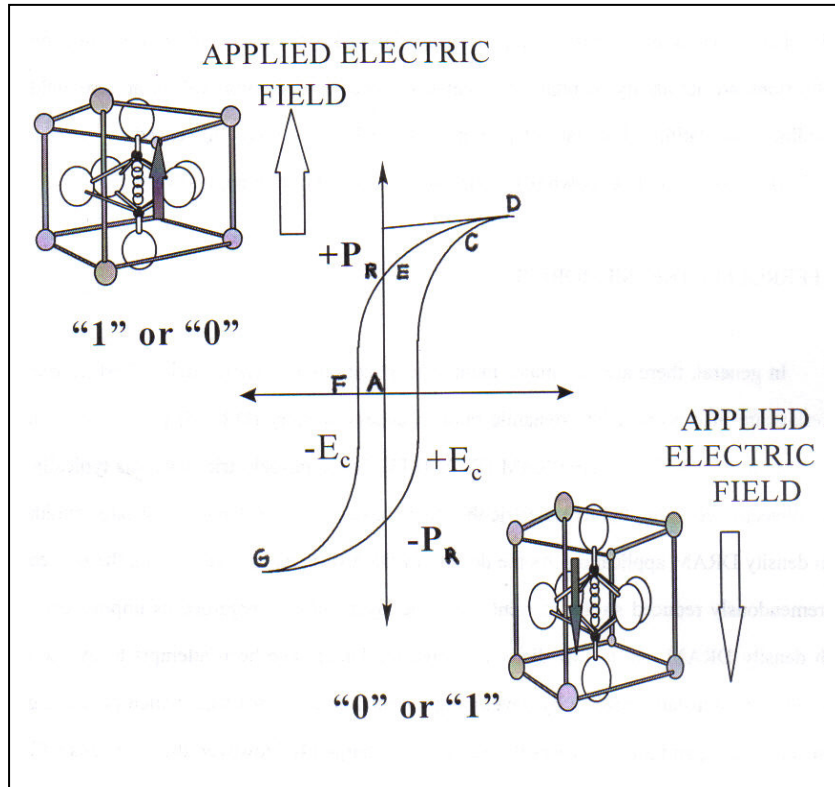


Figure 5. Ferroelectric (P-E) hysteresis loop. Along the measured charge density, the segment (AC) increases rapidly. At Point (C) all the domains are aligned. (D): saturation of domains, (E): remnant polarization. To reach a zero polarization state the field must be reversed (Point F), further increase of the field in the negative direction will cause a new alignment of dipoles at saturation (Point G).

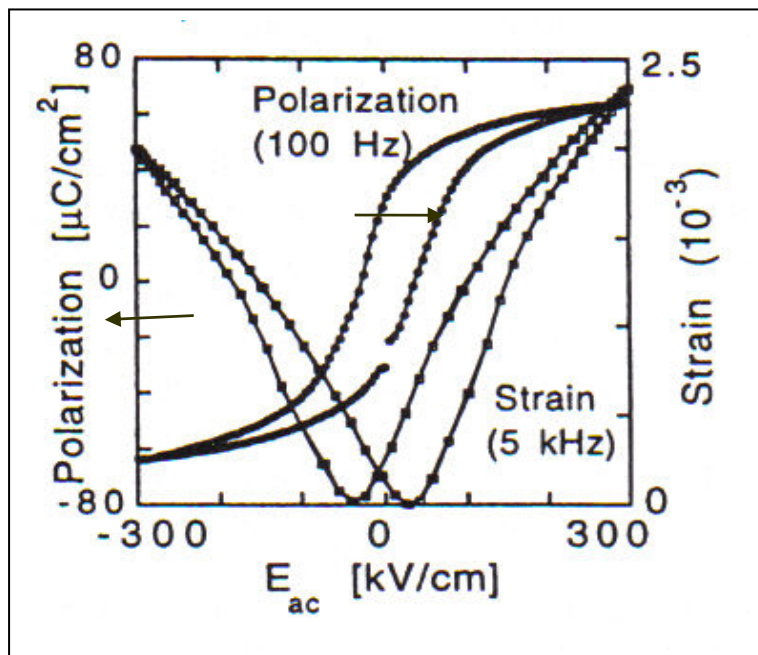


Figure 6. Strain- electric field hysteresis loop in ferroelectric materials. Actual polarization and strain loops measurement on (111)-oriented, sol-gel  $\text{Pb}(\text{Zr}_{0.53}\text{Ti}_{0.47})\text{O}_3$  thin film. (D.V Taylor) [5].

## 1.2 FERROELECTRICITY IN PEROVSKITE AND PEROVSKITE-LIKE LAYERED-STRUCTURES.

The perfect perovskite structure can be represented by the general formula  $ABO_3$ , where the valence of “A” cations varies from +1 to +3 and “B” cations from +3 to +6 (figure 7a). This structure can be viewed as consisting of  $BO_6$  octahedra surrounded by “A” cations. The polarization appears as a result of the small highly charged “B” cation being displaced into a non-centrosymmetric position (figure 7b).

Examples of ferroelectric materials exhibiting this structure are:  $BaTiO_3$  (BT),  $PbTiO_3$  [13-2]. These materials transform from a cubic paraelectric to a tetragonal ferroelectric phase ( $T_c = 120^\circ\text{C}$  and  $T_c = 490^\circ\text{C}$ , respectively) (table 1). At the transition phase temperature oxygen and titanium ions in  $BaTiO_3$  (BT) move in opposite directions, whereas in  $PbTiO_3$  all ions move in the same direction relative to the position of “A” cation at the center of the coordinate system. Ionic shifts are much larger in the  $PbTiO_3$  leading to a larger spontaneous polarization ( $P_S = 57\text{-}75 \mu\text{C}/\text{cm}^2$ ), and the BT ( $P_S = 27 \mu\text{C}/\text{cm}^2$ ) [5].

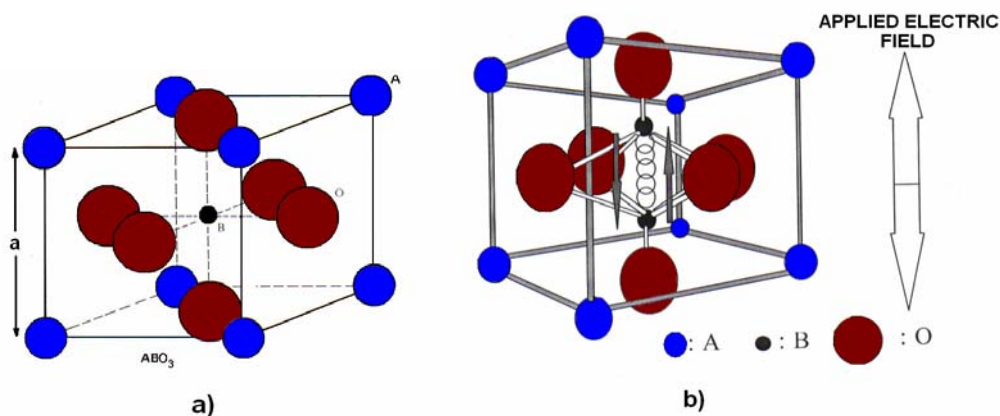


Figure 7. a) The perovskite structure. The “B” cation is at the center of an octahedron of oxygen anions, the “A” cations occupy the unit cell corners. b) Reversible spontaneous polarization.

Other ferroelectric materials belong to the family of Aurivillius- type compounds [14]. The associated structure in these materials consists of perovskite-like blocks  $(A_{n-1}B_nO_{3n+1})^{2-}$  interleaved with  $(BiO_2)^{2+}$  sheets. Here “A” can be mono, di, or trivalent ions or a mixture of them, whereas “B” represents  $Ti^{4+}$ ,  $Nb^{5+}$ ,  $Ta^{5+}$ , etc

[18]. For  $n=2$  we have  $\text{SrBi}_2\text{Ta}_2\text{O}_9$  (SBT) where the crystal structure consist of two perovskite layers O-Ta-O and O-Sr-O chains along the  $c$  axis, alternating with a layer of  $(\text{Bi}_2\text{O}_2)^{2+}$  (figure 8a). For  $n=3$  we obtain  $\text{Bi}_4\text{Ti}_3\text{O}_{12}$  (BIT) =  $\{\text{Bi}_2\text{O}_2\} \cdot \{\text{Bi}_2\text{Ti}_3\text{O}_{10}\}$  [15-16-17], in the  $\text{Bi}_2\text{Ti}_3\text{O}_{10}$  units with Ti enclosed by oxygen octahedral, which are linked through corners forming O-Ti-O linear chains (figure 8b). Bi ions occupy the space in the framework of  $\text{TiO}_6$  octahedral. Thus  $\text{Bi}_2\text{Ti}_3\text{O}_{10}$  units possess a similarity to the perovskite-type structure.

The height of the perovskite-type layers sandwiched between  $\text{Bi}_2\text{O}_2$  layers in  $\text{Bi}_4\text{Ti}_3\text{O}_{12}$  is equal approximately to three perovskite units [18]. In this material the origin of the large polarization within the plane of layers may be traced to a large displacement of  $\text{Bi}^{+3}$  cations in the perovskite “A” sites with respect to the chain of  $\text{TiO}_6$  octahedra, and the small polarization in the direction perpendicular to plane of layers is due to a small displacement of the Ti cation.

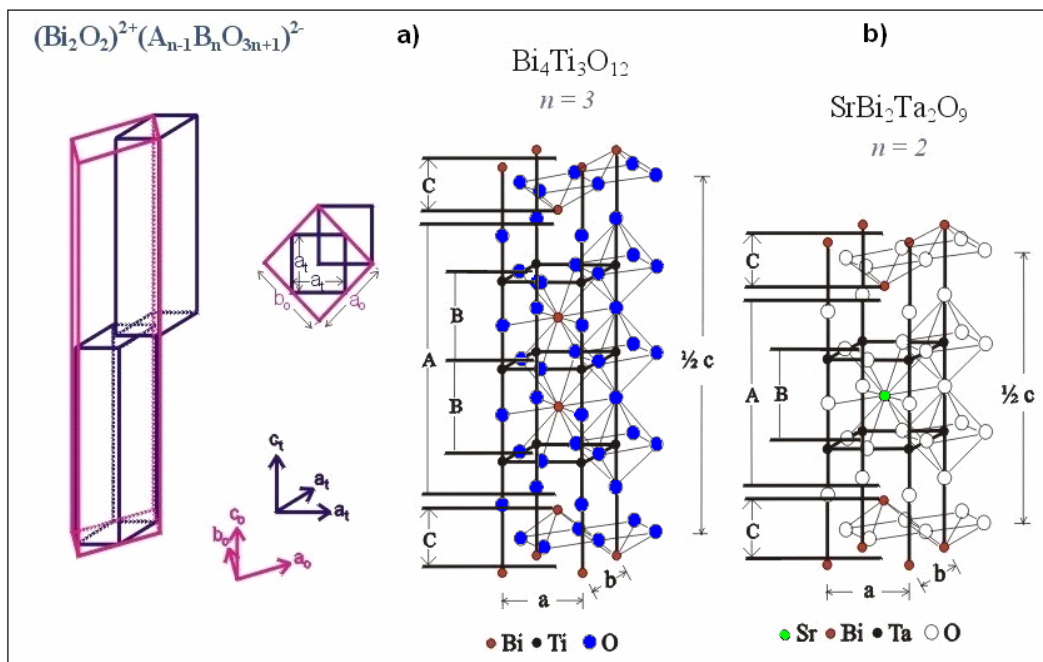


Figure 8. a) Pseudotetragonal unit cell of  $\text{Bi}_4\text{Ti}_3\text{O}_{12}$ . A is the perovskite layer  $\text{Bi}_2\text{Ti}_3\text{O}_{10}^{2-}$ , C is  $\text{Bi}_2\text{O}_2^{2+}$ , and B units cell perovskite structure  $\text{BiTiO}$ . b) Schematic of SBTa.

The lattice parameters of  $\text{Bi}_4\text{Ti}_3\text{O}_{12}$  are  $a=5.4489 \text{ \AA}$ ,  $b= 32.815 \text{ \AA}$ , and  $c=5.4100 \text{ \AA}$  [17]. Nevertheless, these lattice parameters can vary depending of the synthesis methods. The bismuth titanate ( $\text{Bi}_4\text{Ti}_3\text{O}_{12}$ ) has high potential for device

applications because of it is relatively high dielectric constant, high Curie temperature, and high breakdown strength. Recent investigations showed that ion substitution in  $\text{Bi}_4\text{Ti}_3\text{O}_{12}$  may be an effective technique for improving the ferroelectric properties. Takashi et al.[19] reported that the leakage current density of the BIT thin film was large but drastically decreased with the substitution of lanthanide elements, using metal organic chemical vapor deposition, whereas Hirofumi et al. [18] reported that the substitution Bi-site ions in BIT films by  $\text{Pr}^{+3}$  improved the piezoelectric response in this material.

### **1.3 OBJECTIVES IN THIS RESEARCH**

**1.3.1** Synthesize powdered and thin films of earth rare ( $\Pi=\text{Ce, Er, Pr}$ )-substituted bismuth-titanate ( $\text{Bi}_{4-x}\Pi_x\text{Ti}_3\text{O}_{12}$ ) for different compositions of x, deposited on Pt// $\text{TiO}_2$ / $\text{SiO}_2$ /Si substrates using the Sol-Gel technique.

**1.3.2** Characterize this ferroelectric material from its composition, structure and ferroelectric properties viewpoints. For this purpose, x-ray diffraction (XRD), scanning probe microscopy (atomic force microscopy “AFM”), ferroelectric hysteresis, capacitance, dielectric constant and loss tag measurements will be carried out. Measurement of leakage current will also be undertaken.

**1.3.3** Determine the effects of the rare earths (Ce,Er,Pr) substitution in bismuth-titanate films on their electric properties of these films.

## CHAPTER 2

### 2. BACKGROUND INFORMATION: DEPOSITION OF FERROELECTRIC THIN FILMS.

Several methods are in current use for depositing thin films of  $\text{Bi}_4\text{Ti}_3\text{O}_{12}$ , and can be classified into three groups:

#### 2.1 Physical vapor deposition (PVD).

**2.1.1 Pulsed laser deposition (PLD):** The PLD method for thin film growth involves evaporation of a solid target in an ultra high vacuum chamber by means of short and high-energy laser pulses [20]. In a typical PLD process, a ceramic target is placed inside a vacuum chamber. A pulsed laser beam vaporizes the surface of the target, and the vapor condenses on a substrate (figure 9).

The pulsed laser deposition technique involves three main steps: ablation of the target material, formation of a highly energetic plume, and the growth of the film on the substrate. A high-power laser is used as an energy source to vaporize a target containing components of the desired film. When the laser radiation is absorbed by a solid surface, electromagnetic energy is converted into electronic excitation as well as chemical, mechanical, and thermal energy to cause evaporation and plasma formation. The ablation of the target forms a plume of energetic atoms, electrons, ions and molecules. The average kinetic energy of laser-ablated species is typically between 100-1000 kT, where equilibrium energy is on the order of kT. Inside the dense plume, the collisional mean free path is exceptionally small. Immediately after ablation, the plume expands from the target with in vacuum towards the substrate surface.

The main components in a PLD unit are a laser source, optics, and vacuum system. The advantage of using the PLD technique is the ability to preserve the stoichiometry of compound materials, i.e., the deposited film usually has the same chemical structure as the target materials. Also, multilayered structures can be produced. In turn in, addition to the excessive cost, an additional disadvantage of this approach is that the deposition of films on large-area substrates may become a very difficult task.

Kang et al. [21] fabricated thin films of  $\text{Bi}_{3.25}\text{La}_{0.75}\text{Ti}_3\text{O}_{12}$  (BLT) on Pt/TiO<sub>2</sub>/SiO<sub>2</sub>/Si substrate by PLD, these films were deposited at a substrate temperature of 350°C in 200mTorr of oxygen and post-annealed at 700°C in an ambient oxygen for 1h. The thickness of the films was 0.4 μm, the utilized electrode was Au top with a dot size of 2.5x10<sup>-4</sup>cm<sup>2</sup> that was deposited on the film at room temperature by thermal evaporation using and shadow mask. Films produced in this way reported remnant polarization and coercive field varying from 10 to 20 μC/cm<sup>2</sup> and 60 to 90 KV/cm respectively, for applied electric fields between 125 and 325 KV/cm.

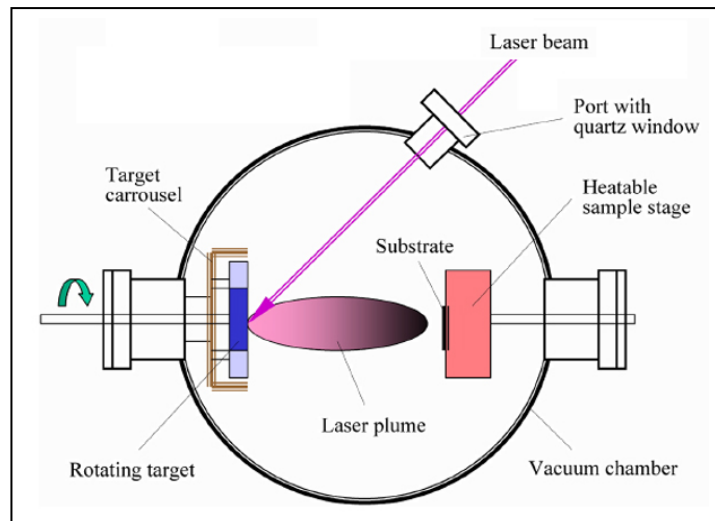


**Figure 9. Schematic of PLD system**

Zhu et al. [22] reported that thin films of the BT-SBTi ( $\text{Bi}_4\text{Ti}_3\text{O}_{12}$ - $\text{SrBi}_4\text{Ti}_4\text{O}_{15}$ ) and BLT-SBTi ( $\text{Bi}_{4-x}\text{La}_x\text{Ti}_3\text{O}_{12}$ - $\text{SrBi}_4\text{Ti}_4\text{O}_{15}$ ) with a thicknesses around 250 and 350 nm fabricated by PLD technique, were deposited on the Pt/TiO<sub>2</sub>/SiO<sub>2</sub>/Si substrates at 400°C, obtaining  $P_R$  values of 12 and 13.5  $\mu\text{C}/\text{cm}^2$  respectively. The fatigue measurement in BT-SBTi film showed serious degradation of the  $P_R$  after 10<sup>6</sup> switching, and therefore it was not considered suitable for the application of FeRAM due its fatigue behavior despite of its large  $P_R$  and a good retention property. The polarization in BLT-SBTi exhibited almost no charge up to 10<sup>10</sup> switching cycles at applied fields above of 250KV/cm (8,9V) indicating that these films had good fatigue resistance for FeRAM applications. In order to improve the fatigue properties of BT-SBTi, Bi was partially substituted by the La.

Garg et al. [23] observed a strong orientation dependence of ferroelectric properties for pulsed-laser ablated  $\{(\text{Bi},\text{Nd})_4\text{Ti}_3\text{O}_{12} (\text{BNdT})\}$  epitaxial films. In contrast, they found that  $P_s=2P_R$  values for BNdT films with orientation further away from  $c$  axis were larger than those of close to the  $c$  axis, with no ferroelectric activity in an (001)-oriented film. Zhang et al. [23] reported that  $P_s$  values of  $c$  axis epitaxial BNdT films grown by pulsed-laser deposition (PLD) were less than 20  $\mu\text{C}/\text{cm}^2$ . It appears then that the growth technique and subsequent processing step played an important role in the film quality.

On the other hand Park et al. [24] reported that the fatigue-free films with excellent ferroelectric properties could be obtained by the substitution of Bi-site ions on  $\text{Bi}_4\text{Ti}_3\text{O}_{12}$  (BIT) film by  $\text{La}^{3+}$  ions. In another case, Noguchi et al. [25] have reported that substitution of Ti-site ion by other ions with higher oxidation states (e.g.,  $\text{V}^{5+}$  and  $\text{W}^{6+}$ ) improved the ferroelectric properties by decreasing the charge density in BIT. Both studies resulted in large  $2P_R$  values over 20  $\mu\text{C}/\text{cm}^2$ , which were considerably higher than that of un-doped BIT thin film.

**2.1.2 Sputtering:** it is based on a vacuum evaporation process which physically removes portions of a material (target), and deposits it film into a substrate (figure 10) [20].

In the sputtering process gaseous ions of plasma are accelerated towards a target consisting of the material to be deposited. Material is detached (sputtered) from the target and afterwards deposited on a substrate in the vicinity. The process is realized in a closed recipient, which is pumped down to the vacuum conditions before deposition starts. To enable the ignition of plasma usually argon is feed into the chamber up to a pressure between 0.5 Pa to 12 Pa. Due to natural cosmic radiations there are always available ionized Ar<sup>+</sup>-ions. In the dc-sputtering a negative potential  $U$  in the order of some hundred volts, is applied to the target. As a result, the Ar-ions are accelerated towards the target and the material is freed. On the other hand secondary electrons are also produced. These electrons cause a further ionization of the gas. The gas pressure  $p$  and the electrode distance  $d$  determine a break-through voltage  $U_D$ , which induces a self sustaining glow discharge according to  $U_D = A \cdot pd / (\ln(pd) + B)$  where A and B are materials-depend constants. Generally speaking, the ionization probability rises with an increase in pressure and hence the number of ions and the conductivity of the gas also increase, whereas the break through voltage drops. For a sufficient ionization rate, a stable burning plasma results wherefrom a sufficient amount of ions is available for sputtering of the material.

The advantage of the sputtering technique is the no need for a laser to produce high-quality thin films.

Yamaguchi et al. [26-27] used planar magnetron sputtering technique to grow thin films of Bi<sub>4</sub>Ti<sub>3</sub>O<sub>12</sub> onto silicon substrate at different temperatures, they observed that the average grain size was increased by increasing the substrate temperature. The thicknesses of the film thin was of 1  $\mu$ m and the dielectric constant was approximately 110 moreover the hysteresis loop showed an apparent remnant polarization and coercive field 2.4  $\mu$ C/cm<sup>2</sup> and 2.3 KV/cm respectively.

Recently Xingsen et al. [28] reported that the microstructure and electric properties of {(Bi<sub>3.15</sub>Nd<sub>0.85</sub>T<sub>3</sub>O<sub>12</sub>) (BNdT)} thin films deposited by RF sputtering were strongly dependent on the excess Bi<sub>2</sub>O<sub>3</sub> content and post-sputtering annealing temperature. For a BNdT with an initial 5 mol% excess of Bi<sub>2</sub>O<sub>3</sub> exhibited a remnant

polarization  $P_s = 2P_R$  of  $25.2 \mu\text{C}/\text{cm}^2$  and coercive field  $2E_c$  of  $161.5\text{KV}/\text{cm}$  at  $9\text{V}$ , together with a dielectric constant of  $304.1$  and dielectric loss of  $0.045$  were reported.

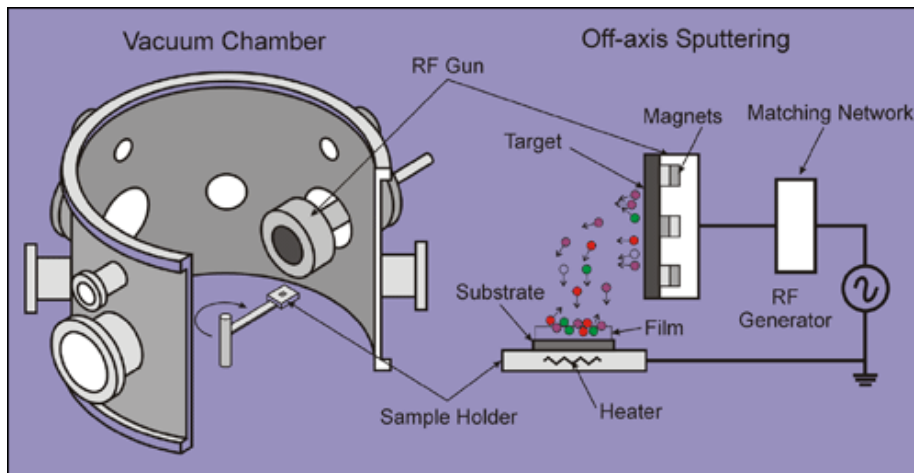


**Figure 10. Schematic of deposition by sputtering technique.**

## 2.2 Chemical Vapor Deposition (CVD):

This technique is used to deposit a film by chemical reaction or decomposition of a gas mixture at elevated temperature on to a wafer surface. In the process CVD [8], film growth occurs through the chemical reaction of component chemicals (i.e., precursors) that are transported to the vicinity of the substrate via the vapor phase. The film-forming chemical reactions typically utilize thermal energy from the heated substrate. The simplest type of CVD involves chemical precursors compounds instead of gases. If liquid- or solid-phases precursors are used, they must have a sufficient vapor pressure to assure an efficient vapor-phase mass transport and mixing. Many organometallic exhibit sufficiently high vapor pressures to be used as CVD precursors in the so-called metal-organic chemical vapor deposition (MOCVD) [4].

The CVD system consists of: a reactor (reaction chamber), gas inlets, gas outlets and a heater. Other CVD-based processes are:

- Vapor phase epitaxy (VPE)-CVD
- Metal-organic Chemical vapor deposition (MOCVD)
- Low pressure Chemical vapor deposition (LPCVD)

- Plasma-enhanced or plasma-assisted Chemical vapor deposition (PECVD or PACVD)
- Laser-induced Chemical vapor deposition (LCVD)

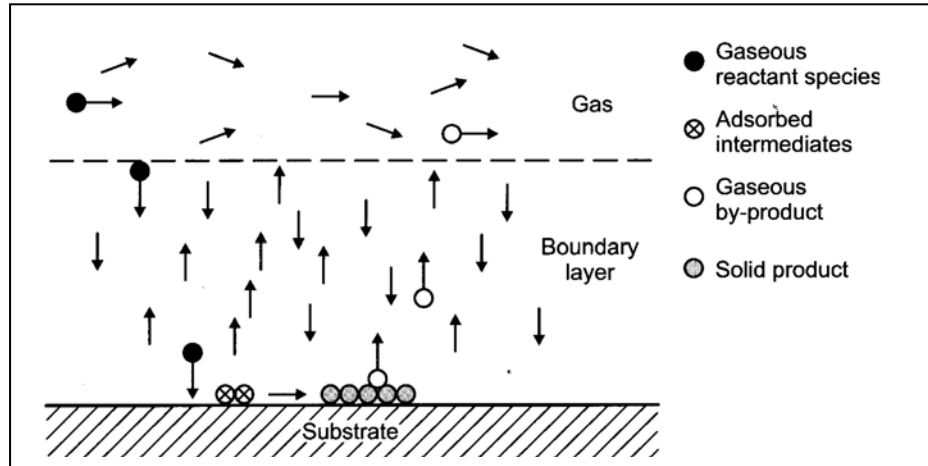


**Figure 11. Representation of steps in CVD processes.**

Takayuki et al. [29] used the MOCVD technique for prepare thin films of  $\text{Bi}_4\text{Ti}_3\text{O}_{12}$  (BIT) and  $(\text{Bi}_{3.5}\text{Nd}_{0.5})(\text{Ti}_{2.97}\text{V}_{0.03})\text{O}_{12}$  (BNTV), where BIT was deposited on a (101)  $\text{TiO}_2$  substrates and BNTV on a (101)  $\text{RuO}_2//$  (012)  $\text{Al}_2\text{O}_3$  substrate. The BNTV film report a remnant polarization of  $24 \mu\text{C}/\text{cm}^2$  and a field coercive of 114 KV/cm, the hysteresis loop did not any significative change after  $1.6 \times 10^{10}$  switching cycles indicating a good fatigue resistance.

Takashi et al. [18] reported that thin films  $(\text{Bi}_{4-x}\text{Ln}_x)\text{Ti}_3\text{O}_{12}$  with ( $\text{Ln} = \text{La}, \text{Nd}, \text{Sm}$ ) fabricated by MOCVD exhibiting a remnant polarization up to  $17 \mu\text{C}/\text{cm}^2$  and 145,135, and 135 KV/cm of coercive field, respectively for dopant fractions ('x') 0.56,0.46,0.13. The films were deposited onto a (111) $\text{SrRuO}_3//$ (111) $\text{SrTiO}_3$  substrates, it was also observed that the substitution of lanthanide elements was quite is effective in decreasing the leakage current densities.

Tomohiro et al. [31] synthetized the  $\text{Bi}_{3.25}\text{La}_{0.75}\text{Ti}_3\text{O}_{12}$  (BLaT) thin films by substituting La with Bi in  $\text{Bi}_4\text{Ti}_3\text{O}_{12}$  (BIT) and using metalorganic chemical vapor deposition (MOCVD). The substitution effectively decreased the leakage current density along the a-b plane. The  $P_s = 2P_R$  values along c-axis and the a-axis were 3.5

and  $38 \mu\text{C}/\text{cm}^2$  respectively. It was suggested that the large remnant polarization was caused by the decrease in the number of defect complexes by La substitution.

H Wangt et al. [32] discussed the effect of grown by the atmospheric pressure in the metal-organic chemical vapor deposition approach. They suggested that the crystalline properties of the films were strongly dependent upon substrate temperature during deposition and annealing temperature. In this work (100) BIT films were grown at  $550^\circ\text{C}$ , whereas a (001) preferred orientation were observed in the films produced at for high-temperature ( $800^\circ\text{C}$ ) annealing.

### 2.3 Chemical Solution Deposition (CSD):

**The Sol-Gel Process:** This route allows the synthesis of materials as ultrafine or spherical shaped powders, thin films coatings, ceramic fibers, microporous inorganic membranes, monolithic ceramic and glasses, or extremely porous aerogel materials. In general, this process involves the transition of a system from a liquid “Sol” (mostly colloidal) into a solid “Gel” phase. The Sol-Gel process can be divided in three stages:

- ◆ Preparation of the Sol:

A sol is a stable colloidal suspension of solid particles in a liquid (aqueous or non-aqueous). In the non-aqueous route, the materials can be formed from metal-organic precursors dissolved in a suitable organic solvent, such as alcohol or other organic acids. The precursor compounds can be colloidal oxides, organic (acetates), or inorganic (nitrates) salts that are dissolved in 2-ethylhexanoic acid, and acetic acid respectively.

- ◆ Gelation :

A gel consists of a liquid trapped by the solid phase. The simplest picture of gelation (figure 12) is represented by the clusters growth by condensation of polymers or aggregation of particles through effective particle-particle collisions.

Then, formed clusters continue growing to produce the final gel. Remaining free-clusters will progressively become connected to the gel network making the stiffness of the gel to increase. The gels are sometimes defined as “strong” or “weak” according to whether the bonds connecting the solid phase are permanent or reversible.

◆ Drying and heat treatment:

The process of drying of a porous material can be divided into several stages. At first the body shrinks by an amount equal to the volume of liquid that evaporates, and the liquid-vapor interface remains at the exterior surface of the body. The second stage begins when the body becomes too stiff to shrink and the liquid recedes into the interior, leaving air-filled pores near the surface. As it invades the pores, a continuous liquid film supports flow to the exterior, so evaporation continues to occur from the surface of the body. Eventually the liquid becomes isolated into pockets and drying can proceed only by evaporation of the liquid within the body and diffusion of the vapor to the outside.

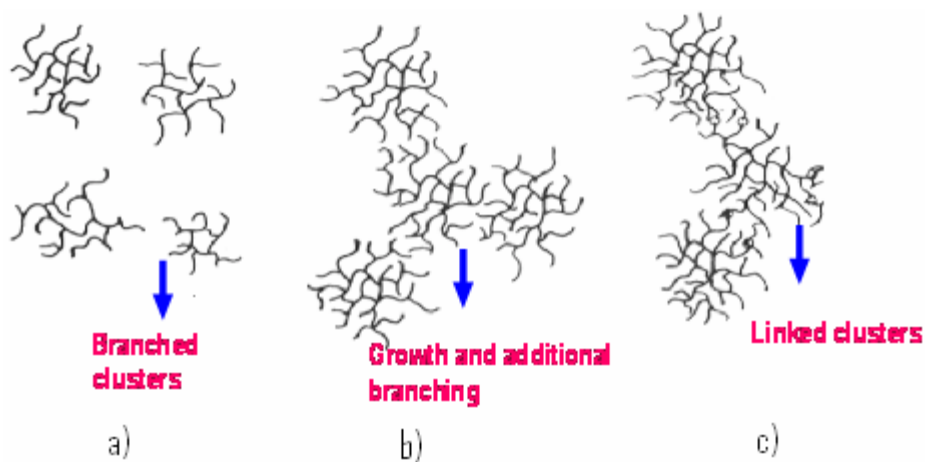


**Figure 12. Schematic representation from Sol to Gel. a) Sol (far from gel point). b) Sol (near gel point). c) Gel point.**

One of the most important features of the Sol-Gel process is its capability to produce thin films. Prior to the gelation and drying, the fluid sol or solution is spread on a piece of substrate by techniques as spinning (spin-coating), dipping (dip-coating), or spraying [33].

**Spin coating:** It is divided in four stages: deposition, spin-up, spin-off, and evaporation of the solvent. First, a suitable excess of the gel must be available onto the surface of the selected substrate during the deposition stage. Next, in the spin-up, stage the gel flows radially outward driven by centrifugal forces. The excess of the gel flows towards the perimeter and leaves the substrate as droplets in the spin-off stage.

As the film thins the rate of removal of excess by spin-off slows down. This effect is because the increase in the resistance of the gel to flow is promoted by the decrease in film thickness. Furthermore, the concentration of nonvolatile component increases raising the viscosity.



**Figure 13. Stages of the Spin-Coating process.**

**The Dip coating technique:** This process divided into five stages, as are immersion, start-up, deposition, drainage, and evaporation (Fig.14). The continuous dip coating is simpler because it separates immersion from the other stage essentially eliminates start-up, and “hides” drainage in the deposited film. The moving substrate entrains liquid in a fluid mechanical boundary layer carrying some of the liquid toward the deposition region, where boundary layer split in two, (Fig. 14.b), the inner layer moves upward with the substrate, while the outer layer is returned to the bath.

Using these technique thin coatings with an excellent adhesion between the metallic substrate and the top coat can be produced. On the other hand, this process is an economic and effective option to produce high quality coatings. Some

limitations of this technique are the low wear resistance, high permeability and difficulty to control the porosity of the deposited films.

Many groups have been using this technique the Sol-Gel with outstanding result. M.S Tomar et al. [1] synthesized thin films of Neodymium-substituted bismuth-titanate ( $\text{Bi}_{4-x}\text{Nd}_x\text{Ti}_3\text{O}_{12}$ ) for different fractions of Nd (x), deposited on Pt// $\text{TiO}_2$ // $\text{SiO}_2$ //Si substrates by spin-coating obtaining a remnant polarization of  $25 \mu\text{C}/\text{cm}^2$  when x was 0.46

Yu-Ming-Sun et al. [35] synthesized thin films of lanthanum-substituted bismuth titanate (BLT for x =0.75) on Pt// $\text{TiO}_2$ // $\text{SiO}_2$ //Si (100) substrate, exhibited a remnant polarization of  $12 \mu\text{C}/\text{cm}^2$  and a field coercive of 78 KV/cm, it was also shown that produced films exhibited a favorable fatigue resistance and charge retention. Following the same strategy, Hirofumi et al. [36] synthesized polycrystalline films substituted  $\text{Bi}_{4-x}\text{Pr}_x\text{Ti}_3\text{O}_{12}$  and determined that the piezoelectric response could be improved for x=0.3.

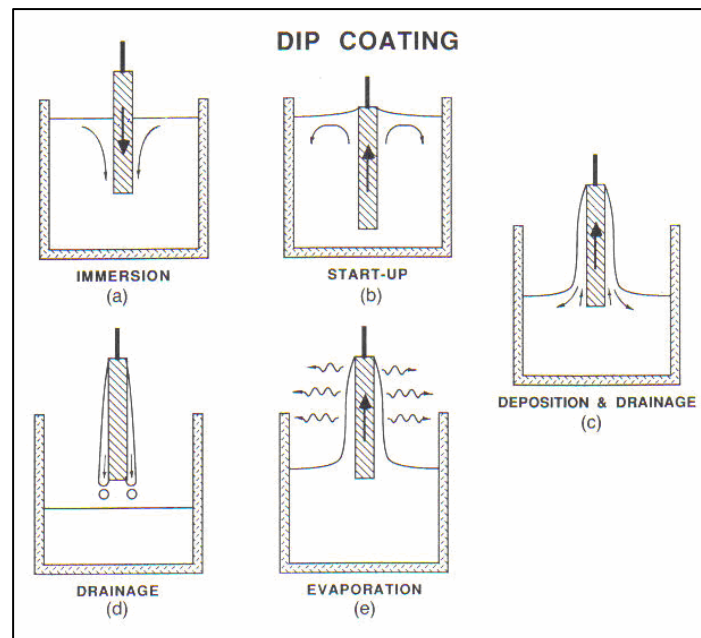


**Figure 14. Stages of the Dip coating process**

Recently Wei et al. [37] had prepared ( $\text{Bi}_{3.15}\text{Nd}_{0.85}\text{Ti}_{3-x}\text{W}_x\text{O}_{12}$ ) thin film on (111) Pt//Ti// $\text{SiO}_2$ //Si substrates using chemical solution deposition technique. They found that a low concentration of donor dopant (x=0.04) efficiently enhanced the

ferroelectric nature whereas and a high dopant concentration deteriorated the ferroelectric nature. Chon et al. [38] have reported very high values of remnant polarization ( $2P_R > 100 \mu\text{C}/\text{cm}^2$ ) in Sol-Gel derived, highly *c*-oriented  $\text{Bi}_{3.15}\text{Nd}_{0.85}\text{Ti}_3\text{O}_{12}$  (BNdT) films. The authors attributed this rather unexpected value to the development of the polarization vector along the *c*-axis in the BNdT unit cell. In undoped BIT, the polarization was almost exclusively along *a*-axis.

J.H.Li et al [39]. Deposited  $\text{Bi}_{3.15}\text{Nd}_{0.85}\text{Ti}_3\text{O}_{12}$  thin films deposited on Pt/Ti/SiO<sub>2</sub>/Si substrates by Sol-Gel method, when the annealing at 750°C temperature, the corresponding grain size varied between 50-100 nm, in the same work, it was observed that the BNdT capacitor fabricated using a Pt top electrode showed well-saturated P-E curves with a the remnant polarization of  $42.5 \mu\text{C}/\text{cm}^2$  under an applied voltage of 7.5 V and, the BNdT capacitors did not show any significant fatigue up  $5 \times 10^9$  read/write switching cycles at a frequency of 1MHz.

Based on the above detailed merits, the present research was focused on the synthesis of targeted ferroelectric materials by using the sol-gel approach.

## CHAPTER 3

### 3. PROCEDURE EXPERIMENTAL

#### 3.1 Solutions preparation

The Sol-Gel approach was used to synthesize targeted materials. Bismuth (III) acetate 99.99% [(CH<sub>3</sub>CO<sub>2</sub>)<sub>3</sub>Bi], Cerium (III) acetate 99.9% [Ce(C<sub>2</sub>H<sub>3</sub>O<sub>2</sub>)<sub>3</sub>.1.5H<sub>2</sub>O], Erbium (III) acetate 99.9% [Er(OOCCH<sub>3</sub>)<sub>3</sub>.4H<sub>2</sub>O] and Titanium (IV) isopropoxide 99.999% [Ti(OCH(CH<sub>3</sub>)<sub>2</sub>)<sub>4</sub>] were used as precursor salts. Acid 2-ethylhexanoic [CH<sub>3</sub>(OH<sub>2</sub>)<sub>3</sub>CH(C<sub>2</sub>H<sub>5</sub>)CO<sub>2</sub>H] and acetic acid [CH<sub>3</sub>CO<sub>2</sub>H] were selected as solvents. To achieve specific compositions in the solid phase (Bi<sub>4-x</sub>Π<sub>x</sub>Ti<sub>3</sub>O<sub>12</sub>), the following formulae was used:

$$\Omega = \frac{(4-x)Bi}{[(4-x)Bi] + [x\Pi] + [3Ti]} \Theta \quad (2)$$

$$\Sigma = \frac{x\Pi}{[(4-x)Bi] + [x\Pi] + [3Ti]} \Theta \quad (3)$$

$$\Gamma = \frac{3Ti}{[(4-x)Bi] + [x\Pi] + [3Ti]} \Theta \quad (4)$$

Where  $\Omega, \Sigma, \Gamma$  are the amounts in grams of Bi,  $\Pi$  (Ce, Er, Pr) and Ti respectively and  $\Theta$ , the total amount of the precursors.

In the next step, bismuth III acetate [(CH<sub>3</sub>CO<sub>2</sub>)<sub>3</sub>Bi], cerium III acetate [Ce(C<sub>2</sub>H<sub>3</sub>O<sub>2</sub>)<sub>3</sub>.1.5H<sub>2</sub>O] or Erbium III acetate [Er(OOCCH<sub>3</sub>)<sub>3</sub>.4H<sub>2</sub>O] and titanium IV isopropoxide [Ti(OCH(CH<sub>3</sub>)<sub>2</sub>)<sub>4</sub>] were dissolved in 2-ethylhexanoic acid [CH<sub>3</sub>(OH<sub>2</sub>)<sub>3</sub>CH(C<sub>2</sub>H<sub>5</sub>)CO<sub>2</sub>H] under room temperature conditions. The obtained solution was placed

in a hot plate pre-heated to 200 °C during approximately 10 minutes or until the organic salts were fully dissolved. The gel produced during heating was filtered through a 0.2  $\mu$  m pore size syringe filters to eliminate any solid impurities.

### **3.2 Thin film preparation**

Substrates of Pt/TiO<sub>2</sub>/SiO<sub>2</sub>/Si were cleaned with distilled water and acetone ACS 99.5% (CH<sub>3</sub>COCH<sub>3</sub>), and dried in a furnace at 400°C for 15 minutes. This cleaning process favored the adherence of the deposited film on the substrate.

Part of the produced gel phase is deposited dropwise onto the cleaned substrate placed in the spin-coating system under 6000 rpm for 20 seconds. The thicknesses of the films are controlled adjusting the speed and the time of the spin as well as the number of the coating sequence. Produced films are placed into the furnace for approximately 10 minutes to ensure complete removal of volatile matter.

This “drying”-spin coating sequence is repeated as many times as needed to thicken the final film.

Finally the dried film was annealed during one hour at 750°C under atmospheric conditions (Figure 15).

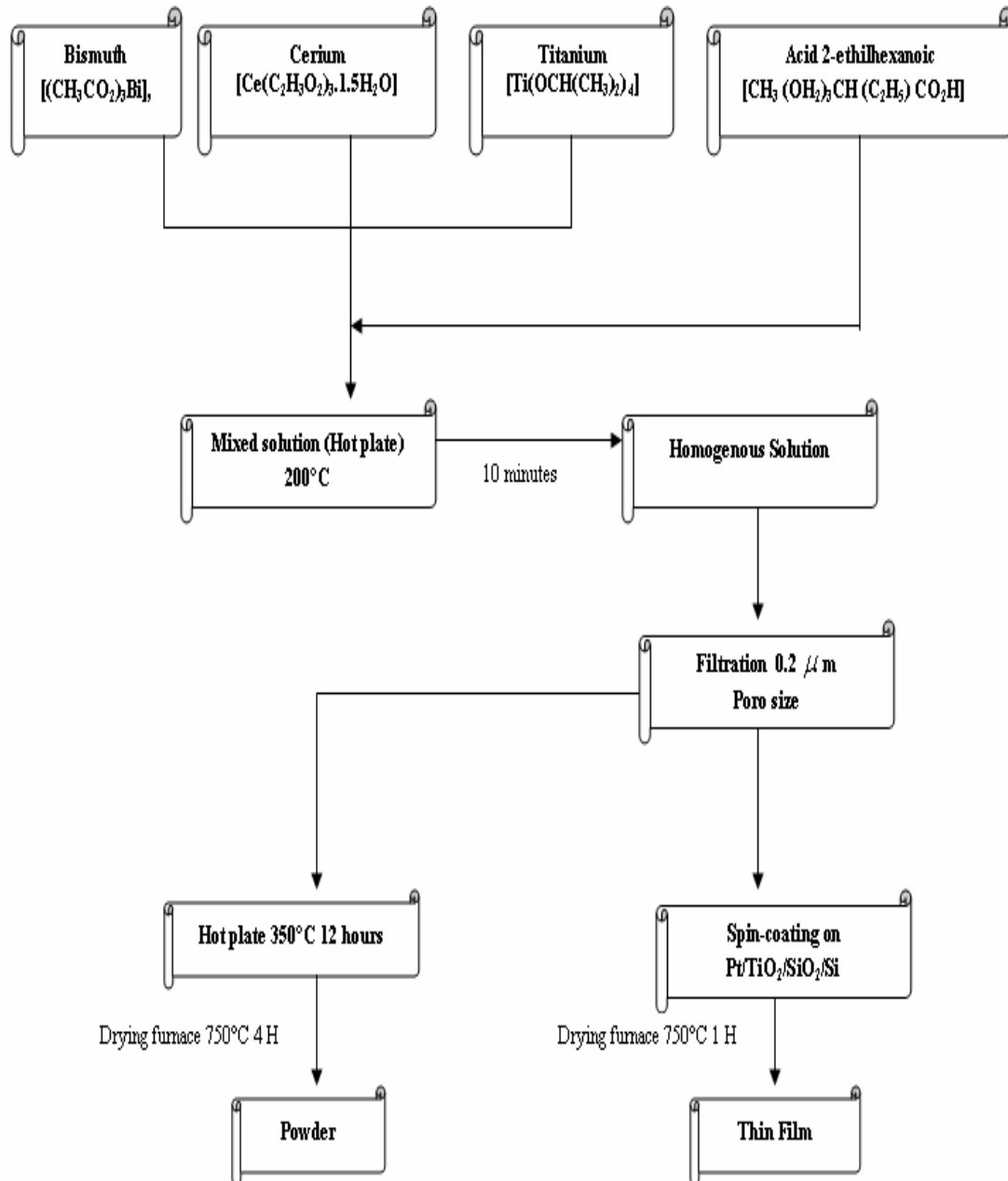


Figure 15. Flow diagram for the preparation of ferroelectric powder and thin film by Sol- Gel.

### 3.3 Powders synthesis

The another fraction of the sol solution was placed in the glass dishes and heated at a 350°C for twelve hours till a powdered solid was produced. The powder product is ground in a mortar and annealed at different temperatures for four or five hours (Figure 16).

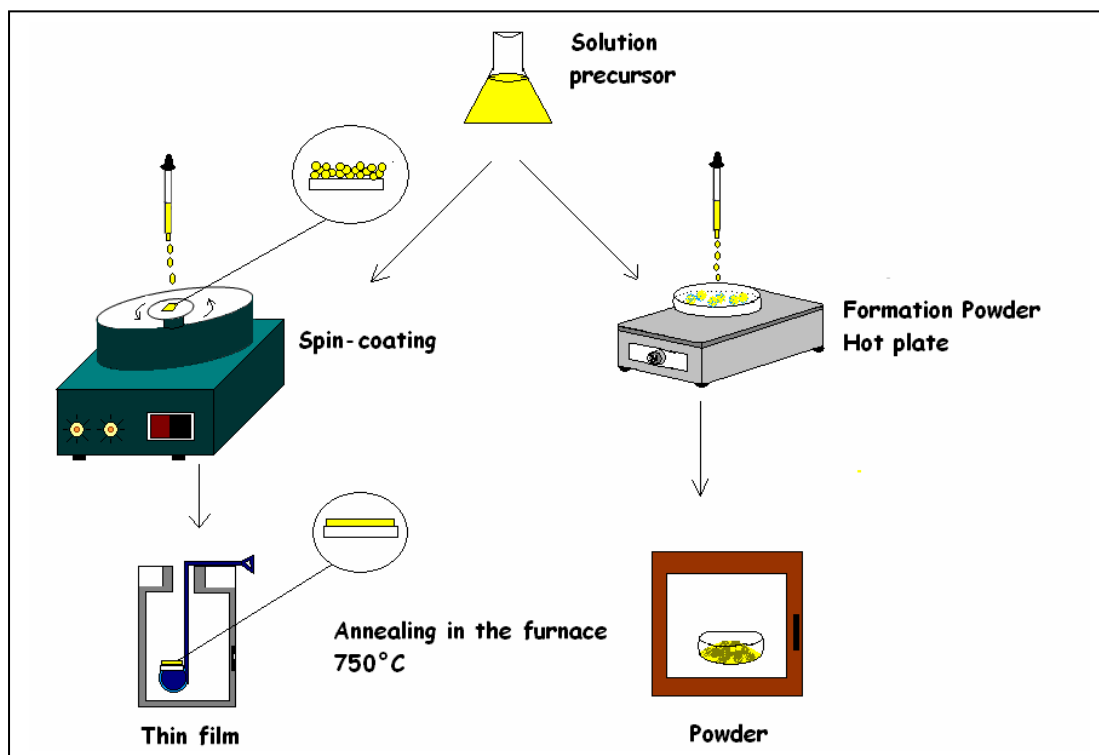


Figure 16. Schematic of the Sol-Gel Process

### 3.4 Safety precautions

The experimental part of this research required the use of harmful compounds and solvents. Therefore, to the wearing of suitable gloves, dressing gown, and goggles become indispensable. Furthermore, were safely placed in plastic containers that were submitted for proper final disposal. Relevant toxicological information about used reagents is detailed as follows:

- ◆ The Bi, Ce, Er acetate are harmful if swallowed or inhaled because affect the liver and kidneys, cause irritation to skin eyes and respiratory tract and lungs.

- ◆ Titanium isopropoxide is a flammable solution that can provoke serious irritation to eyes.

- ◆ The acid 2-ethylhexanoic is a corrosive organic solvent and can cause burns in contact with skin.

In case of direct contact of any of the above mentioned chemicals with eyes, rinse affected areas immediately with plenty of water and seek medical advice. Take off immediately all contaminated clothing, wear suitable protective clothing and eye/face protection.

### **3.5 Characterization of the samples.**

Structural analysis of the powders and the thin films was carried out in Siemens D5000 x-ray diffractometer (XRD) using the Cu K $\alpha$  radiation (0.15405nm). The thicknesses of the films were measured by the reflectance measurement method by a filmetrics F-series. Atomic force microscopy (AFM) technique was used to study the surface morphology of the thin films in contact and no contact (tapping) mode. Electrical measurements were performed using a Pt-ferroelectric-Pt capacitor configuration. These capacitors, were fabricated depositing Pt top electrodes on the surface of the thin film with an area of  $3.14 \times 10^{-4} \text{ cm}^2$  utilizing the masking technique by dc sputtering. The ferroelectric hysteresis loops were measured by a RT6000HVS probe (radiant tech) unit in virtual ground mode. The capacitance, the dielectric constant and loss tag  $\delta$  vs. voltage and frequency were measured with an impedance analyzer HP4294a (in the range from -10V to 10V and 1 KHz to 1MHz) respectively. The variation of the leakage current with applied electric field was determined by using a 6517A electrometer/ high resistance meter. All these measurements were carried out at room temperature.

## CHAPTER 4

### 4. RESULTS AND DISCUSSION

#### 4.1 X-ray diffraction studies

The present thesis reports the structure and ferroelectric properties, of the  $\text{Bi}_{(4-x)}\Pi_x\text{Ti}_3\text{O}_{12}$  films, where  $\Pi = \text{Ce, Er, Pr}$ , deposited on  $\text{Pt/TiO}_2/\text{SiO}_2/\text{Si}$  substrates by the previously described Sol-Gel process.

The structure of the thin films was determined by x-ray diffraction (XRD)  $\theta - 2\theta$  using a Siemens D5000 x-ray diffractometer with the  $\text{Cu K}\alpha$  radiation at 35 Kv and 30 mA at room temperature.

The figure 17 Shows the XRD patterns of the  $\text{Bi}_{(4-x)}\text{Ce}_x\text{Ti}_3\text{O}_{12}$  (BCeT) polycrystalline films. The average films thicknesses were  $0.45 \mu\text{m}$ , for all samples. All peaks correspond to a single phase of bismuth layered-perovskite structure, showing the preferred (117) orientation in addition to (00 $\ell$ ) type peaks of the layered-perovskite [37].

The correlation of the BCeT diffraction peaks with those of BIT implies that  $\text{Ce}^{3+}$  substitution of  $\text{Bi}^{3+}$  does not affect the layered-perovskite structure. Therefore it can be suggested that the  $\text{Ce}^{3+}$  ions, with ion radii of  $1.14 \text{ \AA}$  can substitute for Bi ions (ion radii  $1.03 \text{ \AA}$ ) in the pseudo-perovskite structure without affecting the material structure.

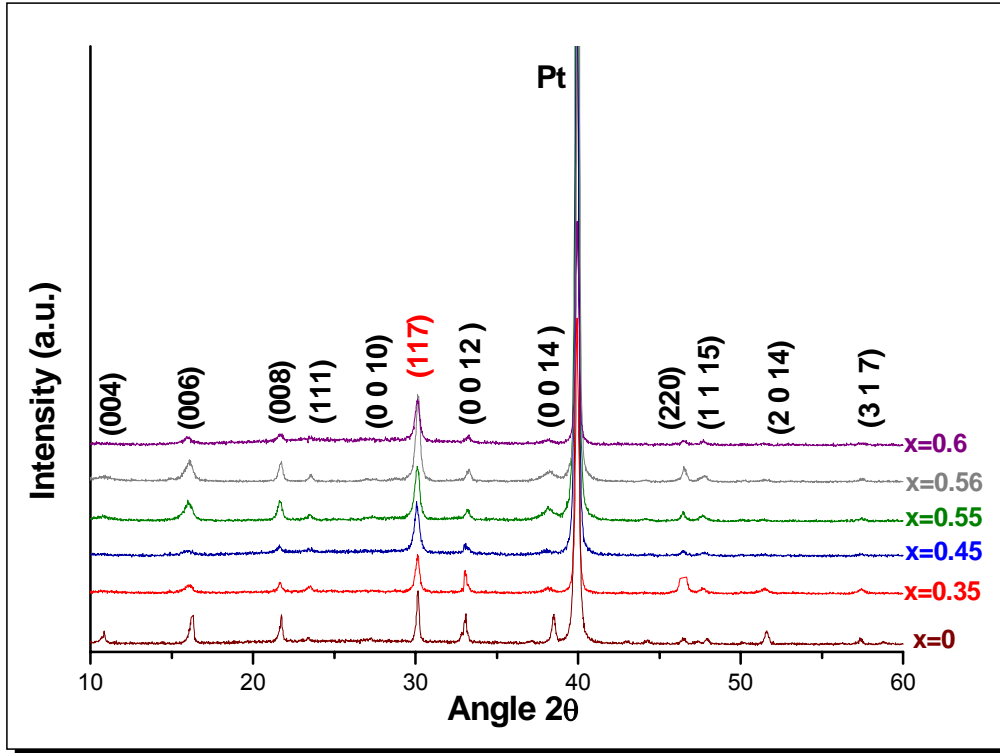


Figure 17. X-ray diffraction (XRD) patterns of  $\text{Bi}_{(4-x)}\text{Ce}_x\text{Ti}_3\text{O}_{12}$  thin films deposited on  $\text{Pt}/\text{TiO}_2/\text{SiO}_2/\text{Si}$  substrates for  $x = 0.00, 0.35, 0.45, 0.55, 0.56, 0.60$  after annealing at  $750^\circ\text{C}$  for 60 min.

The average crystallite size was calculated using the Debye-Scherrer equation<sup>1</sup> (without correction by experimental error) [40]:

$$\langle \tau \rangle = \frac{0.95\lambda}{B \cos \theta} \quad (5)$$

Here  $\langle \tau \rangle$  denotes the size grain,  $\lambda$  the wavelength of XRD diffraction,  $B$  is the full width at half maximum (FWHM) of diffraction peaks in radians and finally have  $\theta$ , the corresponding diffraction angle.

The average crystallite size obtained, it is approximately 24 nm. The lattice parameters “ $a$ ” diminishes, but the parameter “ $c$ ” increase, in comparison with the lattice parameters in the bare  $\text{Bi}_4\text{Ti}_3\text{O}_{12}$ . These values can observe in table 3 and figure 20.

<sup>1</sup> See appendix p-72

**Table 3. Mean size grain of the thin films annealed at 750°C/ 1h as function of amount of composition of Ce in  $\text{Bi}_{(4-x)}\text{Ce}_x\text{Ti}_3\text{O}_{12}$ .**

Composition (x)	Average crystallite size $\tau$ (nm)
0.00	35.23
0.35	24.07
0.45	23.90
0.55	23.53
0.56	34.69
0.60	23.61

The figure 18. Shows the XRD patterns of the  $\text{Bi}_{(4-x)}\text{Er}_x\text{Ti}_3\text{O}_{12}$  (BErT) thin film for varying from 0.45 up to 0.75. All samples were annealed for 60 minutes at 750°C. Other values of “x” were not considered because was observed an unfavorable response of the ferroelectric properties in the thin films.

Corresponding patterns revealed the exclusive formation of well-crystallized layered-perovskite, showing the preference (117) orientation. Therefore Er doping does not affect the basic structure of the BIT, the similitude in ionic radii between  $\text{Er}^{3+}$  and  $\text{Bi}^{3+}$  ( $1.00 \text{ \AA}$  and  $1.03 \text{ \AA}$  respectively) can be involved with this behavior.

The average thickness was approximately of  $0.4 \mu\text{m}$ . The average crystallite size was estimated in 35 nm, this average crystallite size is larger that the 24 nm observed for the  $\text{Bi}_{(4-x)}\text{Ce}_x\text{Ti}_3\text{O}_{12}$  system.

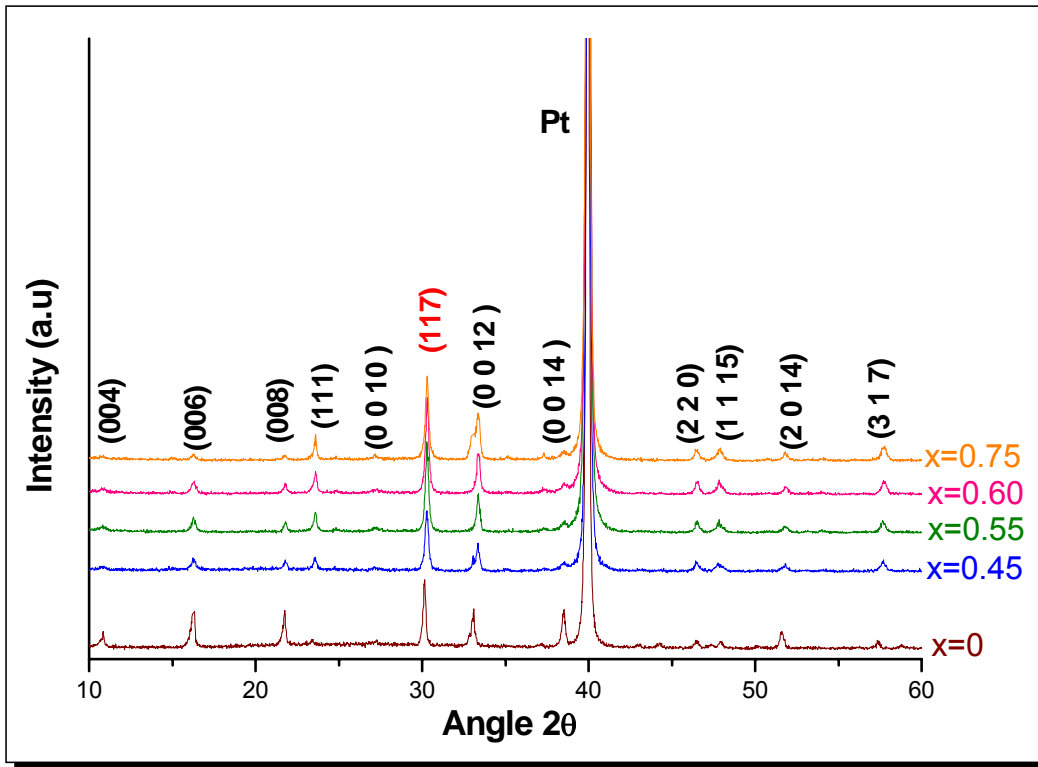


Figure 18. X-ray diffraction patterns of  $\text{Bi}_{(4-x)}\text{Er}_x\text{Ti}_3\text{O}_{12}$  thin films on Pt/TiO<sub>2</sub>/SiO<sub>2</sub>/Si substrates for the composition ( $x = 0.00, 0.35, 0.45, 0.55, 0.56, 0.60$ ) annealed at 1 hour 750°C.

Table 4. Mean size grain of the thin films annealed at 750°C/ 1h as function of amount of composition of Er in  $\text{Bi}_{(4-x)}\text{Er}_x\text{Ti}_3\text{O}_{12}$ .

Composition (x)	Average crystallite size $\tau$ (nm)
0.00	35.23
0.45	36.62
0.55	31.53
0.60	36.60
0.75	34.76

The XRD diffraction spectrum for the thin films of the  $\text{Bi}_{(4-x)}\text{Pr}_x\text{Ti}_3\text{O}_{12}$  system deposited on Pt/TiO<sub>2</sub>/SiO<sub>2</sub>/Si substrates for different compositions ( $x = 0.00, 0.45, 0.55$ ) annealed at 750°C during 1hour is shown in the figure 19. Is clear that the reflection peak corresponded to that exhibited by the  $\text{Bi}_4\text{Ti}_3\text{O}_{12}$  of layered-perovskite, that is the bare material. The thin films are polycrystalline and the most notable characteristics are the predominant (117) oriented for  $2\theta = 30.16^\circ$ ,

Also we can appreciate some (00 $\ell$ ) diffraction peaks, this must be due to the inclusion of Pr<sup>3+</sup> (ion radii of 1.13 Å<sup>0</sup>) in the perovskite block. Replacing Bi<sup>3+</sup> (ion radii 1.03 Å<sup>0</sup>) at the A-site, does not affect the crystal orientation of the BIT.

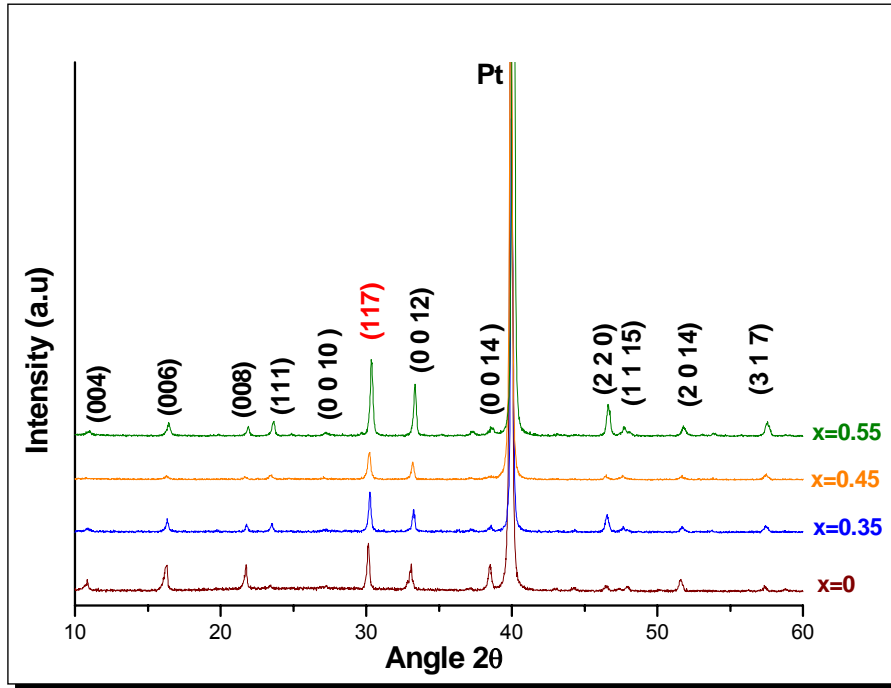


Figure 19. XRD diffraction patterns of Bi<sub>(4-x)</sub>Pr<sub>x</sub>Ti<sub>3</sub>O<sub>12</sub> thin films on Pt/TiO<sub>2</sub>/SiO<sub>2</sub>/Si substrates for different compositions (x = 0.00, 0.35, 0.45, 0.55) annealed at 1 hour 750°C.

The average crystallite size did not change when the fraction dopant increased in the range 0.35-0.55. The average crystallite was estimated in 31 nm.

Table 5. Average crystallite size of the thin films annealed at 750°C/ 1h for different fractions of Pr in Bi<sub>(4-x)</sub>Pr<sub>x</sub>Ti<sub>3</sub>O<sub>12</sub>. the size was estimated by using the Scherrer's equation.

Composition (x)	Average crystallite size $\tau$ (nm)
0.00	35.23
0.35	31.53
0.45	31.48
0.55	31.47

According to literature, single crystals of Bi<sub>4</sub>Ti<sub>3</sub>O<sub>12</sub> exhibit orthorhombic symmetry with lattice parameters  $a = 5.4489 \text{ \AA}$ ,  $b = 32.815 \text{ \AA}$ , and  $c = 5.4100 \text{ \AA}$  [17]

at room temperature, although these values can vary depending on the synthesis methods.

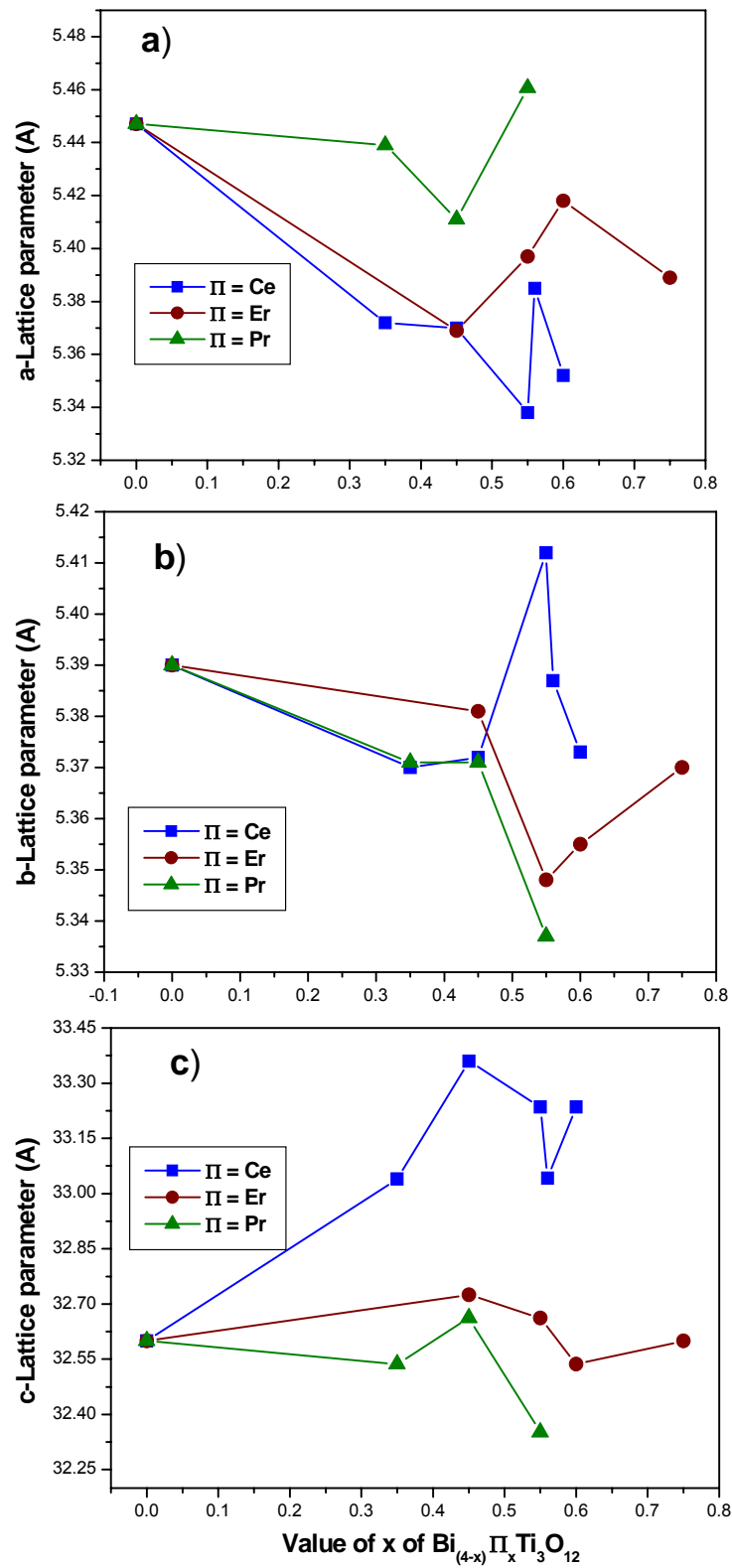


Figure 20. Lattice parameters of  $\text{Bi}_{(4-x)}\Pi_x\text{Ti}_3\text{O}_{12}$  thin films as a function of dopant fraction 'x'.

The figure 20 shows the variations of lattice parameters with the fraction of dopant species (Ce, Er, Pr) “x”. The **c** parameter was computed from (00 $\ell$ ) diffractions for  $\ell = 6$ , whereas the **a** and **b** parameters were obtained from ( $h0\ell$ ) diffractions with  $h = 2$  and  $\ell = 14$ . The orthorhombic distortion **b/a** was 1.013, 0.990, and 0.977 for Ce, Er, and Pr respectively for a composition of  $x = 0.55$ . These ratios are comparable to the unit value reported by Uong C. et al. [41] for the orthorhombic structure of BNdT ( $x = 0.85$ ).

The incorporation of the dopant ions cause the distortion in the unit cell that is verified with the change of the values in the lattice parameters figure 20, suggesting that the difference in the ratios ionic between the Bi ( $1.03 \text{ \AA}$ ) and the dopant species Ce ( $1.14 \text{ \AA}$ ), Er ( $1.00 \text{ \AA}$ ) and Pr ( $1.13 \text{ \AA}$ ) can be the reason for this distortion.

## **.2 Atomic force microscopy (AFM) study**

In order to get information about the morphology, coating effectiveness and surface roughness films of  $\text{Bi}_{(4-x)} \Pi_x \text{Ti}_3\text{O}_{12}$  ( $\Pi = \text{Ce, Er, Pr}$ ) were examined using an atomic force microscope (AFM) in contact mode at room temperature in air. The parameters such as “average roughness (area Ra)”, “root mean square roughness (area RMS)”, “average height” and “maximum Range ( $Z_m$ )” were determined. These parameters are briefly described as follows.

- ◆ *Area Ra (average roughness)*: is the arithmetic mean of the derivations in height from the image mean value.

$$Ra = \frac{1}{n} \sum_{i=1}^N |Z_i - \bar{Z}| \quad (6)$$

Ra is typically used to describe the roughness of machined surfaces. It is useful for detecting general variations in overall profile height characteristic and for monitoring an established manufacturing process.

◆ *Area RMS (root mean square roughness)*: this value is defined as the square root of the mean value of the square of the distance of the points from the image mean value.

$$\text{RMS} = \sqrt{\frac{1}{N} \sum_{i=1}^N \langle Z_i - Z \rangle^2} \quad (7)$$

The root mean square roughness describes the finish of optical surfaces as well as the variation in surface elevation. It is also known as standard deviation of the surface height.

The quantities Ra and RMS are drawn from elementary statistics, but also have a basis in common experience. A surface you would consider to be rough has higher Ra and RMS values than a surface you would consider to be smooth.

◆ *Average Height*: an arithmetic mean defined as the sum of all height values divided by the number of data points.

$$|Z| = \frac{1}{N} \sum_{i=1}^N Z_i \quad (8)$$

Where N is the number of data points within the height profile. This measurement is used as a reference for the Ra and RMS calculations.

◆ *Maximum Range ( $Z_{max}$ )*: is the maximum peak-to-valley range in the area.

Figure 21 shows 2-D AFM images corresponding to  $\text{Bi}_{(4-x)}\text{Ce}_x\text{Ti}_3\text{O}_{12}$  thin films for a scan area of  $1 \mu\text{m} \times 1 \mu\text{m}$ . The films' surfaces were smooth with no presence of cracks.

The films' images also confirmed that the films consisted of nanocrystals as suggested by average crystallite size calculation from XRD patterns. Figure 22

shows the corresponding 3D images including the values of average surface roughness "Ra, RMS and average height. Determined parameters are presented in table 6. As seen, the RMS values are lower than for the base material ( $\text{Bi}_4\text{Ti}_3\text{O}_{12}$ ).

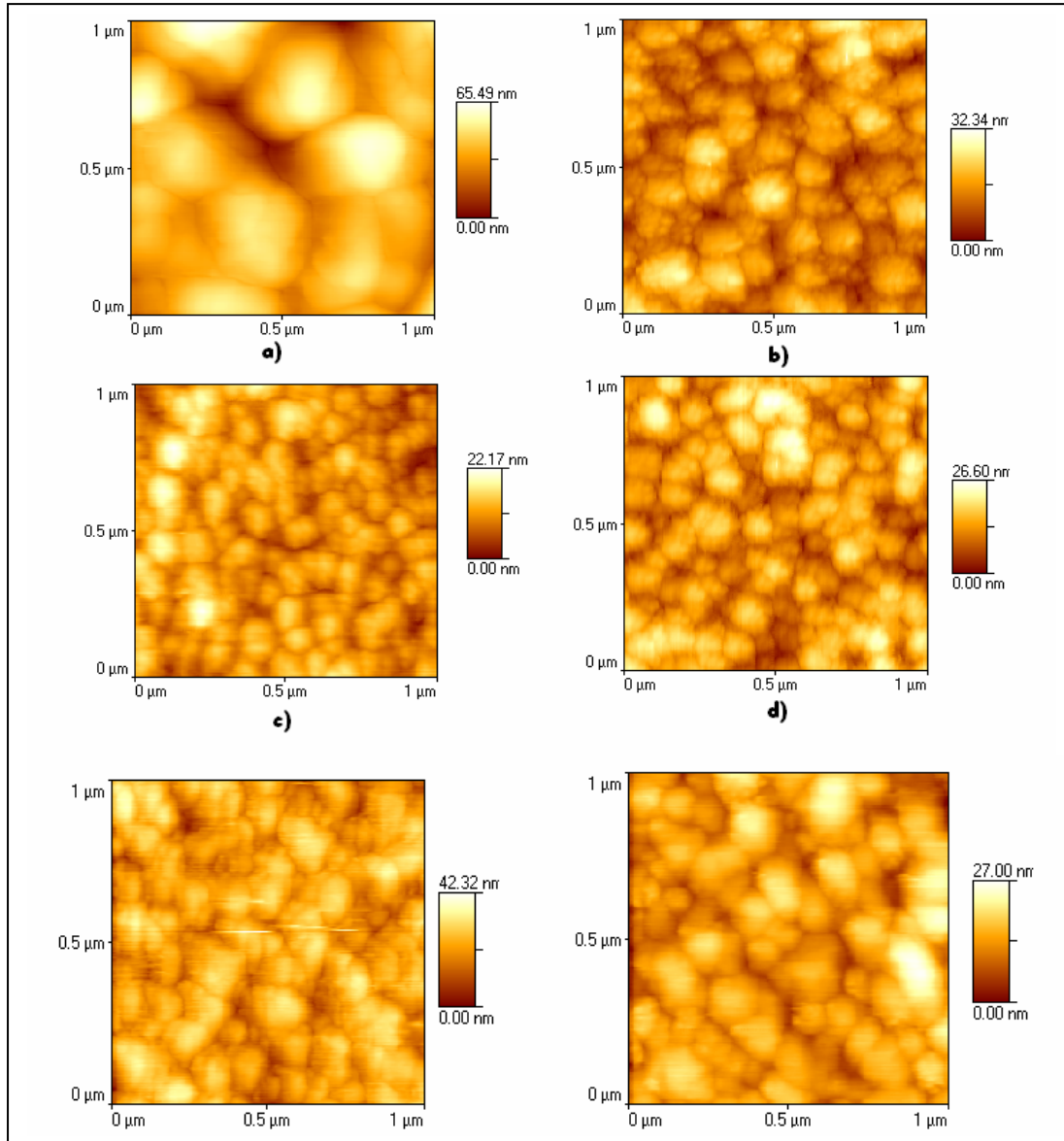


**Figure 21. 2D-AFM images of  $1 \mu\text{m} \times 1 \mu\text{m}$  areas of  $\text{Bi}_{(4-x)}\text{Ce}_x\text{Ti}_3\text{O}_{12}$  thin films deposited on Pt/TiO<sub>2</sub>/SiO<sub>2</sub>/Si substrates and annealed at 750°C for 1 hour. a)  $x = 0$ , b)  $x = 0.35$ , c)  $x = 0.45$ , d)  $x = 0.55$ , e)  $x = 0.56$ , f)  $x = 0.6$ .**

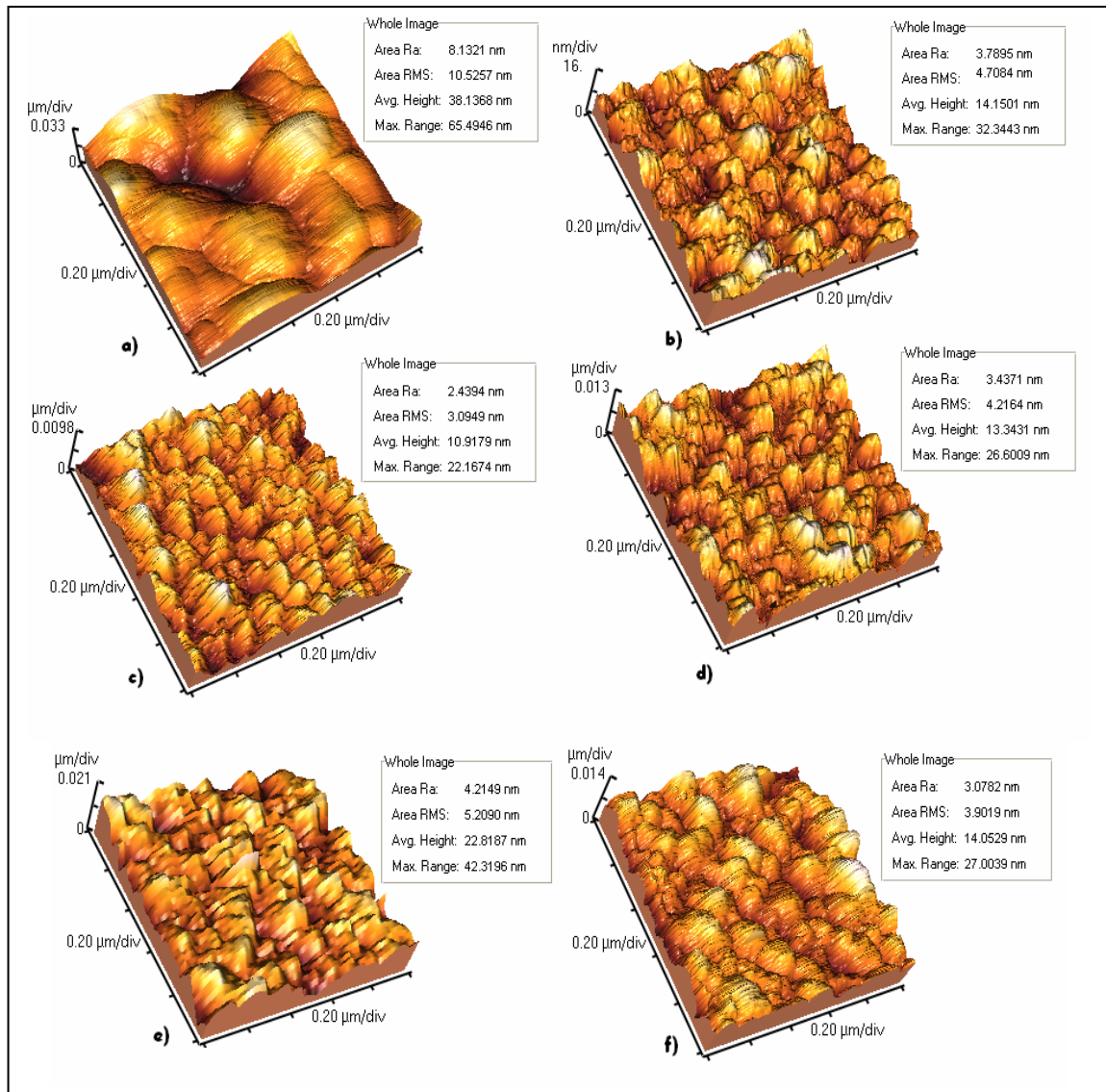


**Figure 22.** 3D-AFM images of  $1 \mu\text{m} \times 1 \mu\text{m}$  areas of  $\text{Bi}_{(4-x)}\text{Ce}_x\text{Ti}_3\text{O}_{12}$  thin films deposited on Pt/TiO<sub>2</sub>/SiO<sub>2</sub>/Si substrates and annealed at 750°C for 1hour. a)  $x = 0$ , b)  $x = 0.35$ , c)  $x = 0.45$ , d)  $x = 0.55$ , e)  $x = 0.56$ , f)  $x = 0.6$ .

The 2D surface morphologies of the  $\text{Bi}_{(4-x)}\text{Er}_x\text{Ti}_3\text{O}_{12}$  thin films are shown in the figure 23. The scanned area was  $1 \mu\text{m} \times 1 \mu\text{m}$ . AFM images suggest that grains in the Er doped BIT films are bigger than in the films doped with Ce. Particle size is in the range 150-200nm. Since this size is far different from the XRD size, a polycrystalline nature can be suggested.

**Table 6. Root mean square roughness (RMS) values of the thin films annealed at 750°C for 1hour as function of fraction molar “x” of Ce in  $\text{Bi}_{(4-x)}\text{Ce}_x\text{Ti}_3\text{O}_{12}$ .**

Composition (x)	Root mean square roughness RMS (nm)	Average height (nm)
0.00	10.52	38.13
0.35	4.70	14.15
0.45	3.09	10.91
0.55	4.21	13.34
0.56	5.20	22.81
0.60	3.90	14.05

The root mean square (RMS) surface roughness and the AFM images in 3D are given in figure 24. BErT thin films exhibited a RMS value larger than in the case of BCeT thin films (table 7). It can be related to the difference between the corresponding particle sizes, which was smaller for the Ce- doped films.

**Table 7. Root mean square (RMS) roughness of  $\text{Bi}_{(4-x)}\text{Er}_x\text{Ti}_3\text{O}_{12}$  thin films annealed at 750°C for 1hour for different Er fractions “x”.**

Composition (x)	Root mean square roughness RMS (nm)	Average height (nm)
0.00	10.52	38.13
0.45	10.36	25.64
0.55	11.11	37.22
0.60	6.95	23.22
0.75	8.04	20.50

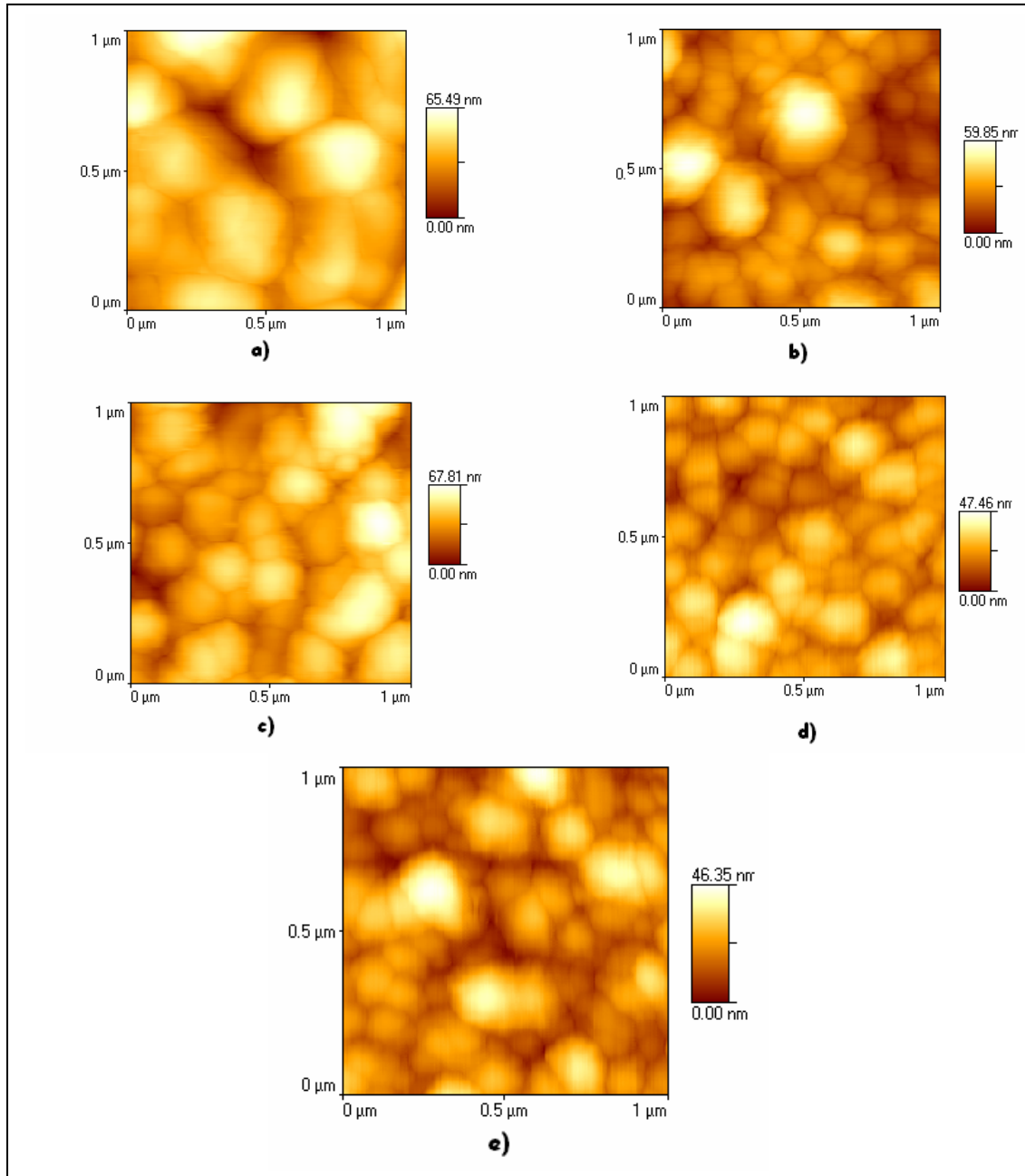
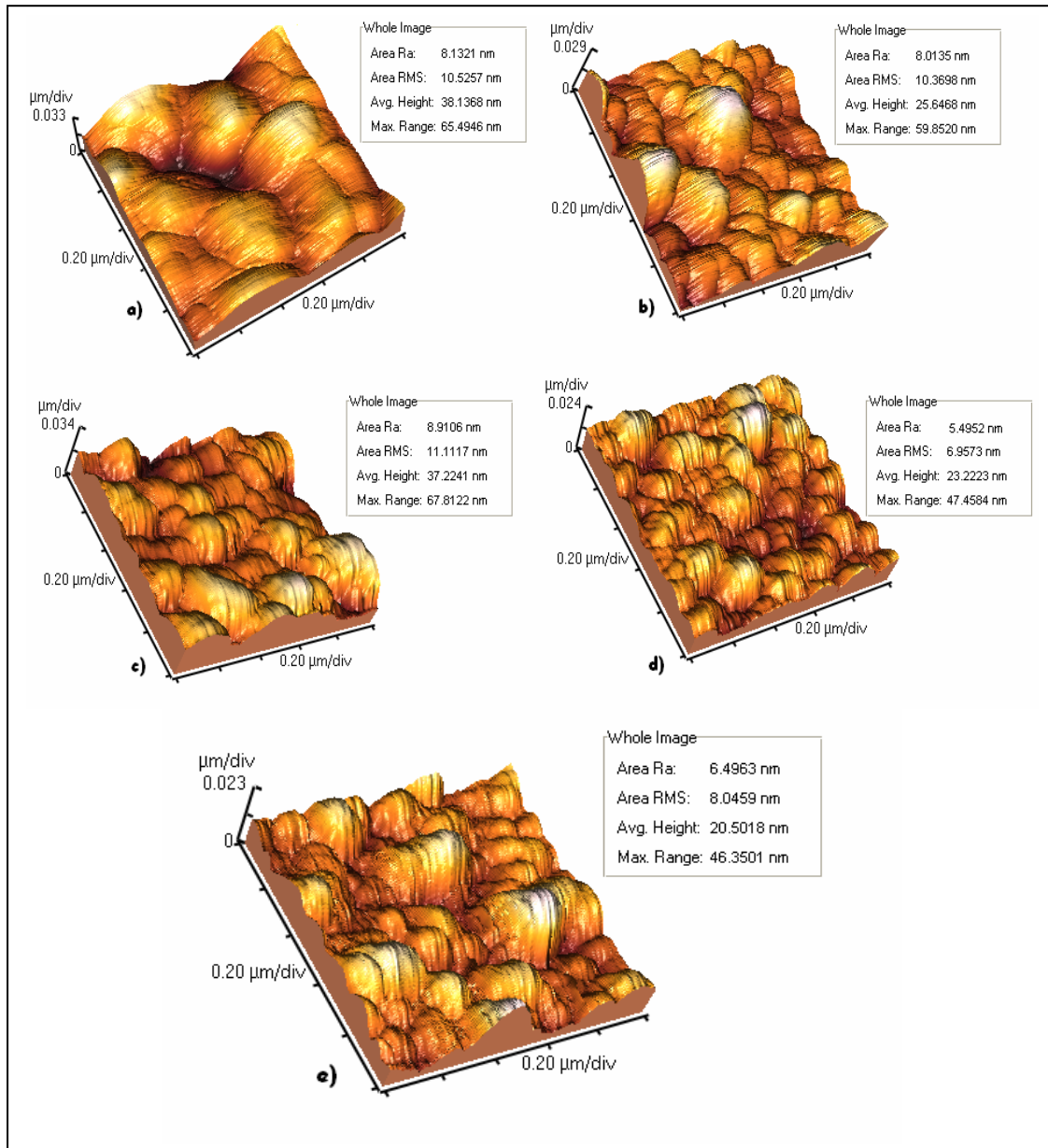


Figure 23. 2D-AFM images of  $\text{Bi}_{(4-x)}\text{Er}_x\text{Ti}_3\text{O}_{12}$  thin films deposited on  $\text{Pt}/\text{TiO}_2/\text{SiO}_2/\text{Si}$  substrates annealed at  $750^\circ\text{C}$  for 1 hour. a)  $x = 0$ , b)  $x = 0.45$ , c)  $x = 0.55$ , d)  $x = 0.6$ , e)  $x = 0.75$ .



**Figure 24.** 3D-AFM images  $\text{Bi}_{(4-x)}\text{Er}_x\text{Ti}_3\text{O}_{12}$  thin films deposited on  $\text{Pt}/\text{TiO}_2/\text{SiO}_2/\text{Si}$  substrates and annealed at  $750^\circ\text{C}$  for 1 hour. a)  $x = 0$ , b)  $x = 0.45$ , c)  $x = 0.55$ , d)  $x = 0.6$ , e)  $x = 0.75$ .

Figures 25 and 26 show the 2D and 3D AFM images of Pr-doped films respectively. The scan area was  $1 \times 1 \mu\text{m}^2$ . The surface morphology did not present crack or defects indicating the deposition of a dense film. Moreover, RMS values (table 8) were greater than for other evaluated system suggesting an irregular deposition of the film.

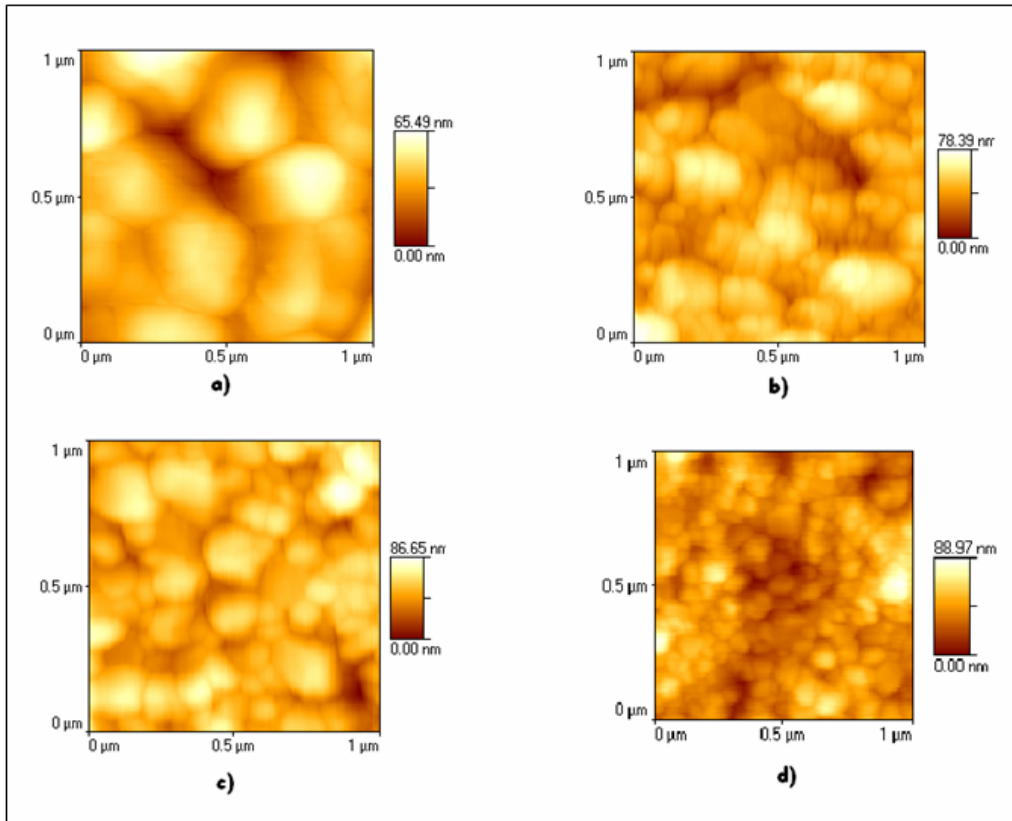


Figure 25. 2D-AFM images of  $\text{Bi}_{(4-x)}\text{Pr}_x\text{Ti}_3\text{O}_{12}$  thin films deposited on  $\text{Pt}/\text{TiO}_2/\text{SiO}_2/\text{Si}$  substrates annealed at  $750^\circ\text{C}$  for 1 hour. a)  $x = 0$ , b)  $x = 0.35$ , c)  $x = 0.45$ , d)  $x = 0.55$ .

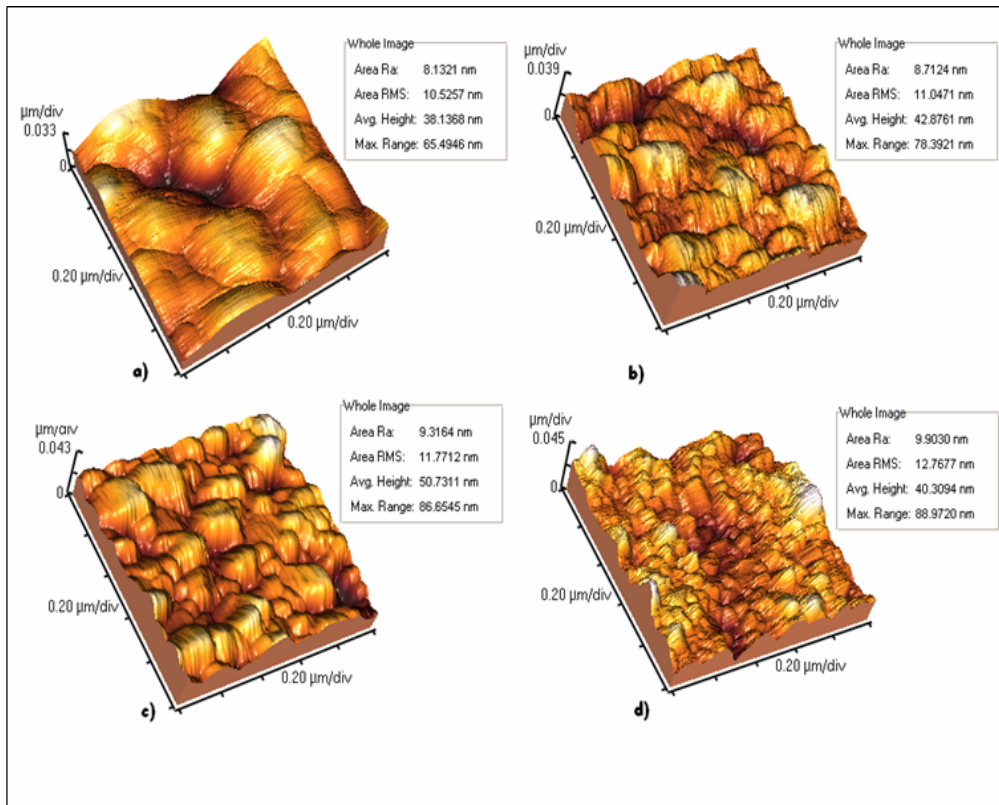


Figure 26. 3D-AFM images of  $\text{Bi}_{(4-x)}\text{Pr}_x\text{Ti}_3\text{O}_{12}$  thin films deposited on  $\text{Pt}/\text{TiO}_2/\text{SiO}_2/\text{Si}$  substrates and annealed at  $750^\circ\text{C}$  for 1 hour. a)  $x = 0$ , b)  $x = 0.35$ , c)  $x = 0.45$ , d)  $x = 0.55$ .

**Table 8. Root mean square (RMS) roughness of the thin films annealed at 750°C for 1 hour as function Pr fraction molar “x” in Bi<sub>(4-x)</sub>Pr<sub>x</sub>Ti<sub>3</sub>O<sub>12</sub> films.**

Composition (x)	Root mean square roughness RMS (nm)	Average height (nm)
0.00	10.52	38.13
0.35	11.04	42.87
0.45	11.77	50.73
0.55	12.76	40.30

### **4.3 Ferroelectric Properties**

The ferroelectric characterization of the synthesized materials was carried out by measuring of the polarization as a function of the applied electric field (hysteresis loop). This type of loop is similar to the magnetic loop (magnetization Vs magnetic field) [42].

The instrument utilized for this measurement is based a Sawyer-Tower circuit [42] that consist of two serially connected components, a ferroelectric capacitor (metal-ferroelectric-metal) “C<sub>F</sub>” and a linear capacitor “C<sub>0</sub>”, being C<sub>0</sub> >> C<sub>F</sub> where an applied voltage of an appropriate wave and an amplitude results in polarization switching of the ferroelectric obtaining a hysteresis loop of figure 27.

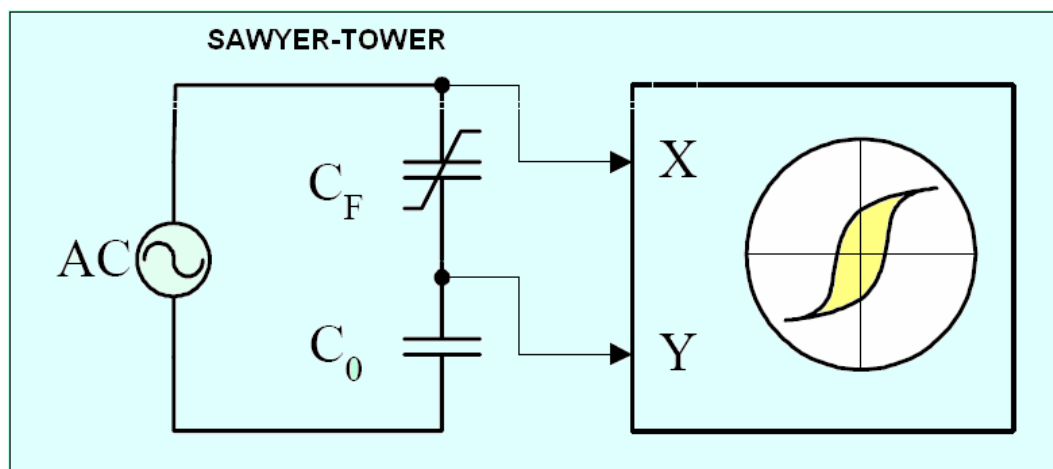


**Figure 27. Typical schematic diagram of a Sawyer-Tower circuit.**

The applied electric field as a function of voltage drop across  $C_F$  and can be expressed as:

$$E = \frac{V_F}{d} \quad (9)$$

$V$  is the applied voltage and  $d$  is the thicknesses of ferroelectric thin films in centimeters. The experimental results of ferroelectric P-E hysteresis loops were conducted on films in a metal-ferroelectric-metal (Pt-film-Pt) capacitor configuration at room temperature in air, using RT 6000HVS probe (radiant technologies) in virtual ground mode.

Figure 28 shows the polarization-electric field (P-E) hysteresis curves, remnant polarization and coercive field of  $\text{Bi}_{(4-x)}\text{Ce}_x\text{Ti}_3\text{O}_{12}$  thin films deposited on Pt/TiO<sub>2</sub>/SiO<sub>2</sub>/Si substrates and annealed at 750°C temperature for different fractions of dopant species ( $x=0.35$ ,  $x=0.45$ ,  $x=0.55$ ,  $x=0.56$ ,  $x=0.6$ ). Corresponding remnant polarization  $P_R$  values were  $5.1 \mu\text{C}/\text{cm}^2$ ,  $17.2 \mu\text{C}/\text{cm}^2$ ,  $27.5 \mu\text{C}/\text{cm}^2$ ,  $21.28 \mu\text{C}/\text{cm}^2$ ,  $16.8 \mu\text{C}/\text{cm}^2$  and a coercive field of 212 KV/cm, 162 KV/cm, 210 KV/cm, 177 KV/cm, 187.7 KV/cm respectively.

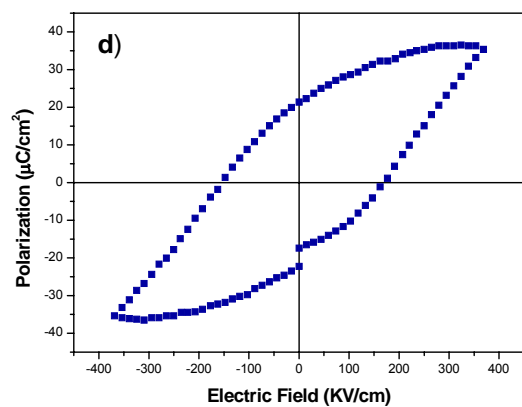
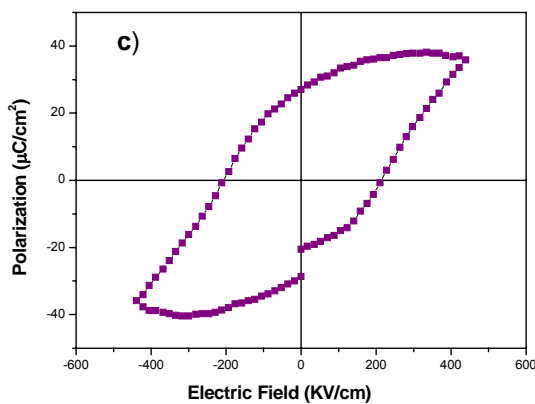
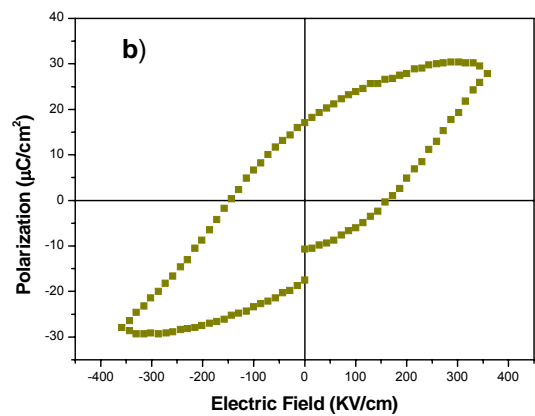
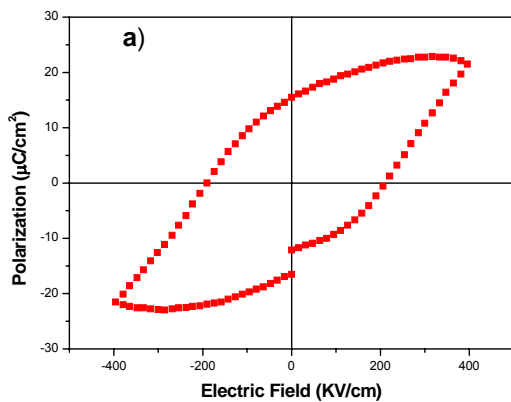
As evidence by obtained results, the best combination of remnant polarization and coercive fields ( $75.5 \mu\text{C}/\text{cm}^2$  and 210KV/cm, respectively) were achieved for a Ce fraction of 0.55, under an applied electrical field of 440 KV/cm.

This attributed to the enhanced crystallinity and small size grain observed in this film. The presence of dopant species (Ce) in the Bi site suggest the existence of a high asymmetry in the host structure, because the difference between the values of the ionic radii causes a displacement of the central Ti ion in TiO<sub>6</sub> octahedron unit with respect of the six surrounding oxygen. This indicates the polarization vector increase along the  $c$  axis.

Figure 29 compares the hysteresis loops of the  $\text{Bi}_{(4-x)}\text{Ce}_x\text{Ti}_3\text{O}_{12}$  films with the one corresponding to the base material  $\text{Bi}_4\text{Ti}_3\text{O}_{12}$ . Evidently, the substitution of  $\text{Bi}^{3+}$  for  $\text{Ce}^{3+}$  in the perovskite-layers structure favors the enhancement of the ferroelectric

properties. The reason behind this effect would be a synergistic effect between these two ionic species which would have promoted a large tilting of  $\text{TiO}_6$  octahedra in the layered structure. However, the synergistic effect is strongly dependent of atomic ratio Bi/Ce. Ce addition larger than 0.55 became deleterious to the ferroelectric behavior of the material, probably because of an enhanced instability of the perovskite-layer structure and/or limited solubility Ce into base structure.

On the other hand the small mismatch and the end of the hysteresis loops can be attributed to the adhesion problem of top Pt contact electrodes. A possible solution to this problem would be the post annealing of the electrodes, before measurement. This loop mismatching can also may be due to the relatively high values in leakage current observed for these films.



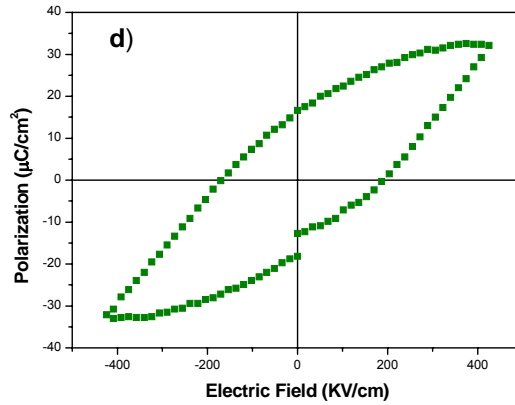


Figure 28. Polarization- electric field hysteresis loops for the  $\text{Bi}_{(4-x)}\text{Ce}_x\text{Ti}_3\text{O}_{12}$  thin films as a function of Ce contents x. a)  $x=0.35$ , b)  $x=0.45$ , c)  $x=0.55$ , d)  $x=0.56$ , e)  $x=0.6$ .

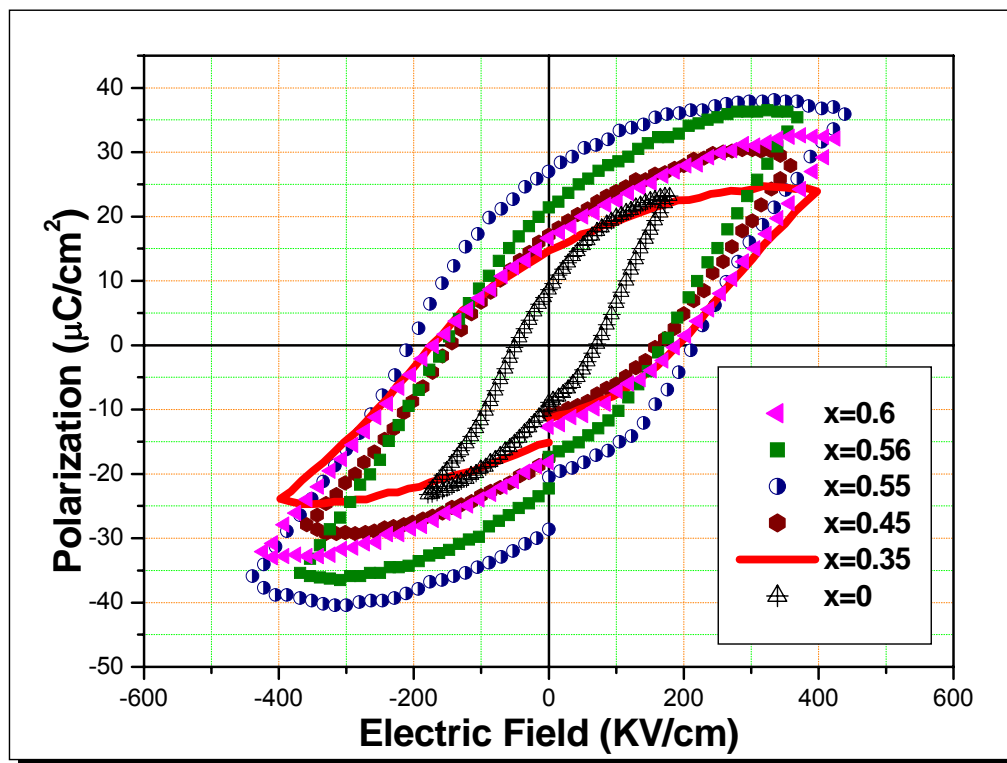


Figure 29. P-E hysteresis loops BCeT thin films of average thicknesses  $0.45 \mu\text{m}$  on Pt ( $\text{Pt}/\text{TiO}_2/\text{SiO}_2/\text{Si}$ ) substrates for  $x=0, 0.35, 0.45, 0.55, 0.56, 0.6$ .

The P-E hysteresis loop of  $\text{Bi}_{(4-x)}\text{Er}_x\text{Ti}_3\text{O}_{12}$  thin films are showed in figure 30. The obtained remnant polarization and coercive field vales were  $15.15 \mu\text{C}/\text{cm}^2$  and  $172.52 \text{KV}/\text{cm}$  for  $x=0.45$  (fig.30a.),  $22.82 \mu\text{C}/\text{cm}^2$  and  $195.73 \text{KV}/\text{cm}$  for  $x=0.55$  (fig.30b.),  $12.13 \mu\text{C}/\text{cm}^2$  and  $230.36 \text{KV}/\text{cm}$  for  $x=0.6$  (fig.30c.),  $10.95 \mu\text{C}/\text{cm}^2$  and  $225.84 \text{KV}/\text{cm}$  for  $x=0.75$  (fig.30d.) respectively. All measurement was carried out under maximum applied field of  $500 \text{KV}/\text{cm}$ . As seen, the loops were not saturated

even at an applied field as high as 500 KV/cm, but the polarization value is greater than that for  $x=0$  (figure 31). The poor saturation exhibited by the hysteresis loops can be due to two factors. First, limitations of the measuring instrument itself in the sense it cannot reach voltages greater of 20V, i.e. a field greater of 500 KV/cm, second the probable of oxygen vacancies in the structure [5].

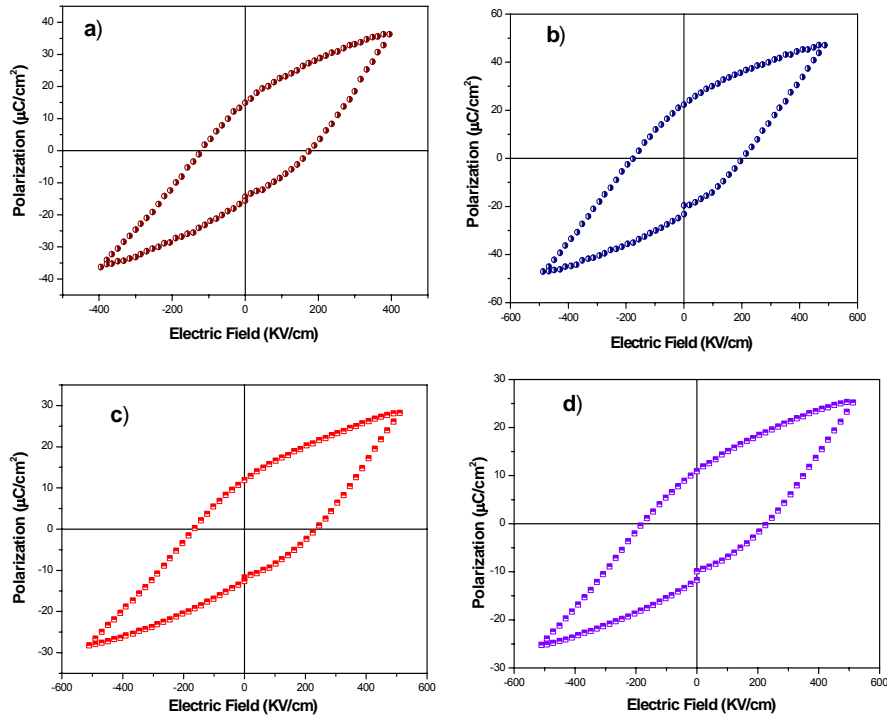


Figure 30. Ferroelectric response of the  $\text{Bi}_{(4-x)}\text{Er}_x\text{Ti}_3\text{O}_{12}$  thin films on Pt(Pt/TiO<sub>2</sub>/SiO<sub>2</sub>/Si) substrates annealed at 750°C for different concentration of doped. a)  $x=0.45$ , b)  $x=0.55$ , c)  $x=0.6$  and d)  $x=0.75$

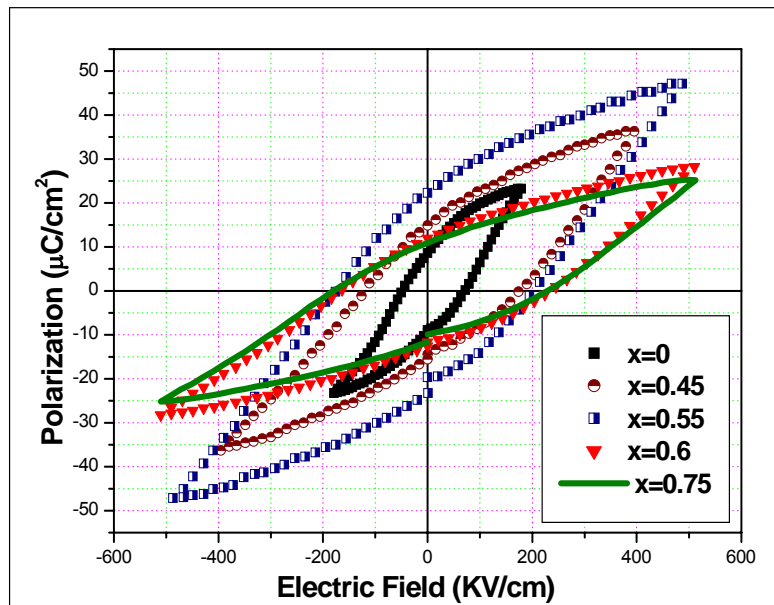
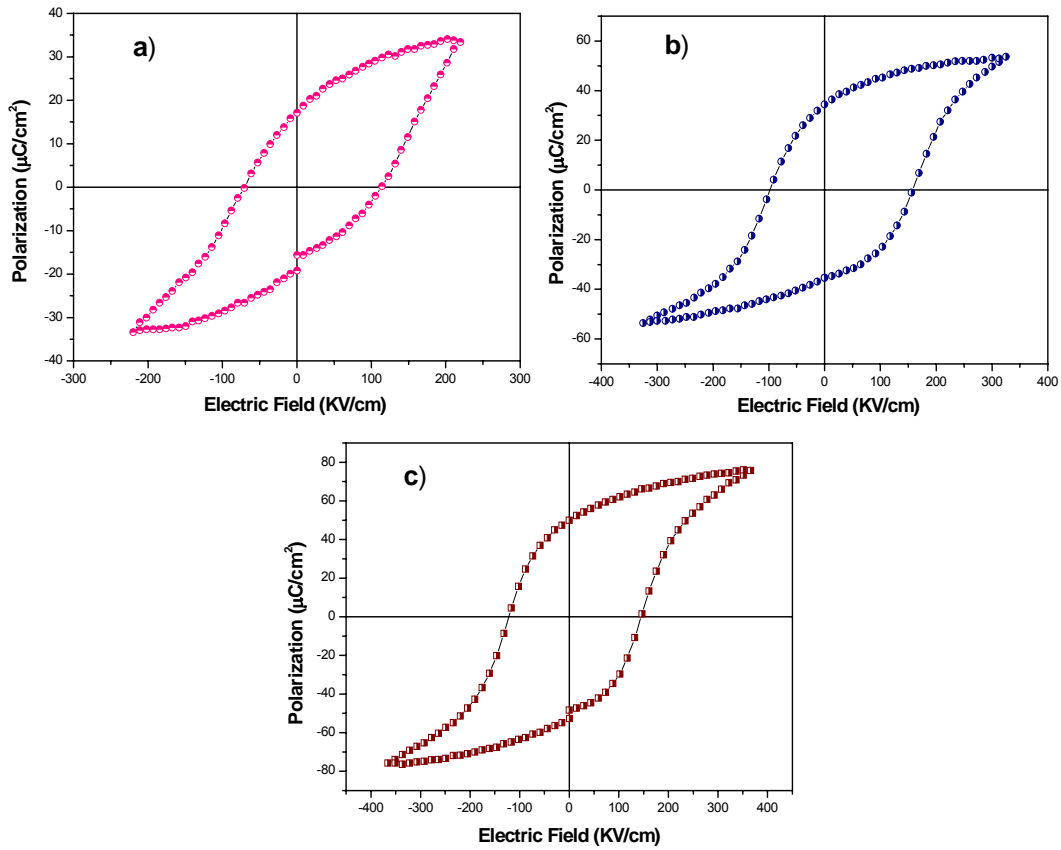


Figure 31. P-E hysteresis curves of  $\text{Bi}_{(4-x)}\text{Er}_x\text{Ti}_3\text{O}_{12}$  thin films as a functions of Er composition  $x$ .



**Figure 32. x dependence of P-E hysteresis loops for  $\text{Bi}_{(4-x)}\text{Pr}_x\text{Ti}_3\text{O}_{12}$  thin films deposited on Pt(Pt/TiO<sub>2</sub>/SiO<sub>2</sub>/Si) substrates annealed at 750°C in air. a) x=0.35, b) x=0.45, c) x=0.55 and d) x=0.6.**

$\text{Bi}_{(4-x)}\text{Pr}_x\text{Ti}_3\text{O}_{12}$  thin films annealed at 750°C in air exhibited remnant polarization values of high as  $50.3 \mu\text{C}/\text{cm}^2$ , as shown in figure 32. The exceptional large  $P_R$  value was coupled with coercive field of 145.10 KV/cm for the composition  $x= 0.55$  (fig.32c.). This coercive field value is greater that the one reported by Hirofumi et al [36]. On the other hand the value of remnant polarization and coercive field for the others compositions are  $17.17 \mu\text{C}/\text{cm}^2$  and 114.05 KV/cm for  $x=0.35$  (fig. 32a.),  $34.76 \mu\text{C}/\text{cm}^2$  and 155.08 KV/cm for  $x=0.45$  (fig.32b.) respectively in a field of 367 KV/cm.

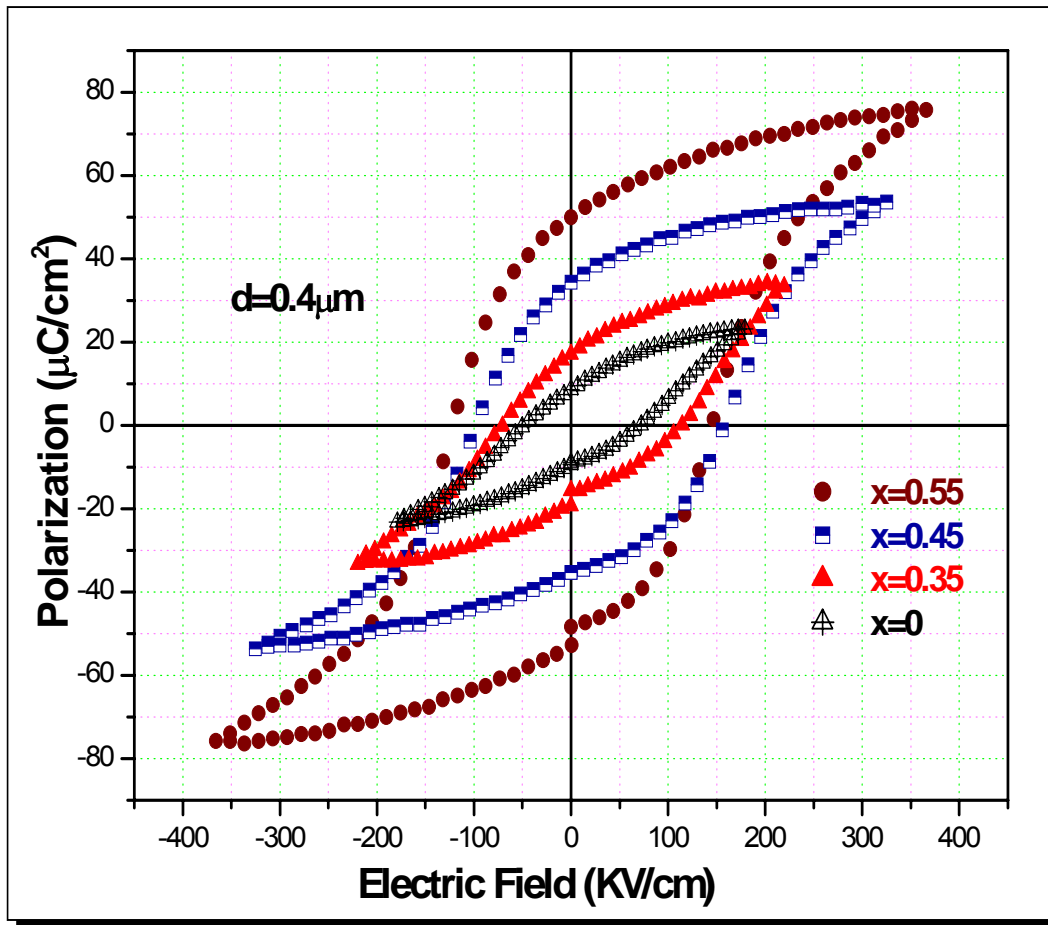


Figure 33. P-E hysteresis curves of  $\text{Bi}_{(4-x)}\text{Pr}_x\text{Ti}_3\text{O}_{12}$  thin films deposited on  $\text{Pt}(\text{Pt}/\text{TiO}_2/\text{SiO}_2/\text{Si})$  substrates as a functions of Pr contents  $x$ .

The ferroelectric response illustrated in the fig 32c, is attributed to the maximum tilt of  $\text{TiO}_6$  octahedra towards  $\text{Bi}_2\text{O}_2$  interlayer, a factor that should have enhanced by the presence of Pr ions. The substitution of rare earth (Ce,Er,Pr) for Bi in bismuth titanate, in this case the  $\text{Pr}^{3+}$  should have partly reduced the oxidation state of Ti to trivalent, producing Ti ions with  $3d^1$  electronic configuration.

This effect would have promoted Jahn-Teller distortion; a  $d^1$  electron in an octahedral field occupies the  $d_{xy}$  orbital of the split  $t_{2g}$  and thus leads to the “Z-in” distortion [41]. The P-E hysteresis loops as a function of composition  $x$  can be seen in the figure 33.

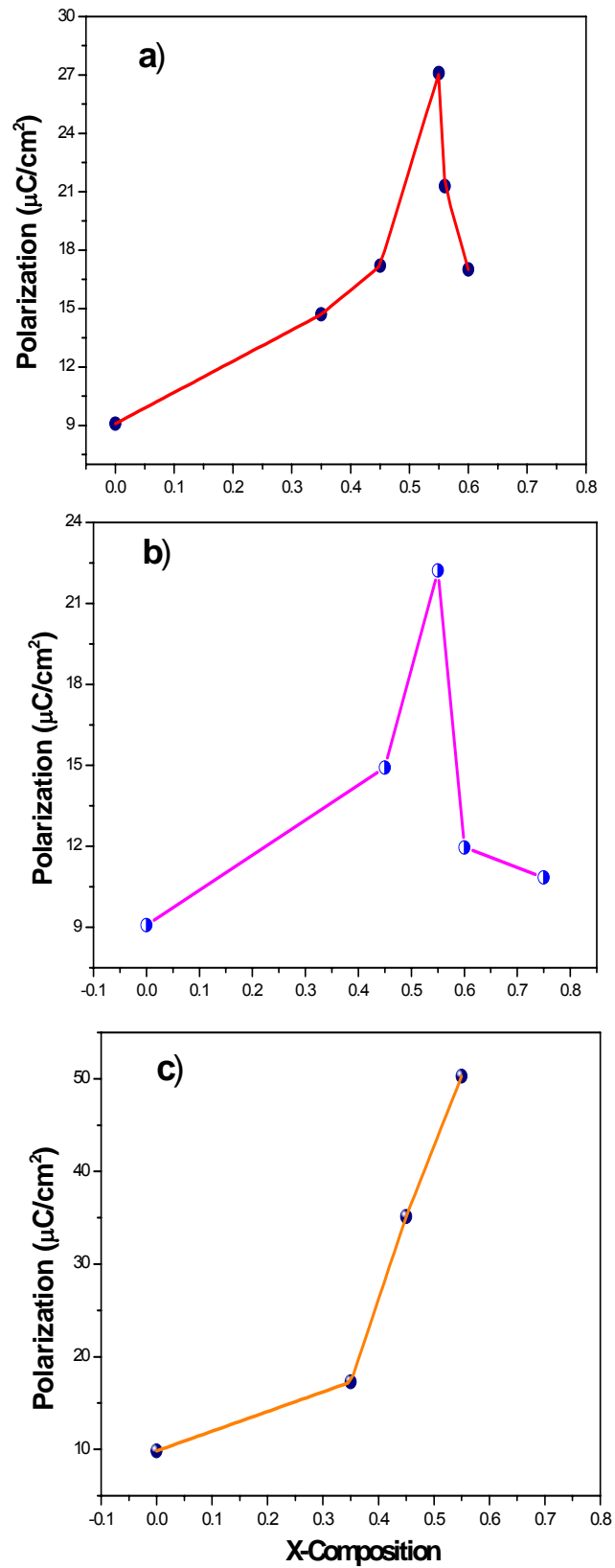


Figure 34. Remnant polarization ( $P_R$ ) as a function of contents of x in  $\text{Bi}_{(4-x)}\Pi_x\text{Ti}_3\text{O}_{12}$  thin films. a)  $\Pi = \text{Ce}$ , b)  $\Pi = \text{Er}$ , c)  $\Pi = \text{Pr}$ .

The relation between the remnant polarization and concentration of doped rare earths (Ce,Er,Pr)-modified bismuth titanate is shown in the figure 34. Evidently the best ferroelectric response was achieved when Pr ions were selected as dopants.

#### **4.4 Dielectric Properties**

The ferroelectric materials are in general characterized by higher dielectric constants approximately (200-10000). For ordinary insulating substances it is around (5-100). The higher dielectric constants make these materials useful as capacitor and energy-storage devices materials. Another very important characteristic is the relative low dielectric loss (loss  $\tan \delta$ ). These properties are measured with capacitors fabricated with the ferroelectric materials as a function of applied frequency. Capacitor Pt-ferroelectric-Pt (PFP) were fabricated depositing Pt top electrodes by dc sputtering technique on the surface of the thin film with an area of  $3.14 \times 10^{-4} \text{ cm}^2$  using a shadow mask, where the area of the electrodes is defined for the geometry of the mask used. A vertical capacitive structure of  $\text{Pt}/\text{Bi}_{(4-x)}\text{Ti}_x\text{O}_{12}/\text{Pt}/\text{TiO}_2/\text{SiO}_2/\text{Si}$  is represented in figure 35. The Pt top electrode is connected to terminal A, while other electrode is Pt sub layer is connected to the terminal B. A swept harmonic signal of variable frequency is applied and therefore the value of capacitance can be measurement. A vertical capacitive structure can be approximated by a single parallel-plate capacitor of area A with distance between its electrodes d. Such capacitor has a capacitance C expressed by:

$$C = \frac{\epsilon_0 \epsilon A}{d} \quad (10)$$

Hence the dielectric permittivity of the material that is used as dielectric layer in the capacitor with well-known geometry can be extracted from the direct measurement of the capacitance. From equation (10), the dielectric permittivity can be determined from:

$$\epsilon = \frac{Cd}{\epsilon_0 A} \quad (11)$$

Where  $\varepsilon$  is the dielectric permittivity,  $C$  is the capacitance measured,  $d$  is the thicknesses of the film,  $\varepsilon_0$  is the permittivity of vacuum with value of  $(8.8542 \times 10^{-12} \text{ C}^2/\text{Nm}^2)$ , and finally  $A$  is the area of top electrode that in this case is  $3 \times 10^{-4} \text{ cm}^2$ . Moreover any material which exhibits dielectric properties can be used as a dielectric in these measurement processes and therefore can be used to evaluate the utilized method.

A capacitor is never perfect therefore they are always losses and the dielectric permittivity of all dielectrics is assumed to be a complex value consisting of two components:

$$\varepsilon = \varepsilon' + i\varepsilon'' \quad (12)$$

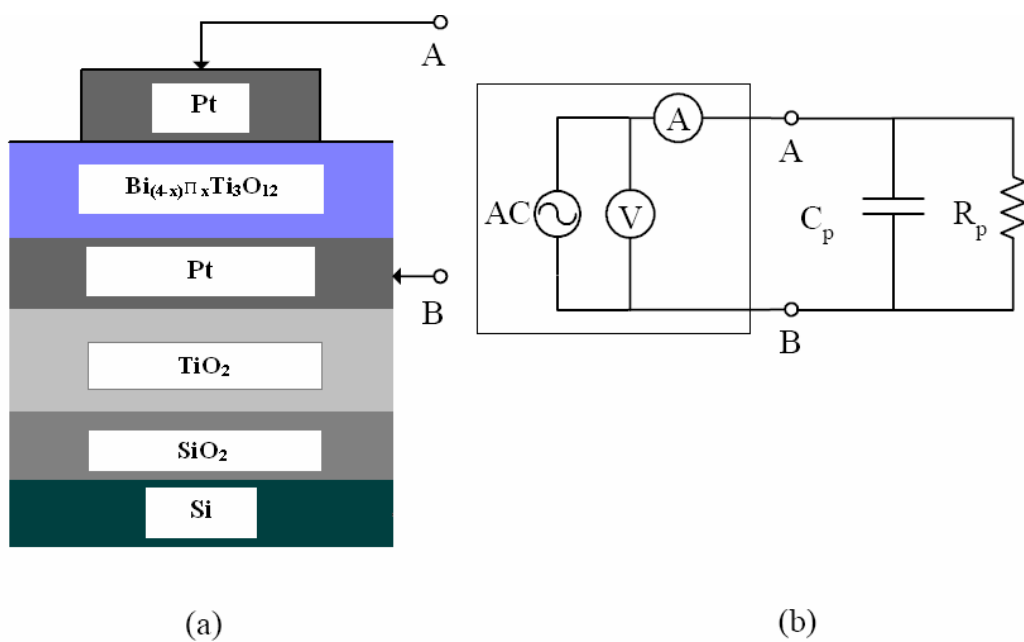


**Figure 35. a) Vertical schematic of capacitive structure Pt/Bi<sub>(4-x)</sub>Π<sub>x</sub>Ti<sub>3</sub>O<sub>12</sub>/Pt/TiO<sub>2</sub>/SiO<sub>2</sub>/Si (Π = Ce,Er,Pr), b) equivalent electric circuit of a)**

Where  $\varepsilon'$  represent the real portion of  $\varepsilon$  and  $\varepsilon''$  is the imaginary portion. The ratio of the power loss in a dielectric material to the total power transmitted through a dielectric is known as dissipation factor, loss dielectric or loss tangent, therefore we have that:

$$\text{Tag } \delta = \frac{\varepsilon''}{\varepsilon'} \quad (13)$$

These measurements were done in terms of the dielectric permittivity and dielectric loss ( $\tan \delta$ ) Vs frequency of the applied voltage using an impedance analyzer HP4294a in the range from 1 KHz to 1MHz and -10V to 10V respectively.

The relation between the dielectric constant and dielectric loss as a function of applied frequency of BCeT films with different contents of Ce is shown in figure 36a. The dielectric constant gradually decreases with a rising frequency for all films.

In the Ce-substitution films, the dielectric constant is diminished with respect to the film without doping. The dielectric constant for the compositions  $x=0, 0.35, 0.45, 0.55, 0.56, 0.6$  and an applied frequency of 1 KHz were 559, 262, 431, 394, 437, 360 respectively. Although the greater value for the dielectric loss was 13% also for the composition  $x=0$ , the others values were around of 8.5%.

The dependence between dielectric constant and dielectric loss Vs applied voltages is summarized by figure 36b (for  $x= 0.55$ ). The asymmetry of the curves, it is the reflection of the small mismatch at the end of the hysteresis loop (Fig.28c).

For the case of films doped with Er dielectric response as a function of frequency was not as high as for base BIT. The dielectric constant values for different contents of Er ( $x=0, 0.45, 0.55, 0.6, 0.75$ ) and an applied frequency of 1KHz were 559, 442.6, 383, 333.90 and 247.93 respectively.

The behavior of the dielectric constant as a function of frequency is consistent with that the similar layer-perovskite systems based on Ba and Sr [47].

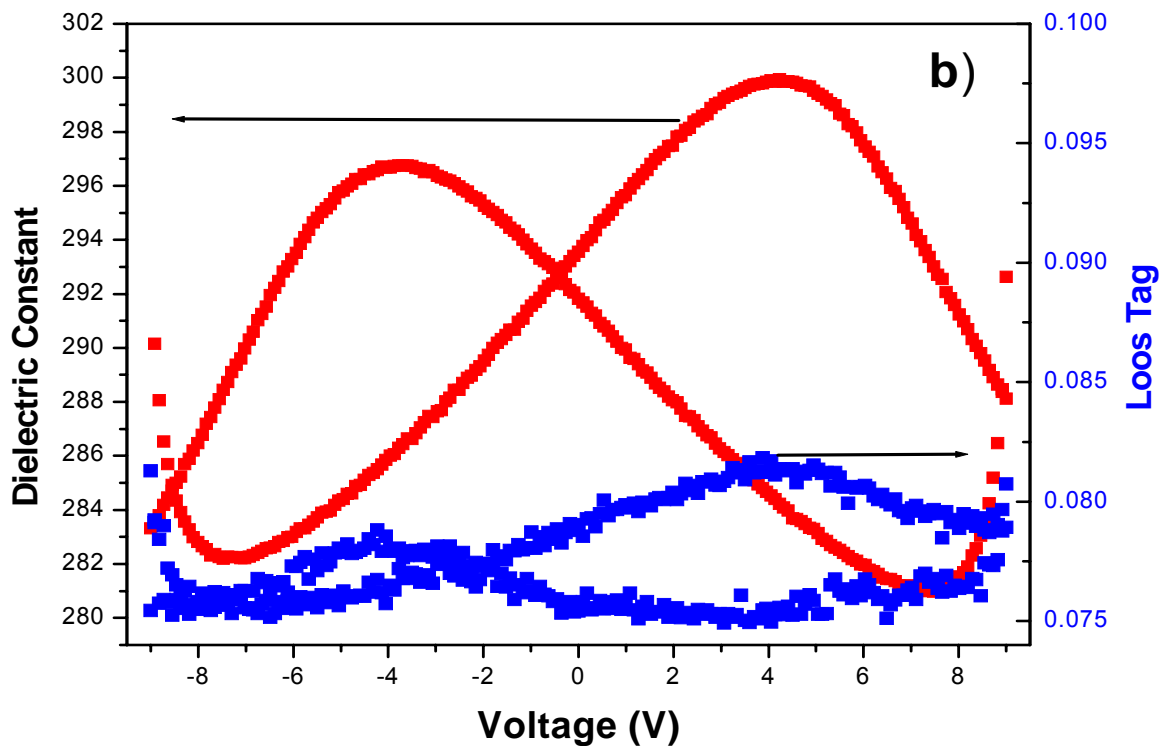
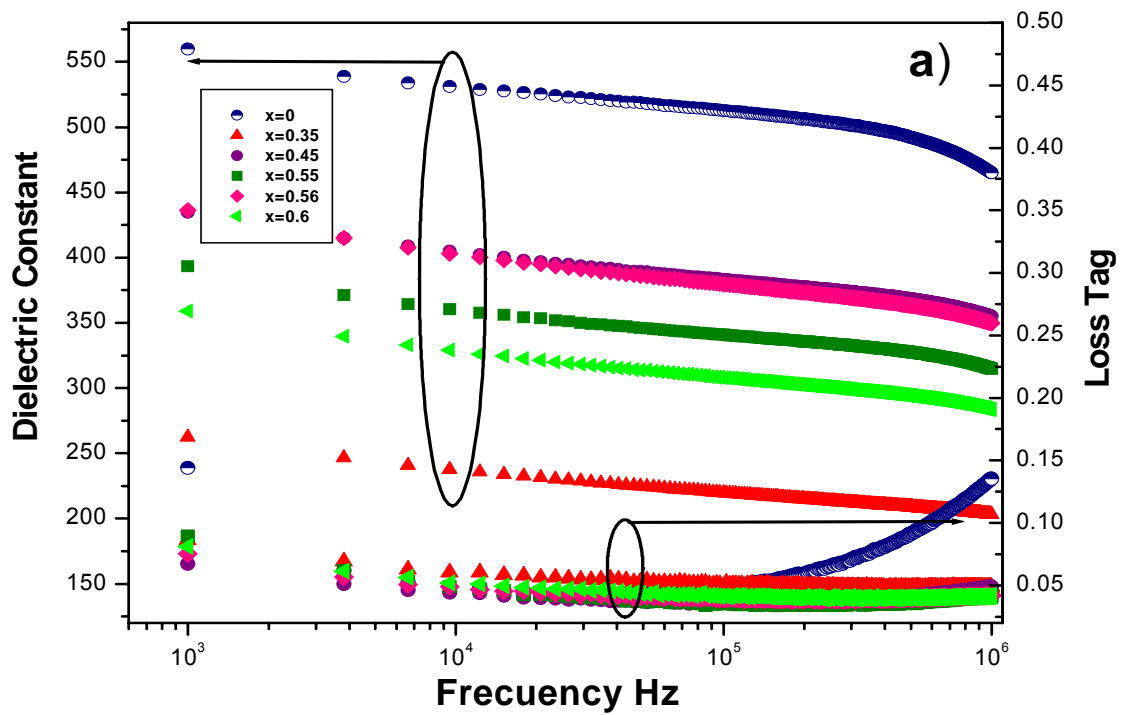


Figure 36. Dielectric constant and dissipation factor (loss Tag) of  $\text{Bi}_{(4-x)}\text{Ce}_x\text{Ti}_3\text{O}_{12}$  thin films as a function of a) frequency for the compositions  $x=0.35, 0.45, 0.55, 0.56,$  and  $0.6$ . b) Voltage for  $x=0.55$ .

The drop in the dielectric constant values with the applied frequency increases from 1 KHz to 1MHz as showed in figure 37a. The dissipation factor was found to be around of 6% and 20% for all films. The curves of dielectric constant Vs applied voltage from (-10V to 10V) are given in figure 37 b. In this case the asymmetry of the curves can be attributed to the poor saturation exhibited by the hysteresis loop (Fig. 30b), although the curves exhibit the typical ferroelectric behavior, which resembles the shape of a butterfly.

The best ferroelectric response was achieved when base material BIT was doped with Pr. This is confirmed for the information provided by the hysteresis loop of figure 33 and the graphs of fig. 38a, where the dielectric constant increases up to  $x= 0.55$  compared with that of  $\text{Bi}_4\text{Ti}_3\text{O}_{12}$ . Although the dielectric constant value decreased for  $x=0.45$ , it is still higher than the corresponding value for substituted La, Sm and Nd BIT films reported by takashi et al [19]. They reported dielectric loss values between 10% and 20% that is relatively small. From figure 38 it is observed that the dielectric constant was smaller when the base BIT is doped with Ce and Er. Figure 38b, shows the dielectric constant as a function of the voltage exhibiting the typical butterfly-shape. In this case the dielectric constant under zero bias is 465.33 which are larger than the values for bulk  $\text{Bi}_4\text{Ti}_3\text{O}_{12}$  (BIT), BLaT and BNdT reported by Hiroshi et al [43].

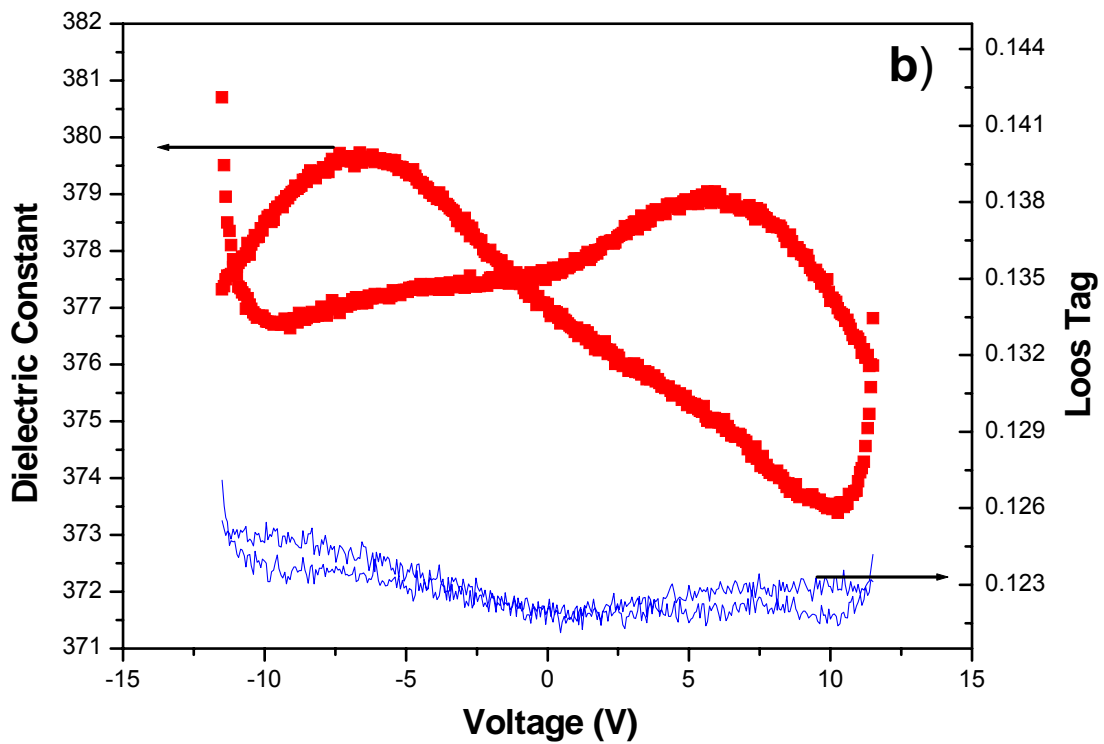
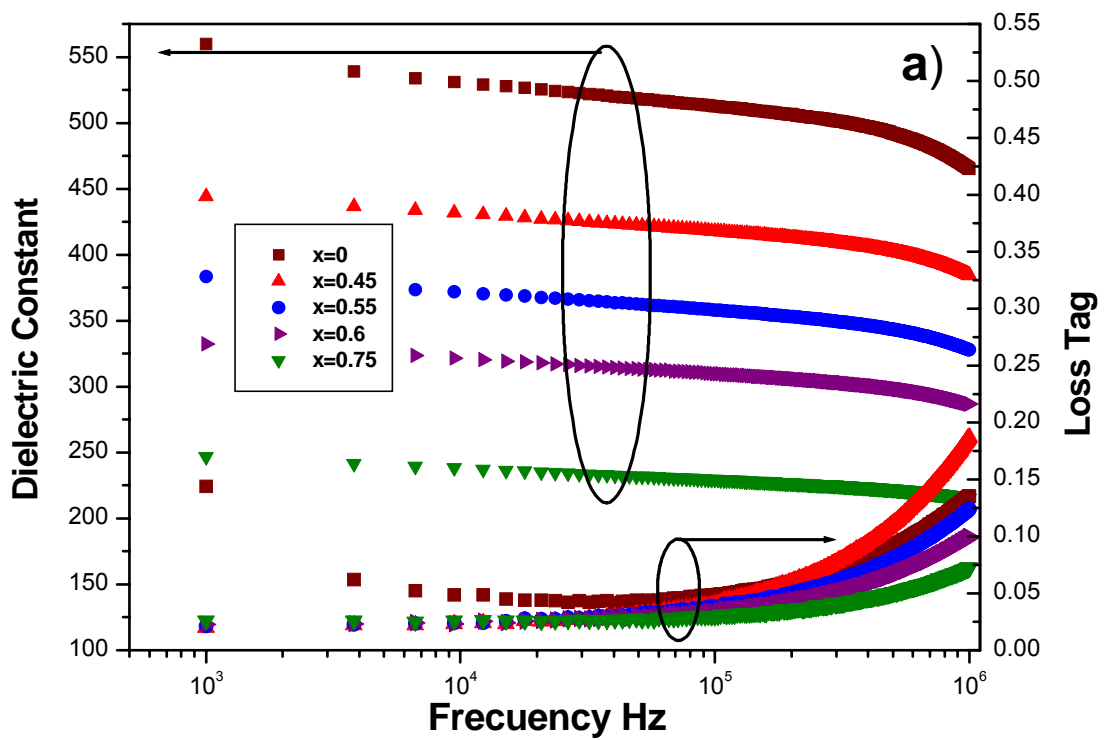


Figure 37. Variation of dielectric constants and dielectric loss as a function of a) Frequency for BErT films with different contents of Er. b) Voltage for BErT film for the composition  $x=0.55$ .

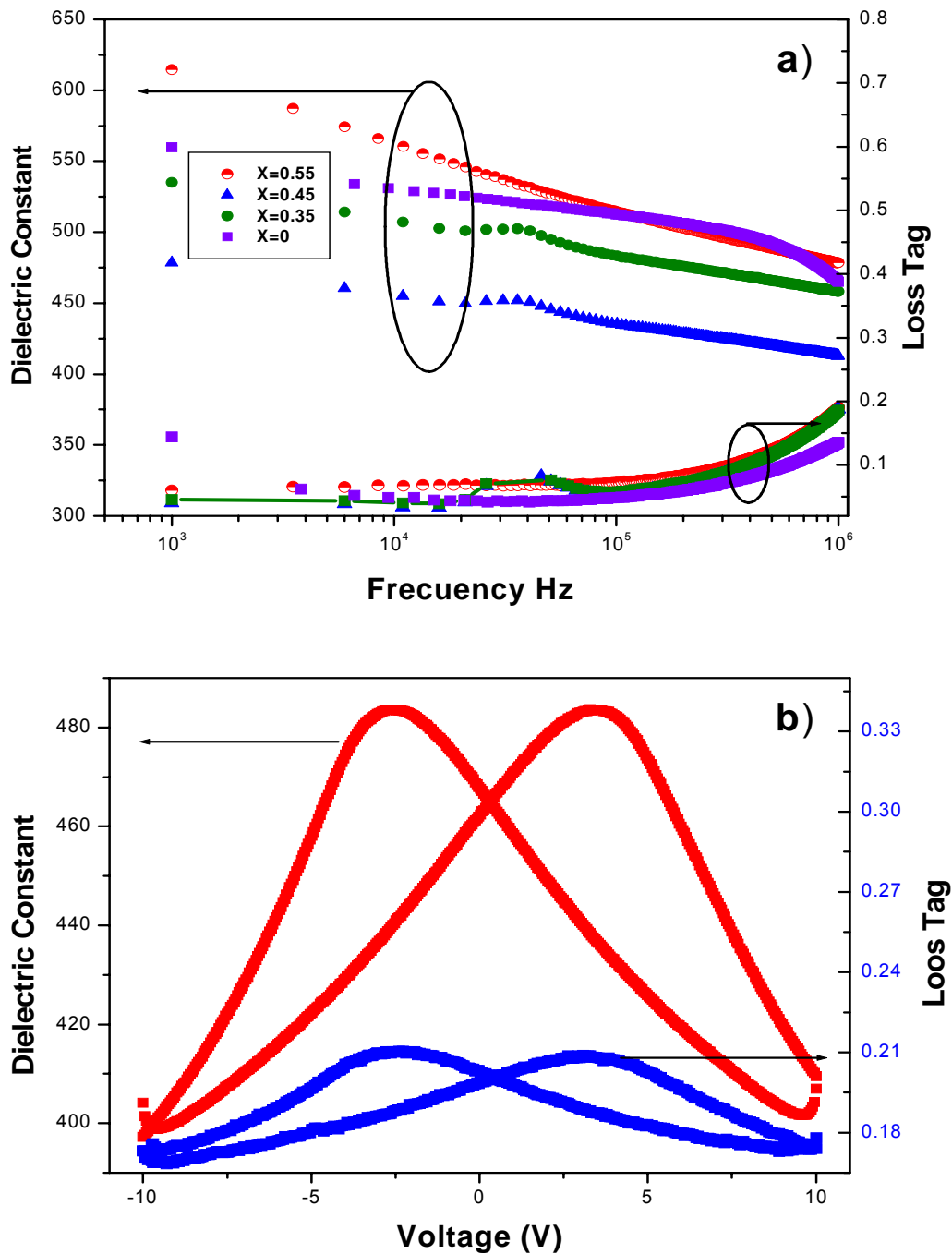


Figure 38. a) The response dielectric dependency of applied frequency for BPrTiO thin films for different contents of Pr. b) dielectric constant and dielectric loss as a function of the voltage for Bi<sub>3.45</sub>Pr<sub>0.55</sub>Ti<sub>3</sub>O<sub>12</sub> thin film on Pt/TiO<sub>2</sub>/SiO<sub>2</sub>/Si substrate.

#### 4.5 Leakage Current

No dielectric material is a perfect insulator, and no matter how high the insulation resistance is, some small current will always flow through the material

when high voltage is applied across the top electrodes of the capacitor. This leakage current multiplied by applied voltage represents a distinct power loss.

The value of leakage current is usually one of the most critical factors for FeRAM application of ferroelectric thin films, due to its direct relation to power consumption and function failure of devices. The leakage depends on various factors related to materials and their processing routes. Some those factors are oxygen depletion at the surface, ionic migration within the bulk, surface traps, and trapped charges, roughness of the surface and interfaces and inhomogeneous stoichiometry. Therefore the complex analysis is a difficult task due to the complicated nature of the charge transport process. The method I-V is based of the measurement of the leakage current as a function of applied electric field through a capacitive ferroelectric cell by an electrometer. In this research, the leakage current vs. electric field curves were obtained by using a 6517A electrometer/ high resistance meter at room temperature, applying voltages with a step of 0.2 V and delay time of 10 seconds.

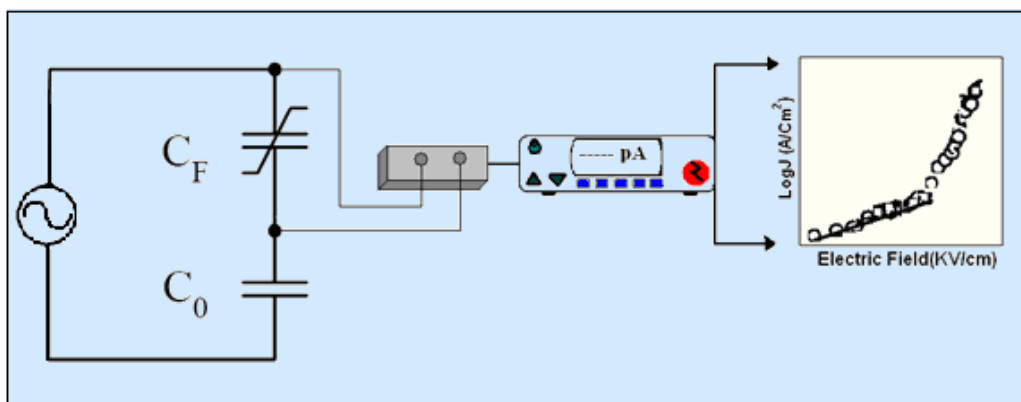


**Figure 39. Schematic diagram for measurement of the leakage current.**

The typical capacitive ferroelectric cell is shown in the Fig.39. Figure 40 shows the leakage current densities of BCeT thin films annealed at 750°C as a function of applied electric field, for several concentration of Ce. The value of leakage current of BIT thin film was large around of  $10^{-4}$  A/cm<sup>2</sup> for a field applied of 50 KV/cm, but decreased in the order of  $10^{-6}$  A/cm<sup>2</sup> for the same value of applied electric field when the bare material BIT is doped with Ce<sup>3+</sup> for the composition x=0.55. This value was similar to that previously reported [16].

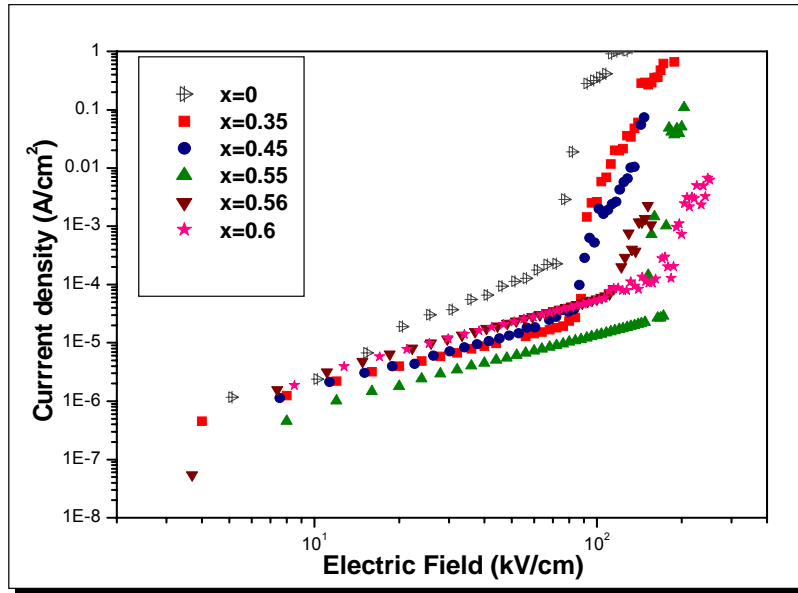


Figure 40. The leakage current density as a function of applied electric field, for the  $\text{Bi}_{(4-x)}\text{Ce}_x\text{Ti}_3\text{O}_{12}$  thin films for  $x = 0, 0.35, 0.45, 0.55, 0.56, 0.6$  deposited on Pt(Pt/TiO<sub>2</sub>/SiO<sub>2</sub>/Si) substrates.

The effect of Er on leakage current behavior in BErT thin films for the concentrations of  $x = 0.45, 0.55, 0.6, 0.75$  can be seen in the figure 41. The leakage current values obtained were smaller than in the case of doped with Ce (Fig 40). In a applied electric field 115 -150 KV/cm the increase was abrupt from  $10^{-6}$  A/cm<sup>2</sup> to  $10^{-3}$  A/cm<sup>2</sup>. The best behavior of leakage current is presented for the thin film with the content of Er is  $x = 0.45$ .

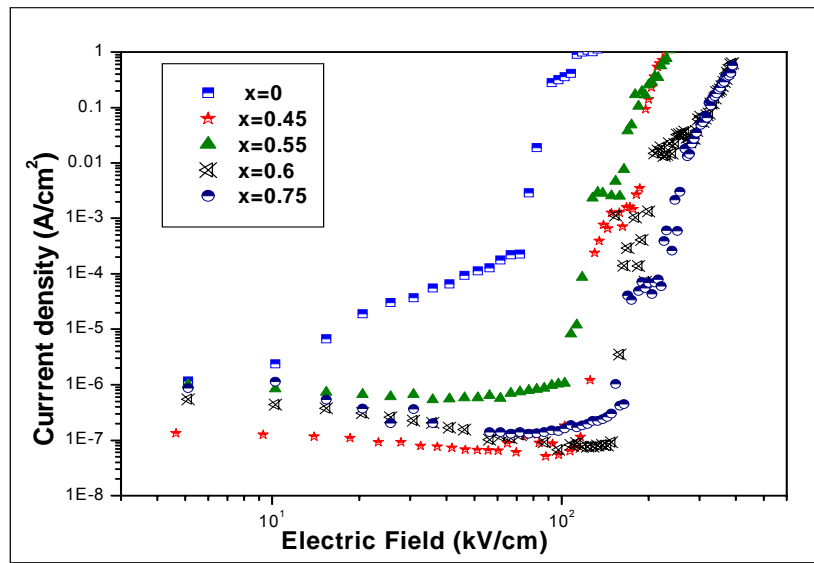
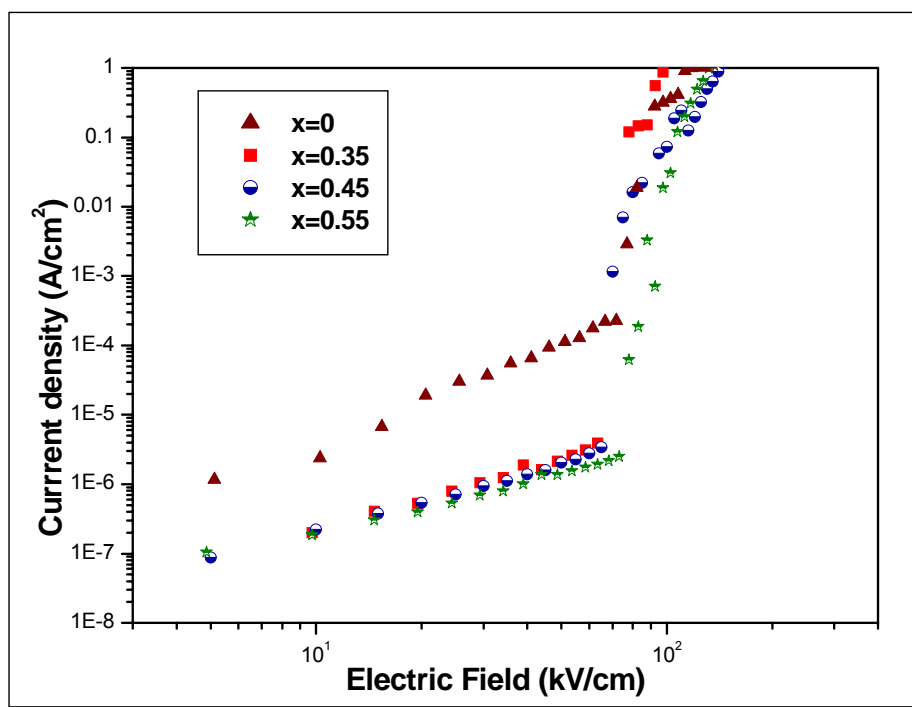


Figure 41. The leakage current Vs Applied electric field at room temperature for the  $\text{Bi}_{(4-x)}\text{Er}_x\text{Ti}_3\text{O}_{12}$  thin films for  $x = 0, 0.45, 0.55, 0.6, 0.75$  deposited on Pt(Pt/TiO<sub>2</sub>/SiO<sub>2</sub>/Si) substrates annealed at 750°C.



**Figure 42. Leakage current density for  $\text{Bi}_{(4-x)}\text{Pr}_x\text{Ti}_3\text{O}_{12}$  thin films  $\text{Pt}(\text{Pt}/\text{TiO}_2/\text{SiO}_2/\text{Si})$  substrates as a function of the electric field.**

Figure 42. shows the leakage current density as a function of the applied electric field for BPrT films. The leakage current density of BPrT thin films for the different contents of Pr ( $x=0.35, 0.45, 0.55$ ) was about  $10^{-7} \text{ A/cm}^2$  and  $10^{-6} \text{ A/cm}^2$  at an electrical 30KV/cm and 70KV/cm respectively. The leakage current jumps abruptly to  $10^{-3} \text{ A/cm}^2$  at an applied up 70 KV/cm, indicating a dielectric breakdown. This can be attributed to defects such as oxygen vacancies interacting strongly with domain boundaries, which should have significant influences on the conduction process. Also the fact that the electric field increases as the leakage current increases, can be attributed to the assembly of mobile vacancies, such as Bi and O vacancies, can assemble in extended structures near the domain boundaries and may contribute to an increase of the leakage current.

## 5. RESULTS ANALYSIS

### 5.1 Changes in the Lattice Parameters.

Summarizing our results, we have the average lattice parameters ( $a$ - $b$ - $c$ ) that were estimated in the section 4.1, where the small variation of those, for the three systems under study (BCeT, BErT, BPrT) for  $x=0, 0.45, 0.55$  can be seen in table 9.

**Table 9. Lattice parameter for bare and RE-doped Bismuth Titanate (BIT)**

Parameter (A)	BIT	X=0.45			X=0.55		
		Dopant Agent			Dopant Agent		
		Ce	Er	Pr	Ce	Er	Pr
$a$	5.41-5.43	5.38	5.38	5.40	5.38	5.405	5.435
$b$	5.36-5.44	5.37	5.36	5.37	5.39	5.315	5.30
$c$	32.60-32.84	33.1	32.66	32.705	33.04	32.63	32.38

Of this result we can indicate that the lattice parameter " $a$ " in BErT and BCeT reduces slightly with the dopant species. (Although this could be attributed to systematic errors, with the measuring instrument or procedure). For the system BPrT, this parameter does not change.

In the case of the  $b$  lattice parameter, for BErT and BPrT it diminishes slightly as a function of the composition  $x$ . For the BCeT system,  $b$  remains constant.

Finally the lattice parameter  $c$  in BCeT increases when the dopant species are incorporated into the host structure but there is no obvious dependence on the composition  $x$ . This parameter does not increase for the BErT and the BPrT systems. We can infer from the collected data that there is a change (although very small) in some lattice parameters for the doped systems in comparison with the BIT-

host material, but the changes are small, not systematic, and therefore rather inconclusive.

Using the values obtained for lattice parameters at  $x=0.55$ , we estimate the dipole moments and the ion displacements. To estimate these values we begin calculating the volume of the unit cell

$$\mathcal{G} = a \times b \times c \quad (14)$$

The area of the thin films is  $3.14 \times 10^{-4} \text{ cm}^2$  and the average thickness is  $0.4 \text{ }\mu\text{m}$ , therefore the volume  $V$  of the sample is:

$$V = 1.256 \times 10^{-14} \text{ m}^3$$

The ratio  $\frac{V}{\mathcal{G}} = N'$  is the number of the unit cells in the sample. Since there are  $m=42$  electric dipoles per unit cell, the total number of dipoles in the sample is:  $mN'$ . Using the measured values of the remnant polarization “P”,  $p$  can be obtained from the number of moments per unit volume  $N = \frac{mN'}{V}$  i.e,  $p = \frac{P}{N}$ . Considering the net charge of the ions,  $q$ , we calculate the average ion displacement in the unit cell. These results can be seen in table 10. Pr shows the largest average displacements and Er the lowest, in the same proportion as the dipole moments.

**Table 10. Dipoles moments and ions displacements for REdoped-BIT “ $x=0.55$ ”**

System	$\mathcal{G} \text{ (m}^3\text{)}$	$N'$	$mN'$	$p \text{ (C.m)}$	$d \text{ (Å)}$
BCeT	$958 \times 10^{-30}$	$1.31 \times 10^{13}$	$5.502 \times 10^{14}$	$6.27 \times 10^{-30}$	0.160
BErT	$937 \times 10^{-30}$	$1.34 \times 10^{13}$	$5.628 \times 10^{14}$	$5.08 \times 10^{-30}$	0.106
BPrT	$930 \times 10^{-30}$	$1.35 \times 10^{13}$	$5.67 \times 10^{14}$	$1.11 \times 10^{-29}$	0.231

We must consider why these displacements occur. The clue to this question is the fact that for perovskite structures ( $ABX_3$ ) with X often occupied by oxygen, the phase transitions from the paraelectric to the ferroelectric phase implies a structural transition from the cubic to tetragonal which occurs at the same time as the displacement. The cubic form is highly symmetric and when the transition occurs the final structure has reduced symmetry.

## 5.2 Ferroelectric Properties

The values of various ferroelectric properties of RE (Ce,Er,Pr)- doped BIT appear in table 11.

**Table11. Electric response for the bare and RE-doped BIT.**

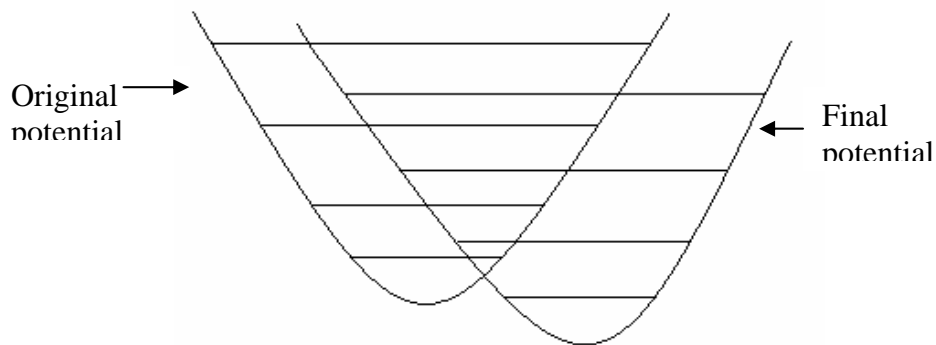
X=0 (BIT)		X=0.45			X=0.55		
	measured	Ce	Er	Pr	Ce	Er	Pr
Remnant Polarization $\mu C / cm^2$	9	17.2	15.1	34.7	27.5	22.8	50.3
Dielectric Constant. F= $10^3$ Hz	559	431	383	478	394	333	614
Loss tang % F= $10^3$ Hz	14	6.5	2.2	4	9	1.8	6
Leakage current E<70 Kv/cm	$2.4 \cdot 10^{-4}$	$2.63 \cdot 10^{-5}$	$6.1 \cdot 10^{-8}$	$3.3 \cdot 10^{-6}$	$8.1 \cdot 10^{-6}$	$7 \cdot 10^{-7}$	$2.1 \cdot 10^{-6}$

We can see that the remnant polarization increases and the value of the dielectric constant decreases as function of the dopant fraction except for Pr: 0.55, where we see an increase in the value of the dielectric constant. The discrepancy for the case of Pr might be attributed to measurement errors and should be verified in the future. The leakage current and dielectric losses don't have a clear tendency.

We cannot attribute these results to the changes in the lattice parameters, because these are inconclusive, we believe that the difference in the electronic

configuration between the dopant elements and Bi may be responsible for the changes in the ferroelectric properties.

The ferroelectric phase transition occurs as the system reaches a new ground state that is lower in energy than the previous one, then along the line of the distortion the degeneracy of states is removed and the states density increases.



The arrival to a new ground state brings the system to a lower energy state and therefore the ions move to comply with the new situation that is, the ions move in order to minimize the energy of the system. This type of the distortion in the structure is attributed to the Jahn-Teller effect (any non-linear molecular system in a degenerate electronic state will be unstable and will undergo distortion to form a system of lower symmetry and lower energy thereby removing the degeneracy) [44]. The systems that we are studying are members of the family of perovskites and the Jahn-Teller effect should may occur for all of them. The difference in the electronic configuration between the dopant elements ( $\text{Pr}^{3+}:4f^25s^25p^6$ ,  $\text{Ce}^{3+}:4f^15s^25p^6$ ,  $\text{Er}^{3+}:4f^{11}5s^25p^6$ ) and Bi [45] may lead to a more stable ground state that enhances the ferroelectric properties. Uong et al [41] indicates that the substitution of lanthanides (Nd, Gd, Sm, Pr) for bismuth in  $\text{B}_4\text{Ti}_3\text{O}_{12}$  partly reduces the oxidation state of Ti to trivalent, producing Ti ions with  $3d^1$  electronic configuration that inevitably leads to the Jahn-Teller distortion. The Jahn-Teller theorem further suggest that  $d^1$  electron in an octahedral field occupies the  $d_{xy}$  orbital of the split  $t_{2g}$  and thus leads to the distortion. The exact nature and role of the dopant electronic configuration in the changes in remnant polarization and the dielectric constant will be the subject of further investigation.

### 5.3 Spontaneous Polarization

The relation between the spontaneous polarization and the dielectric constant is derived from the fact that in the ferroelectric phase  $T < T_c$  ( where  $T_c$  is the Curie temperature) there must be a non-zero induction even when the field  $E$  is zero [46]:

$$D_0 = \pm \sqrt{\frac{\alpha(T_c - T)}{B}} \quad (16)$$

Where  $\alpha$  and  $B$  are constants of the material. Thus the spontaneous polarization is give by ratio of  $D_0/4\pi$  this is:

$$p_0 \pm \frac{\sqrt{\alpha(T_c - T)}}{4\pi\sqrt{B}} \quad (17)$$

The dielectric constant of the ferroelectric phase may be defined as the derivate  $dD/dE$  for  $E=0$ , which is given by

$$\frac{dD}{dE} = \frac{1}{2\alpha(T_c - T)} \quad (18)$$

Combining equations (17) and (18) we get a the relation between dielectric constant and remnant polarization is give by:

$$\varepsilon = \xi \frac{1}{P_0^2} \quad (19)$$

Where the  $\xi = \frac{1}{32\pi^2 B}$ . This relation is in accord with our results since the remnant polarization increases as the dielectric constant decreases (see table 11).

### 5.4 Leakage Current

The leakage current may be attributed to the oxygen vacancies produced during the solidification as results of local disturbances [45] during the growth of the crystal. Oxygen vacancies may also be created by atomic rearrangements during rapid cooling from higher temperatures. The imperfections produced by the vacancies of atoms or ions are known as *Schottky imperfections*. The conductivity

mechanism in our materials is attributed to the ion movement at not of electrons. The net flow of atoms or ions in this type of system can be represented by the equation:

$$J_N = -D \frac{dC}{dX} \quad (20)$$

Where  $J_N$  is the number of atoms that cross the unit of area in the time unit,  $D$  is the proportionality constant called the diffusivity (atomic conductivity), and finally  $\frac{dC}{dX}$  is concentration gradient. The incorporation of the dopants (Ce,Er,Pr) into the host-BIT, may produce a reduction in vacancies and therefore diminish the flow of the ions in the crystal. This may be the mechanism for the leakage current reduction observed in some samples. However, our experimental results are rather inconclusive and further work is required to understand the effects of doping.

## CHAPTER 6

### CONCLUSIONS AND FUTURE WORKS

Bismuth titanate  $\text{Bi}_4\text{Ti}_3\text{O}_{12}$ , is a ferroelectric material that belongs to the family of Aurivillius phases or layered perovskite-like structure is a potential candidate material for devices such as nonvolatile memories, optical piezoelectric memories and electro-optic devices due to its relatively low coercive field, high dielectric constant, low leakage current and free fatigue. The fabrication of  $\text{Bi}_4\text{Ti}_3\text{O}_{12}$  thin films have been reported using some techniques such as Pulsed Laser Deposition [21], Sputtering [26-27], Chemical vapor deposition [29], and Sol-Gel process [34-36].

In this thesis we report the successful fabrication of  $\text{Bi}_4\text{Ti}_3\text{O}_{12}$  thin films doped with rare earths (Cerium, Erbium and Praseodymium) for different compositions deposited on Pt ( $\text{Pt}/\text{TiO}_2/\text{SiO}_2/\text{Si}$ ) substrates annealed at  $750^\circ\text{C}$  temperature using the Sol-Gel Process. The X-ray diffraction (XRD) patterns revealed polycrystalline thin films, exhibited a well-crystallized layered-perovskite (Aurivillius-type) which preferred orientation in the  $(00\ell)$  planes, besides of the strong  $(117)$  diffraction peak.

The absence of the any impurity phase in the x-ray diffraction pattern suggests the incorporation of the dopant species ( $\text{Ce}^{3+}\text{-Er}^{3+}\text{-Pr}^{3+}$ ) without affecting the BIT-host structure. The average crystal size was estimate to be between 20nm and 40 nm by FWHM approach using the Debye-Scherrer's equation [40] for the  $(117)$  peak. The lattice parameters were determined from the orthorhombic symmetry where the distortion  $b/a$  was 1.013, 0.990, and 0.977 for Ce, Er, and Pr respectively for a dopant molar fraction of  $x = 0.55$

The surface morphology of the thin films was examined with the Atomic Force Microscopy (AFM) in the contact mode with a scan area of  $1 \mu\text{m}^2$ . The AFM images showed films smooth without cracks with fairly uniform grains with average size around 150nm, that consist of nanosize individuals, which agrees with the information provided by the XRD analyses. The average roughness root-mean-square "RMS" of the films varies between 4 nm and 13 nm depending of the type and fraction molar of the dopant (film thickness around 400 nm).

Electrical properties measurement was conducted on BIT thin films in Pt- BIT-Pt configuration at room temperature. The ferroelectric hysteresis loop was improved with the substitution at Bi site of Ce, Er, and Pr, the values obtained of polarization and coercive field as a function of applied electric field for the bare material BIT was  $8.93 \mu\text{C}/\text{cm}^2$  and 75 KV/cm. For a fraction of dopant "x" of 0.55, the values of polarization and coercive field were  $25.7 \mu\text{C}/\text{cm}^2$  and 210 KV/cm,  $22.82 \mu\text{C}/\text{cm}^2$  and 195.73 KV/cm,  $50.30 \mu\text{C}/\text{cm}^2$  and 145.10 KV/cm for Ce, Er, and Pr dopants, respectively. The large  $P_R$  value of the Pr-substituted BIT film is comparable to the commercially used  $\text{Pb}(\text{Zr},\text{Ti})\text{O}_3$  films and is a promising candidate for lead-free ferroelectric applications.

The dielectric properties were measurement in terms dielectric constant and loss factor  $\tan \delta$  as a function of the frequency and the voltage. The curves obtained revealed the decrease of the value of the dielectric constant with the increase of the frequency. For an applied frequency of 1KHz and a composition of  $x=0.55$  the value of dielectric constant was 559 for BIT, 394 for BCeT, 383 for BErT, and 615 for BPrT, with a loss dielectric between 6% and 20%. The dielectric constant-voltage curves resembled the shape of a butterfly, which evidenced a typical ferroelectric behavior.

The BIT thin films prepared from stoichiometric composition is well known to suffer from a high leakage current due to defects such as Bi vacancies accompanied by oxygen vacancies. To reduce the leakage current in this experiments we prepared  $\text{Bi}_{(4-x)} \Pi_x \text{Ti}_3 \text{O}_{12}$  thin films where  $\Pi = \text{Ce}, \text{Er}, \text{Pr}$ . using a 5 mol % Bi-excess composition, and doped the bare material BIT with rare earths. The value obtained of leakage current density around of  $10^{-6} - 10^{-7} \text{A}/\text{cm}^2$  for all thin films.

From these studies of synthesis and characterization of bismuth titanate doped with rare earths in specific Cerium, Erbium and Praseodymium were obtained the hoped response ferroelectric although for the case of Er the poor saturation exhibit by the hysteresis loops it must be investigated and to make new tests. In the case of Ce, the hysteresis loops present a small mismatch at the end of the hysteresis loop that it can be solved applying more excess of Bi in the solution, or to look alternatives to suppress the vacancies of oxygen. For the case of Pr that exhibited the best ferroelectric response, is recommended to make tests new for other values of dopant molar fraction and realize studies of the fatigue that can present the thin films. Finally the actual physics behind the phenomena still need an extensive investigation.

## APPENDIX

The estimate of average crystallite sizes was made with the Debye-Sherrer's equation (5) (see section 4.1)

$$\langle \tau \rangle = \frac{0.95\lambda}{B \cos \theta}$$

Although it is not in our interest to make a demonstration we will justify the use of the same for the purpose at hand. We begin such justification with Bragg's law

$$2d \sin \theta = n\lambda \quad (21)$$

Where  $d$  is the separation between planes of given family,  $\theta$  is the angle of incidence and reflection measured with respect to planes,  $\lambda$  is the wavelength of the incident radiation and  $n$  is the order, that for first order maxima should be taken as one, so that

$$2d \sin \theta = \lambda \quad (22)$$

Takin the natural logarithm of both sides of the equation

$$\ln 2 + \ln d + \ln \sin \theta = \ln \lambda \quad (23)$$

Differentiating implicitly

$$\frac{d'}{d} + \frac{\cos \theta d\theta}{\sin \theta} = \frac{\lambda'}{\lambda} \quad (24)$$

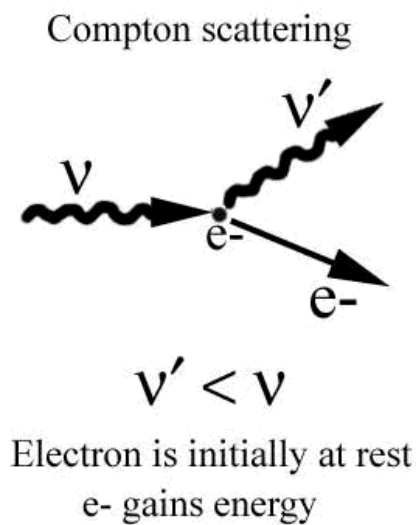
In the theory of measurement the error are not infinitesimally small and the primes should be taken as deltas, i.e.

$$\frac{\Delta d}{d} + \frac{\cos \theta \Delta \theta}{\sin \theta} = \frac{\Delta \lambda}{\lambda} \quad (25)$$

Where  $\frac{\Delta d}{d}$  is the relative error in the measurement of the plane separation, the second term is the relative error in the measurement of the angle and the term at the right of the equation is the relative error in the wavelength. These errors do not come necessarily from a mishandling of the instrument but are inherent to the measuring process.

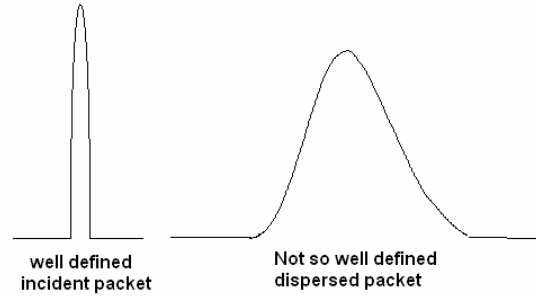
The error  $\Delta d$  as compare to  $d$  may come from the fact that the atoms are moving around an equilibrium position and therefore may introduce an uncertainty in the measurement of  $d$  beyond that permitted by the uncertainty principle. This term should be small as compare to the other terms in the equation if the time of exposure is small which the case is usually.

The error  $\Delta\theta$  in the angle is due to the fact that there is some spreading in the incident radiation and a larger one in the scattering radiation. The error in the wavelength may be tracked down, through the structure form factors  $S_k$ , and the atomic form factor  $F_k$ , to the interaction of the incident X-rays with electrons. As it is well known, the frequency and therefore the wavelength of the radiation changes during the scattering process. For an incident photon and a free electron this is given by Compton's expression



$$\lambda' - \lambda = \frac{h}{mc} (1 - \cos \phi) \quad (26)$$

Although the electron in the crystal are bound some spreading in the wavelength and therefore in the wave packet must occur.



That is the width of the packets should increased upon scattering going back to equation (25) and multiplying the left side by  $2d \sin \theta$  and the right side by  $\lambda$  (from Bragg's law) we obtain

$$2\Delta d \sin \theta + 2d \cos \theta \Delta \theta = \Delta \lambda \quad (27)$$

Since  $\Delta d$  is small and now multiplied by the  $\sin \theta$  is even smaller, to good approximation

$$2d \cos \theta \Delta \theta \approx \Delta \lambda \quad (28)$$

And therefore

$$d \approx \frac{\Delta \lambda}{2\Delta \theta \cos \theta} \quad (29)$$

Multiplying by a factor  $N$ , not necessarily an integer, so that  $N\Delta \lambda \approx \lambda$  then  $Nd \approx \langle \tau \rangle$ . So that

$$\langle \tau \rangle \cong \frac{\lambda}{2\Delta \theta \cos \theta} \quad (30)$$

Now if  $2\Delta \theta = B$  and the equation is corrected by a factor 0.95, that brings us to the Debye-Sherrer's equation.

$$\langle \tau \rangle = \frac{0.95\lambda}{B \cos \theta} \quad (5)$$

In analyzing the expression it is obvious that if  $\Delta\lambda$  is small then  $N$  must be large so that  $N\Delta\lambda \approx \lambda$ . If we let  $\Delta\lambda \rightarrow 0$  then  $N \rightarrow \infty$  and the size of the grain  $Nd$  goes also to infinity which is the correct limit for single crystals. On the other hand the larger  $\Delta\lambda$  the poorer the measurement and the larger the uncertainty in the average crystallite size.

## 7. REFERENCES

- [1] R. E Melgarejo, M. S. Tomar, Appl. Phys. Lett, Vol. 81, Num. 14 (2002).
- [2] M. E. Lines and A. M. Glass, Principles and Applications of Ferroelectric and Related Materials, Claredon Press, (oxford) 1977.
- [3] Nicola A. Spaldin, Science, Vol.304, 11june (2004).
- [4] Carlos Paz de Araujo, James F. Scout, and George W. Taylor, Ferroeelctric Thin Films: Synthesis and Basic Properties, Vol. 10 Part I, Gordon and Breach Publisher (1996).
- [5] Dragan Damjanovic, Ferroelectric, Dielectric and Piezoelectric Properties of Ferroelectric Thin Films and Ceramic, Rep. Prog. Phys. Vol. 61 (1998), PP 1267-1324.
- [6] S.C.Philpy, D.A. Kamp, A. D. DeVilbiss, Proceedings of the IEEE, (2000).
- [7] David Bondurant, and Fred Gnadinger, IEEE Spectrum Vol.89, PP 0030-0033 (1989).
- [8] R.Ramesh, Thin Film Ferroelectric Materials and Devices, Kluwer Academic Publishers (1997).
- [9] Jong-Ho Park, Jong-Seong Bae, Byung-Chun Chio, Jung-Jeong, Journal Appl. Phys. Vol. 97, 064110 (2005).
- [10] P. V. Pavlov, A. F Jojlov, Física del Estado Sólido, Editorial Mir, Moscú (1987).
- [11] C. B. Sawyer, C. H. Tower, Physical Review. Vol. 35, 269, (1930).
- [12] Takashi Hayashi, Naoto Oji, Hiroshi Maiwa, Journal Appl. Phys, Vol.33, 5277-5280 (1994).

- [13] G. A. Smolenskii, V. A. Bokov, V. A. Isupov, N. N. Krainik, R. E. Pasyukov, and A. I Sokolov, *Ferroelectric and Related Materials*, Gordon and Breach Science Publisher (1984).
- [14] P. R Graves, G. Hua, S. Myhra, and J. G. Thompsons, *Journal. Sold. State. Chem*, Vol. 114, PP 112-122 (1995).
- [15] Takayuki Watanabe, Hiroshi Funakubo, *Appl. Phys. Lett*, Vol. 81, Num.9 (2002).
- [16] Kyoung-Tae Kim, Chang-II Kim, *Journal Vac. Sci. Technol. A* 21(4), Jul/Aug (2003).
- [17] Senlin Fu, Hiroyuky Ozoe, *journal Appl. Phys.* Vol. 30, 2240-2248 (1997).
- [18] Takashi Kojima, Takajuki Watanabe, Hiroshi Funakubo, Keisuke Saito, Minoru Osada, Masato Kakihana, *Journal. Appl. Phys*, Vol. 93, Num. 3 (2003).
- [19] Hirofuni Matsuda, Sachico Ito, Takashi Ilyima, *Jpn. Journal. Appl. Phys.* Vol. 42, PP 5977-5980 (2003).
- [20] Takashi Hayashi, Naoto Oji, and Hirishi Maiwa, *Jpn. J. Appl. Phys.* Vol.33, PP 5277-5280 (1994).
- [21] B. S. Kang, J. G. Yoon, T. K. Song, S. Seo, Y. W. So, T. W. Noh, *Jpn. Journal. Appl. Phys*, Vol. 41, PP 5281-5283 (2002).
- [22] J. S. Zhu, D. Su, X. M. Lu, H. X. Qin, Y: N. Wang, *Journal Appl. Phys*, Vol. 92, Num. 9 (2002)
- [23] A. Garg, Z. H. Barber, M. Dawber, J. F. Scott, A. Snedden, and P. Lightfoot, *Appl. Phys. Lett.* Vol. 83, 2412 (2003).
- [24] B. H. Park, B. S. Kang, S. D Bu, T. W. Noh, J. Lee and W. Jo, *Nature (London)* Vol. 401, 682 (1999).
- [25] Y. Noguchi, and M. Miyayama, *Appl. Phys. Lett*, Vol. 78, 1903 (2001).
- [26] Masaki Yamaguchi, and Takao Nagatomo, *Jpn. Journal. Appl. Phys*, Vol. 37, PP 5166-5170 (1998).

- [27] Masaki Yamaguchi, Takao Nagatomo, and Osamu Omoto, *Jpn. Journal. Appl. Phys*, Vol. 36, PP 5885-5888 (1997).
- [28] Xingsen Gao, Zhaohui Zhou, Junmin Xue and John Wang, *Journal, A. Ceram. Soc.* Vol. 88 [4] 1037-1040 (2005).
- [29] P. C. Joshi, and S. B. Krupanidhi, *J. Appl. Phys.* Vol.72, PP 5517-5519 (1992).
- [30] A. Q. Jiang, G. H. Li, and L. D. Zhang, *J, Appl. Phys*, Vol. 83, PP4878-4883 (1998).
- [31] Tomohiro Sakai, Takayuki Watanabe, Hiroshi Funakubo, Keisuke Saito, and Minoru Osada, *Jpn. Journal. Appl. Phys*, Vol. 42, PP166-169 (2003).
- [32] H. Wang, L. W. Fu, S. X. Shang, X. L. Wang, and M. H. Jiang, *Journal Phys. D: Appl*, Vol. 27, 393-395 (1994).
- [33] C .Jeffrey Brinker, George W. Scherer. *Sol-Gel Science*. Academic Press INC.
- [34] M. Daghli, T Kemmitt, *IPENZ Transactions*, Vol.27, No.1/Gen, (2000).
- [35] Yu-Ming Sun, Yi-Chan Chen, Jon-Yiew Gan, and Jenn-Chang Hwang, *Appl. Phys. Lett*, Vol. 81, Num. 17 (2002).
- [36] Jun Zhu, Xiao-Bing Chen, Wang-Ping Lu, Xiang-Yu Mao, and Rong Hui, *Appl. Phys. Lett*, Vol.83, Num. 9 (2003).
- [37] Wei Li, Yuan Yi, Dong Su, and Jinsong Zhu, *J. Appl. Phys*, Vol. 97, 084102 (2005).
- [38] S. T. Zhang, X. J. Zhang, H. W. Chen, Z. G. Liu, N. B. Ming, X. B Hu, and J. Y. Wang, *Appl. Phys. Lett.* 83, 4378 (2003).
- [39] J. H. Li, Y. Qiao, X. L. Liu, C. J. Nie, and C. J. Lu, *Appl. Phys. Lett.* 85, Num. 15 (2004).
- [40] A. Ginier, *X-ray Diffraction*, Freeman, San Francisco (1963).
- [41] Uong Chon, Hyun M. Jang, M. G. Kim, and C. H. Chang, *Phys. Review. Lett*, Vol 89, Num. 8 (2002).

- [42] Vera V. Daniel. Dielectric Relaxation, Academic Press, (London) 1967.
- [43] Hiroshi Maiwa, Naoya Lizawa, Daichi Togawa, and Takashi Hayashi, Appl. Phys. Lett, Vol. 82, Num. 11 (2003).
- [44] Quéré Yves. Physics of materials. Gordon and Breach science publisher (1998) pp 168-170.
- [45] Kittel Charles. Introducción a la física del estado sólido. pp 527-531, 662-661
- [46] Electrodynamics of Continuous Media 2<sup>a</sup> Ed. 19, 1984
- [47] J. Petzelt, et. al. J. European Ceramic Soc., 23 (2003) 2627-2632